ELECTRODEPOSITION OF COBALT FOR ADVANCED INTERCONNECT APPLICATIONS

by

YANG HU

QIANG HUANG, COMMITTEE CHAIR
C. HEATH TURNER
JAMES W. HARRIS
QING PENG
SUSHMA KOTRU

A DISSERATION

Submitted in partial fulfillment of the requirements
for the degree of Doctor of Philosophy
in the Department of Chemical and Biological Engineering
in the Graduate School of
The University of Alabama

TUSCALOOSA, ALABAMA

2021

ABSTRACT

Copper (Cu) damascene processes have been used to produce back end of line (BEOL) interconnect structures in integrated circuits (IC). As the critical dimension of BEOL structures approaches the electron mean free path of Cu or below, the Cu resistivity exponentially increases, posing significant challenges on further scaling. Metals with shorter electron mean free path, for example cobalt (Co), have been explored as the alternative material to replace Cu in the finest metal levels.

The Co electrodeposition process for interconnect applications must produce Co films that can reproducibly fill deep vias or trenches without any defects. It is can be achieved by adding small amounts of organic additives to the plating bath, which lead to the Co electrodeposition preferentially at the bottom of trench, known as bottom-up filling, or super conformal filling, or simply “super-filling”. As the size of interconnect continues to shrink, additives are becoming the key to the successful application of Co electrodeposition in IC manufacture. In this dissertation, a new class of organic additives, dioximes (dimethylglyoxime, cyclohexane dioxime, and furil dioxime), have been investigated for their effects on the electrochemical deposition process of cobalt.

In Chapter 2, the nucleation and growth behavior of Co deposition with the addition of dimethylglyoxime and cyclohexane dioxime are studied. Double-peak nucleation curves are observed during Co deposition for the first time. In Chapter 3, a descriptive model is established for the Co nucleation process using furil dioxime, where the suppression effect on Co deposition and the catalytic effect on hydrogen evolution are both more pronounced among the dioxime molecules. Mercaptopropanesulfonate, or MPS, a well-known accelerator used in Cu damascene process, is investigated during the Co deposition in Chapter 4. A

potential oscillation is observed during galvanostatic deposition for the first time and a kinetically controlled mechanism is proposed. In Chapter 5, Co films are electrodeposited with different additives including dimethylglyoxime, sodium chloride, and 3-mercapto-1-propanesulfonate. It is found that the addition of 3-mercapto-1-propanesulfonate into the electrolyte significantly increases the S incorporation level and decreases the grain size, both contributing to a higher sheet resistance of film.

DEDICATION

I would like to dedicate my dissertation to my parents, friends, and everyone who helped and guided me throughout my stay and research. A special dedication to Qizhi Tang, my grandma in heaven, those memories of whom I will be forever cherishing.

LIST OF ABBREVIATIONS AND SYMBOLS

A	Nucleation rate per active site
Al	Aluminum
APT	Atom probe tomography
BEOL	Back end of line
c	Bulk concentration
$C_{cottrell}$	Time-independent constant for 3-dimensional nucleation and growth
C_{side}	Time-independent constant for side reaction
Cu	Copper
Co	Cobalt
CEAC	Curvature Enhanced Accelerator Coverage
CHD	Cyclohexane Dioxime
CV	Cyclic voltammetry
D	Diffusion coefficient
DCEF	Differential Current Efficiency Fill
DI	Deionized
DMG	Dimethylglyoxime
EDS	Energy dispersive x-ray spectroscopy
EIS	Electrochemical impedance spectroscopy
F	Faraday constant
FD	Furil dioxime
FIB	Focused ion beam
HER	Hydrogen evolution reaction

i	Current Density
i_{ad0}	Constant for capacitive adsorption
$i_{ad}(t)$	Current density for capacitive adsorption
i_{max}	Maximum current density for nucleation peak
$i_{side}(t)$	Current density for side reaction
$i_{total}(t)$	Total current density
$i_{3D}(t)$	Current density for 3-dimensional nucleation and growth
JGB	Janus Green B
k	Dimensionless constant
k'	Dimensionless constant
LEAP	Local electrode atom probe
M	Molar Mass
MPA	Mercaptopropionic acid
MPS	3-mercapto-1-propanesulfonate
N	Number of nuclei
N_∞	maximum number of nuclei
NHE	Normal Hydrogen Electrode
PEG	polyethylene glycol
PVD	Physical vapor deposition
RDE	Rotating disk electrode
Ru	Ruthenium
SCE	Saturated calomel electrode
SDS	Sodium dodecyl sulfate
SEM	Scanning electron microscopy
SIMS	Secondary ion mass spectroscopy

S-NDR	S-shaped negative differential resistance
SPS	bis-(3-sulfopropyl)-disulfide
t	Time
t_{max}	Time to reach the maximum current density
TEM	Transmission electron microscopy
TSV	Through silicon vias
XRD	X-ray diffraction
z	Number of electrons transferred per molecule reduced
τ_{ad}	Time-independent constant for capacitive adsorption
$\varphi(t)$	Retardation of the growth of the extended coverage
$\phi(t)$	Retardation of the current by slow nucleation
$\theta(t)$	Actual fraction of area covered by diffusion zone
ρ	Density

ACKNOWLEDGEMENTS

I would like to extend my sincere thanks to everyone who helped me and guided me to make this dissertation accomplished. First and foremost, I would like to express the most gratitude to my Ph.D. advisor, Prof. Qiang Huang, for his incredibly selfless help, encouragement, guidance, and patience throughout my Ph.D. studies in the past four years. I truly appreciate his insightful ideas, continuous dedication and tremendous support of my professional development.

I would like to sincerely appreciate all my doctoral committee members, Prof. C. Heath Turner, Prof. James W. Harris, Prof. Qing Peng, and Prof. Sushma Kotru for the invaluable guidance and great advice on my research. I would like to thank William Sides, Shuvodeep De, Joseph Ortenero, Behzad Malekpouri, Kamal Ahammed, Tim Brusuelas, William Freeman, Dalton Cameron, Tyler Lyons, Dan Mantoni, Melissa Montalvo, Ryan Morelock, John White, and all other members of my research group for sharing their experiences, enthusiasm and assistance during my lab work. It has been great pleasure to work with all of you. I would also like to show my special gratefulness to all of the colleagues and friends throughout my Ph.D. study as well as Johnny Goodwin, Robert Holler, and Sanghamitra Deb for the expert training on the SEM, TEM, XRD, FIB, and LEAP.

I would like to thank my parents for their continuous support, without whom I would not have come thus far, and achieved what I am today. They have always been my inspiration and supported me not only economically but also with emotional comfort.

Finally, I want to thank all faculties, staffs, and students of the Department of Chemical and Biological Engineering at The University of Alabama, as well as the Central

Analytical Facility, the Center of Materials for Information Technology, the Chemistry Glass Shop, and the College of Engineering Machine Shop. Financial support by the National Science Foundation, the Graduate Council, and the Research Grant Council at The University of Alabama is greatly appreciated.

CONTENTS

LIST OF TABLES

LIST OF FIGURES

CHAPTER 1. INTRODUCTION

Electrodeposition of Copper for Interconnect Application

Interconnect technology plays an important role in the integrated circuit development. It is a network of conductive metals connecting transistors, resistors, and other electronic components on the chip.[1-2] The first generation of interconnect was made of aluminum (Al).[3] To create these interconnects, a layer of Al is deposited and it is patterned and etched into lines. Insulating material is deposited to fill the gaps between and to isolate the conducting lines. Along the advancement of semiconductor technology, the size of interconnects continues to decrease and Al no longer meets the performance requirements for interconnect.[4-5] In details, the interconnect not only needs to maintain high electrical conductivity but also has to survive the electromigration due to the high current densities in operation. To meet these requirements, copper (Cu) was selected to replace Al as the second generation of interconnect material because of its low resistivity and superior resistance to electromigration.[6] In the late 1990s, IBM developed the Cu damascene process to produce Cu interconnects using electrodeposition methods, primarily for its high deposition rate and low manufacturing costs.[7]

During the electrodeposition process, Cu is deposited to fill trenches by applying either current or voltage. The electrolyte usually contains cupric sulfate, sulfuric acid, and small amounts of various inorganic and organic chemicals as additives. Three typical filling profiles in an electrodeposition or electroplating process are shown in Figure 1-1.[7] In conformal plating, similar amount of Cu is deposited across the trench, resulting in a seam as the deposit on both sidewalls continues to grow until meeting each other. For subconformal plating, a void will be formed because more Cu are deposited at the top of trenh. For

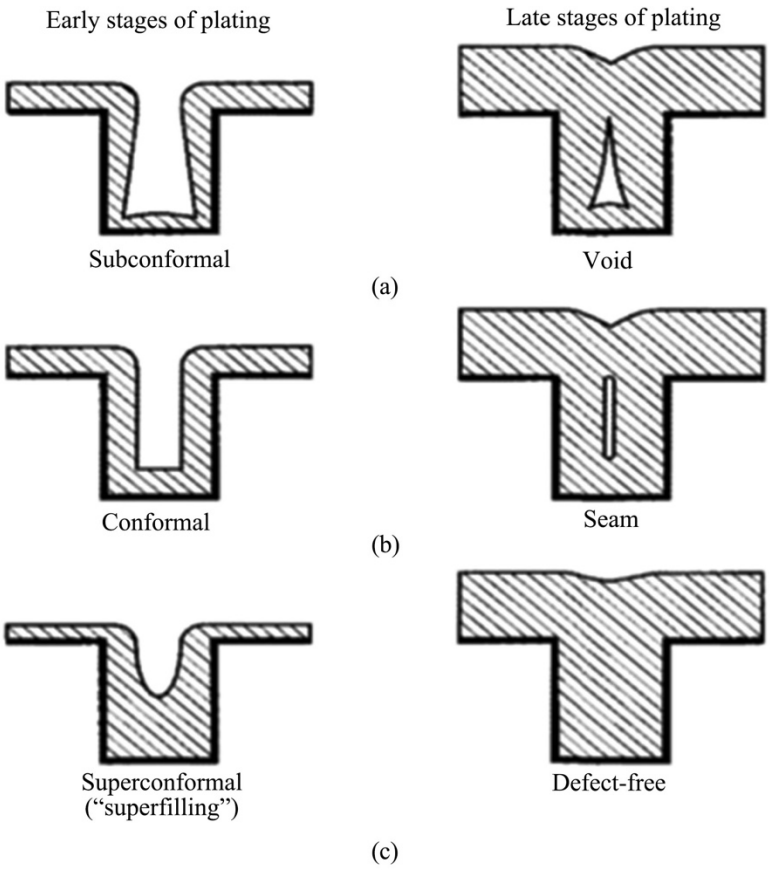

Figure 1-1. Types of profile evolution in damascene plating[8]

superconformal plating or superfilling, the deposition rate at the bottom is faster than the side wall and top region. Therefore, the superconformal plating is required to achieve a void-free filling in high aspect ratio trenches.

Organic additives in electrolyte play an important role in creating different plating rates at the bottom and top of the feature. There are three different types of additives utilized to achieve Cu void-free filling: suppressor, accelerator, and leveler.[9] The suppressors are usually glycol polymers such as polyethylene glycol (PEG), which decreases Cu deposition rate in the presence of chloride ions. The accelerators are typically soluble organic molecules containing thiol group, such as mercaptopropanesulfonate (MPS) and the dimer of MPS, bis-(3-sulfopropyl) disulfide (SPS). Both of these molecules weaken the suppression by PEG and facilitate the copper plating process. Levelers are typically high molecular weight monomers or polymers with cationic nitrogen functional groups, for example the Janus Green B (JGB),

which by itself shows weak suppression on Cu deposition. But the functions of leveler are to neutralize adsorbed accelerator, thus reducing surface topography and enhancing the filling performance.

A great deal of research have been conducted to study the interaction of different additives and how void-free trench filling is achieved.[10-17] One of proposed mechanisms is called Curvature Enhanced Accelerator Coverage (CEAC) mechanism,[13] which not only explains the effect of additives on the Cu filling process but also elucidate the filling process for gold,[18-20] silver,[21-23] and nickel.[24] Figure 1-2 shows the illustration of CEAC mechanism for different filling stages with three different additives. Before the current or voltage is applied, the concentrations of all solution species are equal at the top and bottom of trench. When the deposition starts, rapid surface area change at the bottom leads to the increasing surface coverage of adsorbed accelerators, which accelerates the Cu deposition at the bottom. When the trench is almost fully filled with Cu at the top, the accelerator will be neutralized with leveler and thus a pronounced protruding topography due to the momentum acceleration is avoided.

Although the primary role of the various organic additives has been to enable superfilling, they also provide control over the microstructure and recrystallization of deposited Cu films.[25-27] In fact, it is another important reason why electrodeposition was selected as the process for Cu interconnect manufacturing. To decrease the interconnect resistance, efforts have been made to understand how plating additives and annealing process affect Cu line resistance.[28-30] An important characteristic behavior of electrodeposited Cu is the self-annealing or room temperature recrystallization, where the as-deposited Cu film recrystallizes at room temperature.[31] The resistance of Cu film significantly decreases during the self-annealing process. However, since the distribution of the additive in the trench filling process is different from film deposition process, the corresponding impurity incorporation

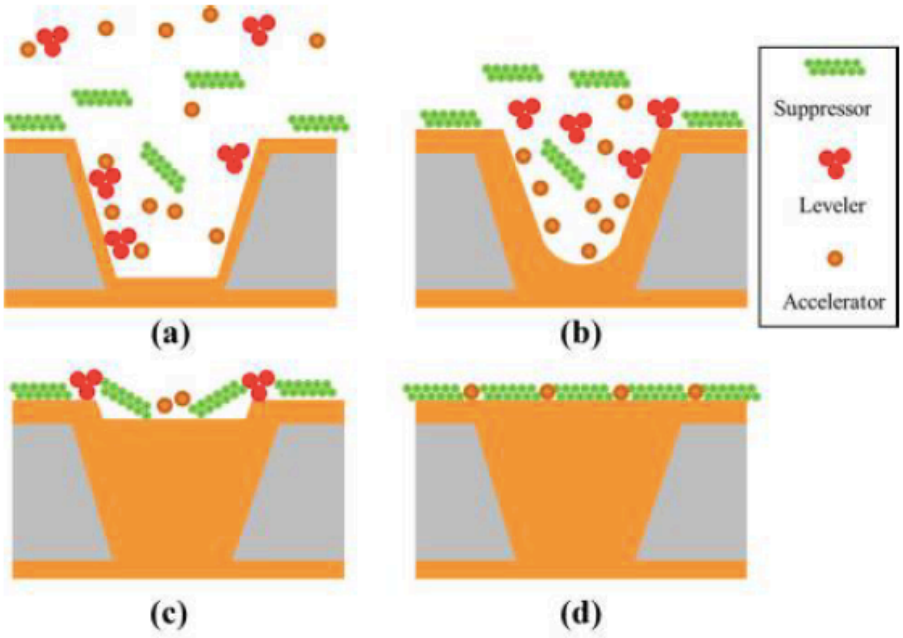

Figure 1-2. A schematic illustration of CEAC mechanisms for different filling periods[32]

behavior can also be different. Therefore, the annealing process is necessary for BEOL fabrication, and an elevated temperature will facilitate, expedite and stabilize the grain growth. Another important requirement of Cu interconnect is to survive the electromigration at high current densities. The microstructure of the electrodeposited Cu interconnect is found to be related to its resistance to electromigration. In general, a bamboo-like grain structure typically leads to good electromigration resistance.[27, 33-34]

Electrodeposition of Cobalt for Interconnect Application

The further scaling of damascene Cu interconnects in most recent technologies faces significant challenges due to the increase of Cu resistivity in small lines.[35] Because the electron scattering at interfaces (between Cu and surrounding materials) dominates, the resistivity of Cu will exponentially increase.[36] One of the solutions is to replace Cu with another material with much shorter electron mean free path.[37] The resistivity of such material is less dominated by the interface scattering when the line dimension is greater than the electron mean free path and will not significantly increase as the dimension decreases, thus enabling further scaling.[38] Co has been one of the most promising materials for interconnect

application because of its shorter mean free path, better electromigration resistance, and relatively low manufacturing cost.[39-40]

Since the thermal equilibrium voltage of Co^{2+}/Co, or the Co deposition potential, is more negative than that of H^+/H_2, proton reduction or hydrogen evolution reaction (HER) is inevitable and is expected to impact the Co filling process. Defect-free filling of Co has been recently reported in different dimensions of trench using a single suppressor.[41-46] HER has been found to be crucial in such processes, where it helps to create a contrast in current efficiency between top and bottom of the trench and leads to superconfomal plating. The proposed mechanism is called Differential Current Efficiency Fill (DCEF).[44]

Figure 1-3 shows the diagram of DCEF mechanism. Before current or voltage is applied, the relative concentrations of all species in the bath are the same between the top field, the feature bottom, and the bulk solution. When certain current or voltage is applied,

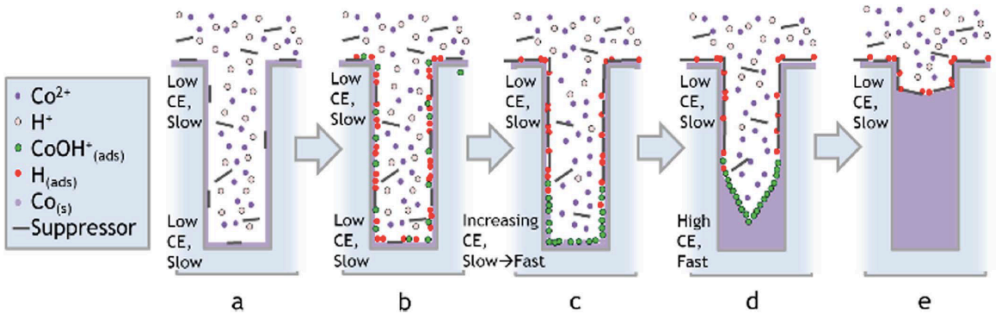

Figure 1-3. A schematic diagram of DCEF mechanisms for different filling periods.[44]

conformal deposition begins because the deposition rate is the same across the trench.

Since the diffusion rate of a chemical species from bulk solution to the bottom of feature is significantly slower than that to the top field, pH and suppressor gradients are formed within the feature. The pH gradient results in a higher current efficiency at the feature bottom and enhances the deposition rate at the bottom. Relatively low concentrations of suppressor at the base of the trench also leads to a faster deposition rate. Therefore, bottom-up filling is achieved and continues across the trench until such gradients are dissipated at the top field.

Because such concentration gradients are not extremely pronounced in practice, the bottom-up filling continues slowly.

While the interactions between different additives, annealing process, and impurity distribution on Cu interconnects have been extensively investigated, very few literature is available for the microstructure and impurity incorporation of Co interconnects. Kelly et al. conducted a comprehensive study about Co film properties (resistivity, impurity concentration, and grain structure) with different thin film deposition methods (physical vapor deposition, chemical vapor deposition, and electrodeposition).[47] It was found that the impurity level of Co films could be related to deposition methods, additive composition, and annealing process. Doubina et al. reported a systematic study about the effect of annealing process on the grain structure of electrodeposited Co films and lines. Lowest resistivity of Co lines was obtained after 300 to 350 °C annealing process and large Co grains were observed.[48]

Electrochemical Methods

Electrochemistry is widely applied in many research fields. Examples can be found in lithium batteries,[49] fuel cells,[50] water electrolysis,[51] electroplating,[7] electrorefining,[52] and corrosion.[53] Electrochemical methods used in various fields can be significantly different. In this section, the common electrochemical methods frequently used in this dissertation are discussed.

The majority of electrochemical work are performed in a three-electrode electrochemical cell, including a reference electrode, working electrode, and counter electrode. The reference electrode serves as a reference point for voltmeter to measure the working electrode potential. In addition, because a tiny current passes through the reference electrode, the voltage drop due to the solution resistance between the reference electrode and working electrode is usually small. This solution resistance is further reduced using a

capillary connecting the reference electrode to a position in catholyte close to the working electrode. A glass frit is used to separate the anolyte from the catholyte, preventing any oxidized species generated on anode contaminating the catholyte.

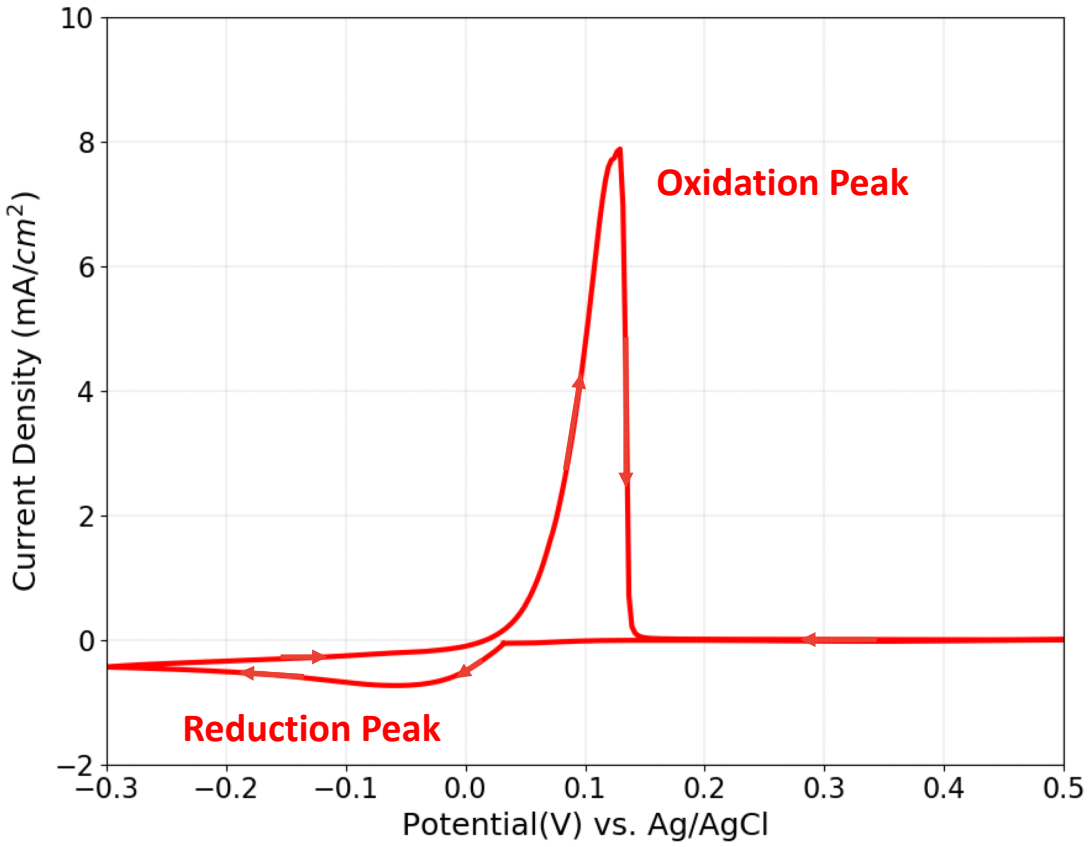

Figure 1-4. A typical cyclic voltammetry curve.

Cyclic voltammetry (CV) is commonly used in electrochemistry to study the reduction and oxidation reaction of ionic or molecular species. It is performed by cycling the potential of a working electrode, and measuring the resulting current. A typical CV curve in metal deposition is shown in Figure 1-4. Generally, open circuit potential is selected as the start point and the potential decreases at a constant rate to the more negative potential. Reduction reactions will occur when the required potential is reached, and the corresponding current will be measured. This current reflects the reaction rate, in other words, a more negative current indicates a faster reaction rate. The current will initially follow the Butler-Volmer equation,[54] where the reaction kinetic dominates the deposition process. After that, as

the potential scan continues, the deposition rate further increases and becomes even faster than the diffusion rate of reactants. Consequently, the concentration of reactants near the electrode gradually decreases resulting in the decrease of current, which explains the deposition peaks shown in CVs. Once the defined cathodic vertex potential is reached, the direction of scan will be reversed. When a certain positive potential is reached, the oxidation reaction will occur on the working electrode, where deposited metal will dissolve into the solution.

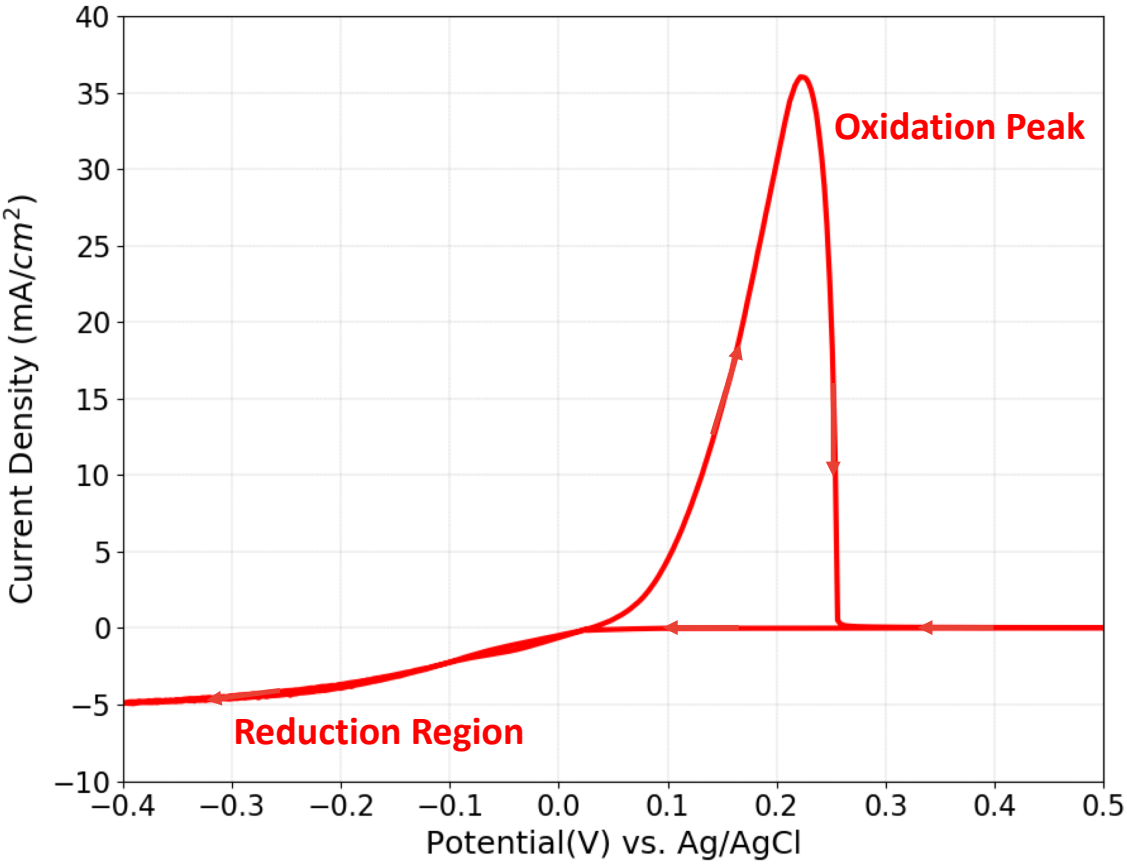

Figure 1-5. A typical cyclic voltammetry curve with RDE.

To facilitate the convection and diffusion process during CV scans, a rotating disk electrode (RDE) is frequently used. The function of RDE is to continuously supply fresh reactants to the electrode surface. In the presence of RDE, a horizontal current line at mass transfer limiting region can be obtained in the CV and it indicates a diffusion control process. There are several influencing factors affecting the diffusion process such as rotation

rate, kinematic viscosity of solution, and the concentration of active species in solution. The value of this horizontal line can be calculated using Levich equation.[54]

Metal deposition is typically conducted either in potentiostatic or galvanostatic modes. In the potentiostatic mode, or the chronoamperometry method, a constant potential is applied while the current is measured. In galvanostatic mode, the current is held constant while the potential is measured. During both modes, some additives can be added to investigate the effect of additives on deposition process. In such studies, various changes in the measured current or potential can be observed depending on the effects of additive on metal deposition. Another type of study is for the metal nucleation, where chronoamperometry is typically used. In general, a constant potential is applied at the beginning of metal deposition on the foreign substrate and the growth rates of nuclei are reflected in the acquired current transients.

References

1. Singer, P., Tantalum, copper and damascene: The future of interconnects. *Semiconductor international* **1998,** *21* (6), 90-95.

2. Baklanov, M. R.; Adelmann, C.; Zhao, L.; De Gendt, S., Advanced interconnects: materials, processing, and reliability. *ECS Journal of Solid State Science and Technology* **2014,** *4* (1), Y1.

3. Shacham-Diamand, Y.; Osaka, T.; Datta, M.; Ohba, T., *Advanced nanoscale ULSI interconnects: fundamentals and applications*. Springer: 2009.

4. Steinlesberger, G.; Schindler, G.; Engelhardt, M.; Steinhogl, W.; Traving, M. In *Aluminum nano interconnects*, Proceedings of the IEEE 2004 International Interconnect Technology Conference (IEEE Cat. No. 04TH8729), IEEE: 2004; pp 51-53.

5. Bohr, M. T. In *Interconnect scaling-the real limiter to high performance ULSI*, Proceedings of International Electron Devices Meeting, IEEE: 1995; pp 241-244.

6. Merchant, S. M.; Kang, S. H.; Sanganeria, M.; van Schravendijk, B.; Mountsier, T., Copper interconnects for semiconductor devices. *JOM* **2001,** *53* (6), 43-48.

7. Andricacos, P. C.; Uzoh, C.; Dukovic, J. O.; Horkans, J.; Deligianni, H., Damascene copper electroplating for chip interconnections. *IBM Journal of Research and Development* **1998,** *42* (5), 567-574.

8. Jhothiraman, J. K.; Balachandran, R., Electroplating: Applications in the Semiconductor Industry. *Advances in Chemical Engineering and Science* **2019,** *9* (2), 239-261.

9. Broekmann, P.; Fluegel, A.; Emnet, C.; Arnold, M.; Roeger-Goepfert, C.; Wagner, A.; Hai, N.; Mayer, D., Classification of suppressor additives based on synergistic and antagonistic ensemble effects. *Electrochim. Acta* **2011,** *56* (13), 4724-4734.

10. Hayase, M.; Taketani, M.; Aizawa, K.; Hatsuzawa, T.; Hayabusa, K., Copper bottom-up deposition by breakdown of PEG-Cl inhibition. *Electrochem. Solid-State Lett.* **2002,** *5* (10), C98-C101.

11. Moffat, T.; Wheeler, D.; Huber, W.; Josell, D., Superconformal electrodeposition of copper. *Electrochem. Solid-State Lett.* **2001,** *4* (4), C26-C29.

12. Moffat, T. P.; Bonevich, J.; Huber, W.; Stanishevsky, A.; Kelly, D.; Stafford, G.; Josell, D., Superconformal electrodeposition of copper in 500–90 nm features. *J. Electrochem. Soc.* **2000,** *147* (12), 4524-4535.

13. Moffat, T. P.; Wheeler, D.; Edelstein, M. D.; Josell, D., Superconformal film growth: Mechanism and quantification. *IBM Journal of Research and Development* **2005,** *49* (1), 19-36.

14. Cha, S. H.; Kim, S.-S.; Cho, S. K.; Kim, J. J., Copper bottom-up filling by electroplating without any additives on patterned wafer. *Electrochem. Solid-State Lett.* **2007,** *10* (2), D22-D24.

15. Lee, C. H.; Lee, S. C.; Kim, J. J., Bottom-up filling in Cu electroless deposition using bis-(3-sulfopropyl)-disulfide (SPS). *Electrochim. Acta* **2005,** *50* (16-17), 3563-3568.

16. Chang, C.; Lu, X.; Lei, Z.; Wang, Z.; Zhao, C., 2-Mercaptopyridine as a new leveler for bottom-up filling of micro-vias in copper electroplating. *Electrochim. Acta* **2016,** *208*, 33-38.

17. Lu, X.; Yao, L.; Ren, S.; Wang, Z., A study of bottom-up electroplated copper filling by the potential difference between two rotating speeds of a working electrode. *J. Electroanal. Chem.* **2014,** *712*, 25-32.

18. Josell, D.; Moffat, T., Extreme bottom-up filling of through silicon vias and damascene trenches with gold in a sulfite electrolyte. *J. Electrochem. Soc.* **2013,** *160* (12), D3035-D3039.

19. Josell, D.; Beauchamp, C.; Kelley, D.; Witt, C.; Moffat, T., Gold superfill in sub-micrometer trenches. *Electrochem. Solid-State Lett.* **2005,** *8* (3), C54-C57.

20. Josell, D.; Wheeler, D.; Moffat, T. P., Gold superfill in submicrometer trenches: Experiment and prediction. *J. Electrochem. Soc.* **2006,** *153* (1), C11-C18.

21. Baker, B.; Freeman, M.; Melnick, B.; Wheeler, D.; Josell, D.; Moffat, T. P., Superconformal electrodeposition of silver from a KAg (CN) 2 KCN KSeCN electrolyte. *J. Electrochem. Soc.* **2003,** *150* (2), C61-C66.

22. Moffat, T. P.; Baker, B.; Wheeler, D.; Bonevich, J. E.; Edelstein, M.; Kelly, D.; Gan, L.; Stafford, G. R.; Chen, P.; Egelhoff, W., Superconformal electrodeposition of silver in submicrometer features. *J. Electrochem. Soc.* **2002,** *149* (8), C423-C428.

23. Baker, B.; Witt, C.; Wheeler, D.; Josell, D.; Moffat, T. P., Superconformal silver deposition using KSeCN derivatized substrates. *Electrochem. Solid-State Lett.* **2003,** *6* (5), C67-C69.

24. Josell, D.; Baker, B.; Witt, C.; Wheeler, D.; Moffat, T. P., Via filling by electrodeposition superconformal silver and copper and conformal nickel. *J. Electrochem. Soc.* **2002,** *149* (12), C637-C641.

25. Barmak, K.; Gungor, A.; Cabral Jr, C.; Harper, J., Annealing behavior of Cu and dilute Cu-alloy films: Precipitation, grain growth, and resistivity. *J. Appl. Phys.* **2003,** *94* (3), 1605-1616.

26. Bonou, L.; Eyraud, M.; Denoyel, R.; Massiani, Y., Influence of additives on Cu electrodeposition mechanisms in acid solution: direct current study supported by non-electrochemical measurements. *Electrochim. Acta* **2002,** *47* (26), 4139-4148.

27. Hu, C.-K.; Gignac, L.; Baker, B.; Liniger, E.; Yu, R.; Flaitz, P. In *Impact of Cu microstructure on electromigration reliability*, International Interconnect Technology Conference, IEEE 2007, IEEE: 2007; pp 93-95.

28. Kelly, J.; Nogami, T.; Van der Straten, O.; Demarest, J.; Li, J.; Penny, C.; Vo, T.; Parks, C.; DeHaven, P.; Hu, C.-K., Electrolyte additive chemistry and feature size-dependent impurity incorporation for Cu interconnects. *J. Electrochem. Soc.* **2012,** *159* (10), D563-D569.

29. Huang, Q.; Avekians, A.; Ahmed, S.; Parks, C.; Baker-O'Neal, B.; Kitayaporn, S.; Sahin, A.; Sun, Y.; Cheng, T., Impurities in the electroplated sub-50 nm Cu lines: The effects of the plating additives. *J. Electrochem. Soc.* **2014,** *161* (9), D388-D394.

30. Stangl, M.; Lipták, M.; Acker, J.; Hoffmann, V.; Baunack, S.; Wetzig, K., Influence of incorporated non-metallic impurities on electromigration in copper damascene interconnect lines. *Thin Solid Films* **2009,** *517* (8), 2687-2690.

31. Lagrange, S.; Brongersma, S.; Judelewicz, M.; Saerens, A.; Vervoort, I.; Richard, E.; Palmans, R.; Maex, K., Self-annealing characterization of electroplated copper films. *Microelectron. Eng.* **2000,** *50* (1-4), 449-457.

32. Wang, J.; Wu, M.; Cui, C., Factors governing filling of blind via and through hole in electroplating. *Circuit World* **2014**.

33. Hu, C.-K., Electromigration failure mechanisms in bamboo-grained Al (Cu) interconnections. *Thin Solid Films* **1995,** *260* (1), 124-134.

34. Hu, C.-K.; Rosenberg, R.; Lee, K., Electromigration path in Cu thin-film lines. *Appl. Phys. Lett.* **1999,** *74* (20), 2945-2947.

35. Steinhögl, W.; Schindler, G.; Steinlesberger, G.; Engelhardt, M., Size-dependent resistivity of metallic wires in the mesoscopic range. *Physical Review B* **2002,** *66* (7), 075414.

36. Wu, W.; Brongersma, S.; Van Hove, M.; Maex, K., Influence of surface and grain-boundary scattering on the resistivity of copper in reduced dimensions. *Appl. Phys. Lett.* **2004,** *84* (15), 2838-2840.

37. Zhang, W.; Brongersma, S. H.; Richard, O.; Brijs, B.; Palmans, R.; Froyen, L.; Maex, K., Influence of the electron mean free path on the resistivity of thin metal films. *Microelectron. Eng.* **2004,** *76* (1-4), 146-152.

38. Gall, D., Electron mean free path in elemental metals. *J. Appl. Phys.* **2016,** *119* (8), 085101.

39. Wei, C.-C.; Chou, E.; Shih, S.; Lin, S.-M. In *Bottom-up Filling of Damascene Trenches with Cobalt By Electroplating Process*, Meeting Abstracts, The Electrochemical Society: 2015; pp 949-949.

40. Kelly, J.; Chen, J.-C.; Huang, H.; Hu, C.; Liniger, E.; Patlolla, R.; Peethala, B.; Adusumilli, P.; Shobha, H.; Nogami, T. In *Experimental study of nanoscale Co damascene BEOL interconnect structures*, Interconnect Technology Conference/Advanced Metallization Conference (IITC/AMC), 2016 IEEE International, IEEE: 2016; pp 40-42.

41. Lee, C. H.; Bonevich, J. E.; Davies, J. E.; Moffat, T. P., Superconformal Electrodeposition of Co and Co–Fe Alloys Using 2-Mercapto-5-benzimidazolesulfonic Acid. *J. Electrochem. Soc.* **2009,** *156* (8), D301-D309.

42. Kang, J.; Sung, M.; Byun, J.; Kwon, O. J.; Kim, J. J., Proton Sensitive Additive for Cobalt Electrodeposition. *J. Electrochem. Soc.* **2020,** *167* (12), 122510.

43. Kang, J.; Sung, M.; Byun, J.; Kwon, O. J.; Kim, J. J., Superconformal Cobalt Electrodeposition with a Hydrogen Evolution Reaction Suppressing Additive. *J. Electrochem. Soc.* **2020,** *167* (16), 162514.

44. Rigsby, M. A.; Brogan, L. J.; Doubina, N. V.; Liu, Y.; Opocensky, E. C.; Spurlin, T. A.; Zhou, J.; Reid, J. D., Superconformal Cobalt Fill through the Use of Sacrificial Oxidants. *ECS Transactions* **2017,** *80* (10), 767-776.

45. Rigsby, M. A.; Brogan, L. J.; Doubina, N. V.; Liu, Y.; Opocensky, E. C.; Spurlin, T. A.; Zhou, J.; Reid, J. D., The Critical Role of pH Gradient Formation in Driving Superconformal Cobalt Deposition. *J. Electrochem. Soc.* **2019,** *166* (1), D3167-D3174.

46. Wu, J.; Wafula, F.; Branagan, S.; Suzuki, H.; van Eisden, J., Mechanism of Cobalt Bottom-Up Filling for Advanced Node Interconnect Metallization. *J. Electrochem. Soc.* **2019,** *166* (1), D3136-D3141.

47. Kelly, J.; Kamineni, V.; Lin, X.; Pacquette, A.; Hopstaken, M.; Liang, Y.; Amanapu, H.; Peethala, B.; Jiang, L.; Demarest, J., Annealing and Impurity Effects in Co Thin Films for MOL Contact and BEOL Metallization. *J. Electrochem. Soc.* **2019,** *166* (1), D3100-D3109.

48. Doubina, N. V.; Spurlin, T. A.; Opocensky, E. C.; Reid, J. D., The Effect of Thermal Annealing on Cobalt Film Properties and Grain Structure. *MRS Advances*, 1-9.

49. Jung, K. N.; Shin, H. S.; Park, M. S.; Lee, J. W., Solid-State Lithium Batteries: Bipolar Design, Fabrication, and Electrochemistry. *ChemElectroChem* **2019,** *6* (15), 3842-3859.

50. Rees, N. V.; Compton, R. G., Sustainable energy: a review of formic acid electrochemical fuel cells. *J. Solid State Electrochem.* **2011,** *15* (10), 2095-2100.

51. Yan, Y.; Xia, B. Y.; Zhao, B.; Wang, X., A review on noble-metal-free bifunctional heterogeneous catalysts for overall electrochemical water splitting. *Journal of Materials Chemistry A* **2016,** *4* (45), 17587-17603.

52. Willit, J.; Miller, W.; Battles, J., Electrorefining of uranium and plutonium—a literature review. *J. Nucl. Mater.* **1992,** *195* (3), 229-249.

53. Kear, G.; Barker, B.; Walsh, F., Electrochemical corrosion of unalloyed copper in chloride media—a critical review. *Corros. Sci.* **2004,** *46* (1), 109-135.

54. Bard, A. J.; Faulkner, L. R.; Leddy, J.; Zoski, C. G., *Electrochemical methods: fundamentals and applications*. wiley New York: 1980; Vol. 2.

CHAPTER 2. EFFECTS OF DIMETHYLGLYOXIME AND CYCLOHEXANE DIOXIME ON THE ELECTROCHEMICAL NUCLEATION AND GROWTH OF COBALT

Published Work Disclosure: This chapter is based on previously published paper (Hu, Y.; Huang, Q., Effects of Dimethylglyoxime and Cyclohexane Dioxime on the Electrochemical Nucleation and Growth of Cobalt. Journal of The Electrochemical Society 2019, 166 (1), D3175-D3181.)

Summary

Electrodeposition of cobalt on blanket Si with extremely thin cobalt seed was studied in the presence of two additives, dimethylglyoxime (DMG) and cyclohexane dioxime (CHD). Cyclic voltammetry (CV), potentiostatic current transients and galvanostatic nucleation studies were conducted to understand the effects of DMG and CHD on cobalt nucleation process. A typical cross-over in the cathodic sweep was observed in CV studies, consistent with a 3D cobalt nucleation and growth. An interesting "two-peak" phenomenon was observed in the potentiostatic studies with median concentrations of DMG and CHD. A two-step reduction reaction mechanism was proposed. The first peak was identified as the reduction reaction of Co^{2+} chelate, and the second peak was related to that of free Co^{2+}. This mechanism was further verified with the absence of the second current peak in a solution without free Co^{2+}.

Introduction

The scaling of damascene copper interconnects faces significant challenges in recent years because of the exponential increase of the resistivity of copper lines, particularly, for 7 nm technology and beyond.[1] The main reason for this resistivity increase is because the electron scattering at interfaces (between copper and surrounding materials) overwhelms the

intrinsic electron scattering and dominates the material resistivity.[2] One of the solutions to this challenge is to replace copper with another material with a much shorter electron mean free path.[3] The resistivity of such materials will continue to be dominated by the intrinsic scattering and will not dramatically increase as the dimension decrease. Cobalt is of great interest for this application due to its short mean free path, compatibility with semiconductor manufacturing, and a relatively low material cost.[4-5]

Electrodeposition is a simple and economical way to deposit metal films. However, it requires a complete understanding of the nucleation and growth process to design the right chemistry and process for a target product. For example, the interactions between additive components in a damascene copper chemistry has to be well understood to achieve a so-called bottom-up fill.[6-12] In addition, the deposition processes also have to be finely tuned in conjunction with the chemistry to improve nucleation and minimized sidewall defects in the interconnect structures.[13] Chronoamperometry is widely used to provide insights of the nucleation process. Under a constant potential, the growth rates of nuclei are reflected in the acquired current transients.[14] This method has been used to investigate the nucleation of cobalt on different substrates such as nickel, gold,[15-17] copper,[17-18] palladium[17, 19-20] and glassy carbon.[15, 21-23]

On the other hand, organic additives also greatly affect the film morphology and properties.[24] Specifically, different functional groups in organic additives were found to affect the deposition process. For example, molecules with a pair of conjugated oxime groups such as DMG and CHD showed a strong suppression effect on cobalt deposition.[25-26] Thiol groups were found to accelerate the deposition and amine groups would suppress the deposition rates of iron group metals.[27-29] However, studies to investigate the influence of organic additives on the cobalt nucleation process are limited.This paper presents a study of the effect of DMG and CHD on Co nucleation process. Since the early stage of

electrodeposition of Co depends strongly on the nature of substrates, an industrially relevant material stack, physical vapor deposited (PVD) TiN and thin Co, was used as the substrate.

Experimental

Experiments were carried out in a three-compartment cell with a glass frit to separate the cathode and anode solutions. A saturated calomel electrode (SCE) was used as the reference electrode, connecting to catholyte through a capillary. All potentials were referred with respect to this SCE. Si coupons cleaved from a 12-inch blanket wafer with Co (10 nm, PVD) on TiN (5 nm, PVD) were used as cathodes. A thin Co seed was used to mimic the substrates used in industry and to provide enough conductivity for the electrodeposition studies. But the seed is not expected to be continuous and Co electrodeposition behavior is dominated by the underneath TiN layer. The area of deposition was defined with plating tape and fixed at 0.385 cm^2.

The cobalt makeup solution was adapted from our previous study,[26] containing 0.01 M $CoSO_4$, 0.1 M Na_2SO_4, 0.1 M H_3BO_3, and 0.1 g/L sodium dodecyl sulfate (SDS). The pH of Co solution was adjusted to 5.0 with H_2SO_4 and NaOH. Concentrated DMG solutions (23,000 ppm) and CHD solutions (7,000 ppm) were prepared using the corresponding sodium salts. The prepared additives were then added into the Co makeup solution up to various concentrations of DMG or CHD. Another cobalt makeup solution containing 0.4 mM $CoSO_4$, 0.1 M Na_2SO_4, 0.1 M H_3BO_3, and 0.1 g/L sodium dodecyl sulfate (SDS), pH = 5.0 was also used, where a low Co^{2+} concentration is needed to ensure the complete complexation. All salts and organic additives were at least ACS grade and deionized (DI) water with a resistivity of 18 MOhm-cm was used in all studies.

Cobalt nucleation was studied using electrochemical techniques (cyclic voltammetry, chronoamperometry and galvanostatic DC deposition). An Autolab 302N potentiostat was

used for all electrochemical studies. Surface morphology of the deposited Co was examined with a scanning electron microscope (SEM, JEOL 7000, Japan).

Results

Cyclic voltammetry

Figure 2-1 shows a typical cyclic voltammetry (CV) curve for cobalt deposition in the additive free makeup solution. A scan rate of 81 mV s^{-1} was used. The voltammogram started at -0.3 V, scanned in the negative direction and reversed at -1.6 V. A cross-over was observed at around -0.90 V, which confirmed a typical Volmer-Weber three dimensional nucleation and growth process.[30] The sharp increase of cathodic current density observed at

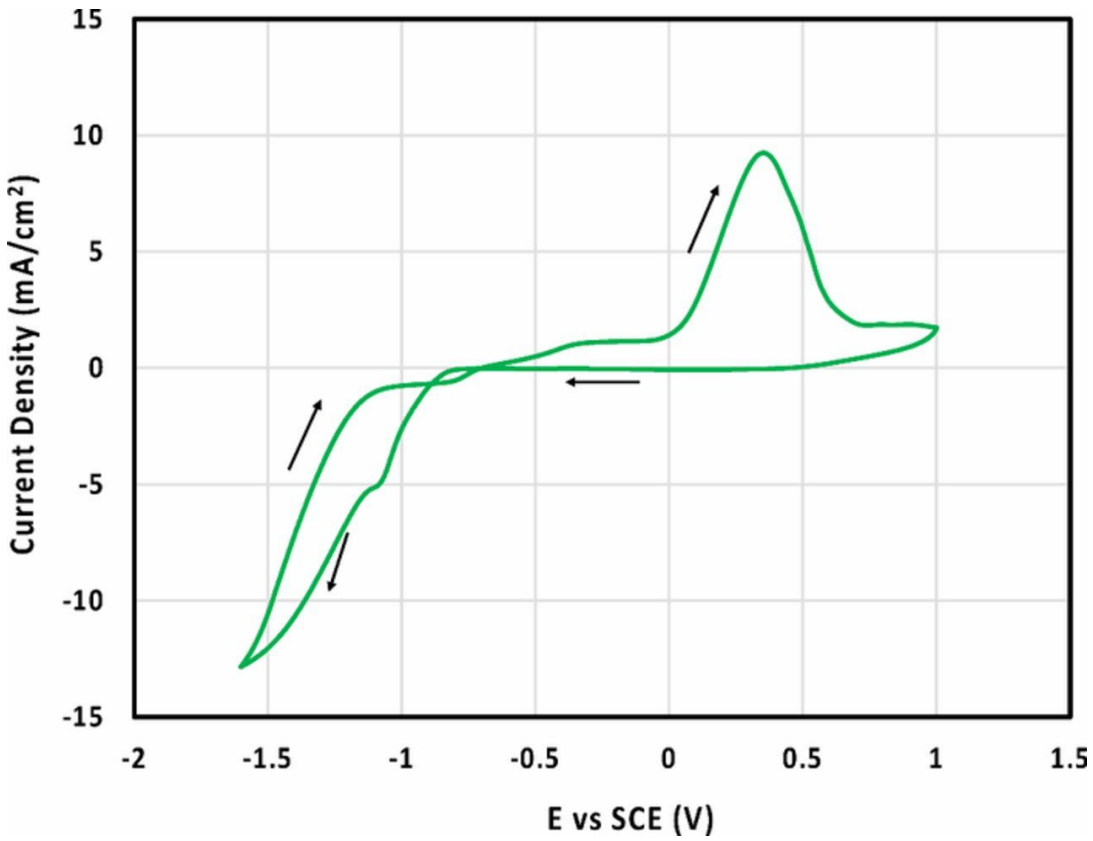

Figure 2-1. Cyclic voltammograms of Co deposition in aqueous solution comprising 0.01 M $CoSO_4$ + 0.1 M Na_2SO_4 + 0.1 M H_3BO_3 + 0.1 g/L SDS with pH 5.0. Potential scan rate was 81 mVs^{-1}.

-0.80 V corresponded to cobalt electrodeposition, resulting a shoulder peak at -1.15 V. The further increase of current density below -1.15 V is due to water reduction. Only one intense

peak was observed in the anodic sweep at potential above 0 V and it is believed to result from the dissolution of cobalt. As discussed above, Co deposition dominates the current from -0.80 V to -1.15 V. Therefore, a range of different potentials between -0.80 V and -1.1 V were selected for the following potentiostaic studies on Co nucleation.

Potentiostatic current transients

Figure 2-2 shows a series of current transients for the electrodeposition of cobalt at various potentials in the range of -0.85 to -1.05 V. An initial sharp decay which corresponds to an adsorption process was observed at relative less negative applied potential (-0.85 V, -0.90 V). This rapid decay is followed by a current increase due to an increase in the surface

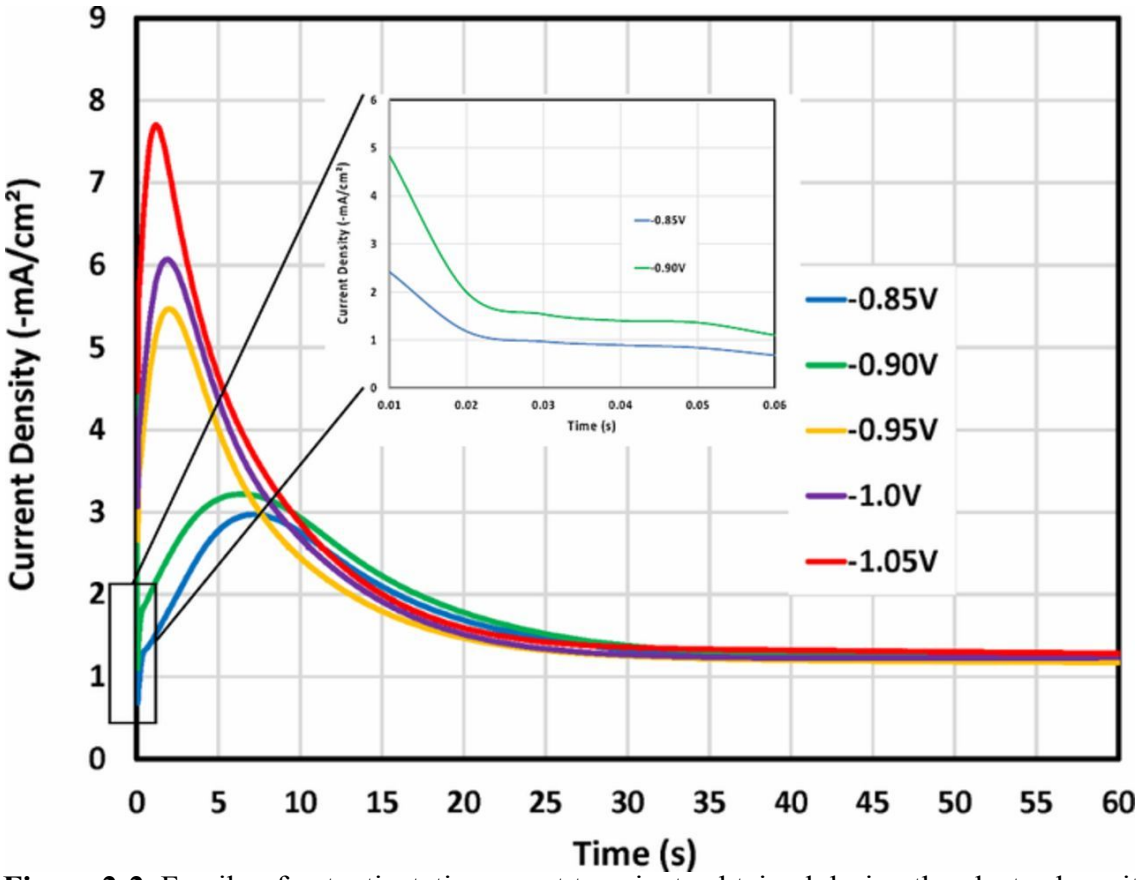

Figure 2-2. Family of potentiostatic current transients obtained during the electrodeposition of cobalt onto thin seed blanket wafer without additives at various potentials. The inset shows the magnified initial section of the transient curves at -0.85 and -0.90 V.

area associated with nucleus formation on the substrate. After a maximum, current density

gradually decreased again upon the development of a mass transport limited process. An ideal mass transport limited current decay during potentiostatic deposition can be described by the so-called Cottrell equation.[31] However, the currents in this study do not decay to 0 but stay at a constant of around 1.5 mA/cm^2. In this paper, we call this region of current transients as a "steady state current density". The observation of this steady state is believed to relate to a free convection of the electrolyte as well as a forced convection upon hydrogen evolution reaction. Since cobalt deposition occurs at a comparably negative potential, hydrogen evolution inevitably occurs. The surface agitation caused by hydrogen bubbling promotes the mass transport. The observed steady state current density includes Co deposition and hydrogen evolution.

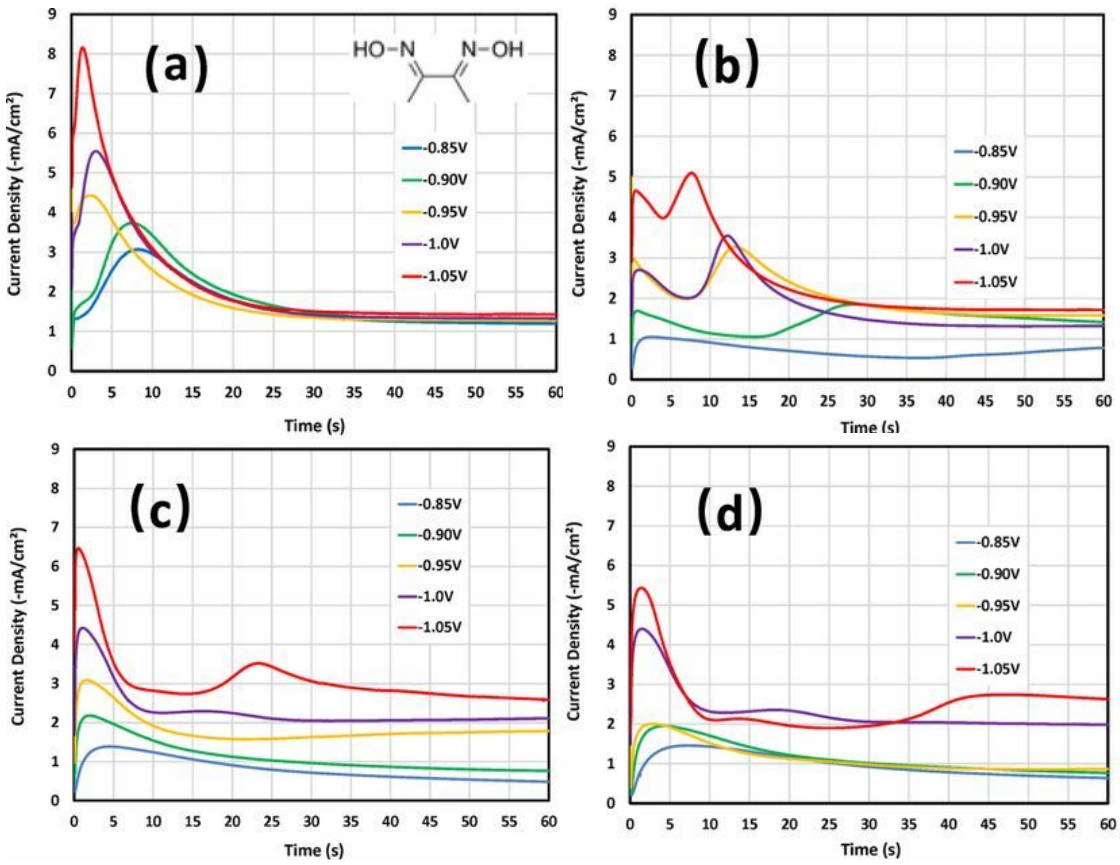

Figure 2-3. Current transients for cobalt deposition on thin Co seed blanket wafer at different potentials in 0.01M Co solutions with (a) 10-ppm (b) 100-ppm (c) 300-ppm (d) 500-ppm DMG. Inset in (a) shows the molecular structure of DMG.

The suppression effect of dioxime molecules including DMG and CHD on Co electrodeposition has been reported previously.[26] To further understand their impacts on the initial nucleation in Co deposition, current transients were acquired at various potentials and different additive concentrations. Figure 2-3 shows the chronoamperometry studies of Co nucleation in presence of DMG. The addition of 10 ppm DMG had little effects on the overall nucleation process, but a change of current peaks was observed. For example, the height of current peaks decreased (from 5.4 mA/cm^2 to 4.3 mA/cm^2) at -0.95 V. Similar behavior was also observed at -1.0 V. However, an increase of current peak was seen at -1.05 V. Moreover, the time to reach current peaks increased. Take -0.90 V case as an example, the time to reach the maximum current increased from around 6 s to 9 s upon the addition of 10 ppm DMG. In addition, the steady state current densities were almost the same for all potentials studied.

The suppression effect became more pronounced when the DMG concentration was increased to 100 ppm. The magnitudes of all current peaks decreased. More importantly, two nucleation peaks were observed for all applied potentials except for -0.85 V. It was noted that the height of second peak was higher than the first one. Moreover, the appearance of second peak delayed as the applied potentials became less negative. In detail, the second peak was at around 8 s, 13 s, 14 s, 28 s as the applied potential changed from -1.05 V to -0.9 V. The second peak did not fully emerge at -0.85 V up to a deposition time of 60 seconds and a steady state current was not reached. The steady state current densities at other potentials were approximately the same as the additive free and the 10 ppm DMG cases, suggesting the hydrogen evolution reaction rates were not significantly changed in the presence of 100 ppm DMG.

The height of the first peak significantly increased with the addition of 300 ppm DMG. Take -1.0 V as an example, the magnitude of first current peak increased from 2.8 mA/cm^2 for 100 ppm DMG to 4.2 mA/cm^2 for 300 ppm. The second peak was only observed

at relatively more negative applied potentials (-1.0 and -1.05 V). Furthermore, the appearance of the second peak further delayed and the height of second peak declined. Take -1.05 V as an example, the second peak showed up nearly 17 s later than the case with 100 ppm DMG. Moreover, the height of second peak dropped from 5.1 mA/cm^2 to 3.5 mA/cm^2. In addition, the steady state current density not only increased along with the applied potential in presence of 300 ppm DMG but also were higher than 100 ppm DMG cases at any potential studied. At a higher DMG concentration of 500 ppm, such trends became even more pronounced. The height of first peak decreased and the second current peak further delayed and diminished. In addition, it is worth noting that no significant difference was observed for the current transients at -0.85, -0.90, and -0.95 V, including the steady state current densities.

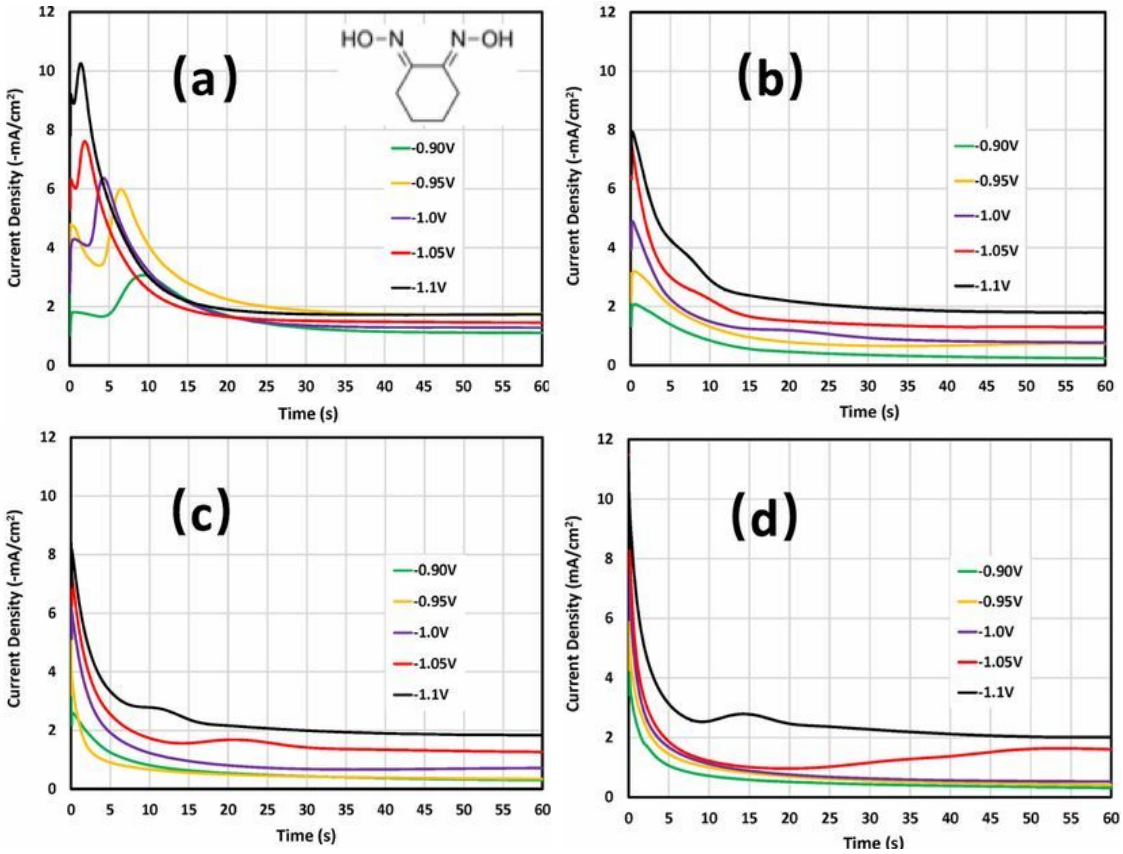

Figure 2-4. Current density-time transients for cobalt deposition on thin Co seed blanket wafer at different potentials in 0.01M Co solutions with (a) 10-ppm (b) 100-ppm (c) 300-ppm (d) 500-ppm CHD. Inset in (a) shows the molecular structure of CHD.

The effect of CHD on Co nucleation was studied in the same fashion. Due to a stronger suppression effect of CHD than DMG, a more negative potential range of -0.90 V to -1.1 V was used for the studies. Figure 2-4 presents the chronoamperometry study of Co nucleation. The suppression effect and the second current peak were clearly seen with the addition of 10 ppm CHD. The height of the first peak was lower than the second one, which was the same as 100 ppm DMG. Furthermore, the appearance of second peak delayed when a less negative potential was applied. For example, the second peak shifted from 3 s to 10 s as the applied potential changed from -0.90 V to -1.1 V. The effects of higher concentrations of CHD followed the same trend as DMG in Figure 2-3. The appearance of the second peak delayed and the peak height decreased as the CHD concentration increased. However, the first current peaks were found to be much sharper with CHD than DMG. No rising part of current was observed in most of the cases, resulting in a current decay instead of a current peak at the beginning of a transient.

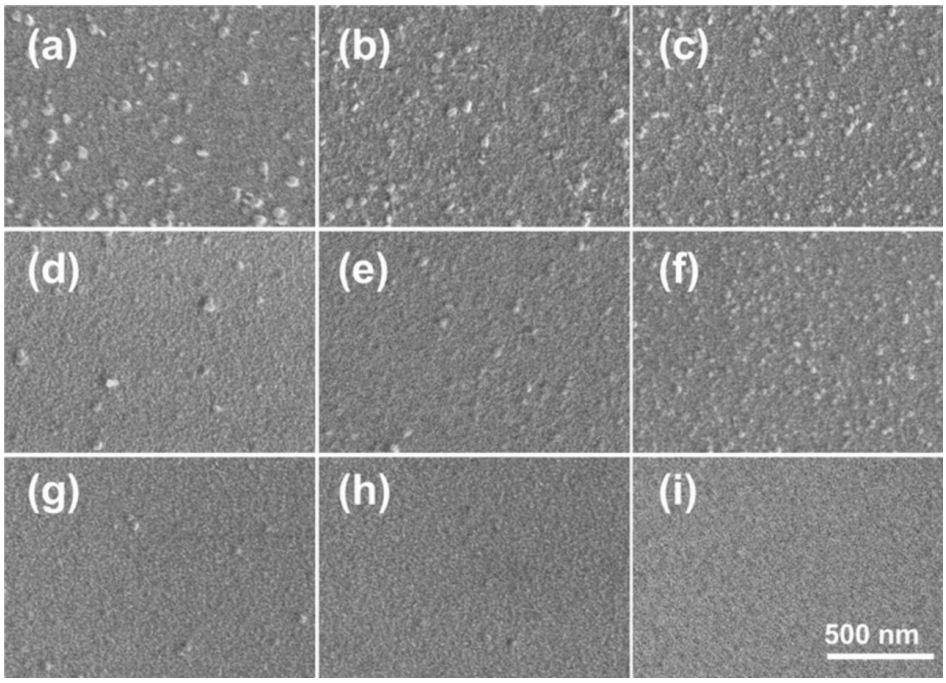

Figure 2-5. SEM images of cobalt nuclei deposited thin Co seed blanket wafer from solution containing 0.01 M Co with (a-c) 0, (d-f) 10, and (g-i) 100 ppm DMG at (a,d,g) -2, (b,e,h) -4, and (c,f,i) -10 mA/cm^2. different concentration of DMG and different current densities. The total deposition charge was -6.5 mC/cm^2.

Galvanostatic deposition with different current densities of -2, -4 and -10 mA/cm^2 were used to examine the effects of DMG and CHD on Co deposition. A constant charge density of -6.5 mC/cm^2 was used. The deposition time needed for this charge density are only up to 3.2 seconds, corresponding to a very small section at the beginning of current transients shown in Figures 2-3 and 2-4. Figures 2-5 and 2-6 show the top down SEM images of deposits. The same image of the substrate before deposition was included for comparison. It was evident that the nucleation density increased and the nucleus size decreased as the current densities increased in the additive free electrolyte. The addition of 10 ppm DMG resulted in a decrease in the number of cobalt nuclei for all the current densities used. Moreover, this decrease was the most pronounced at -4 mA/cm^2 and the least at -10 mA/cm^2. The nucleation density further decreased as the DMG concentration increased to 100 ppm. While this decrease of nucleation density was very evident at -2 mA/cm^2, only a handful of cobalt nuclei was observed at -4 and -10 mA/cm^2.

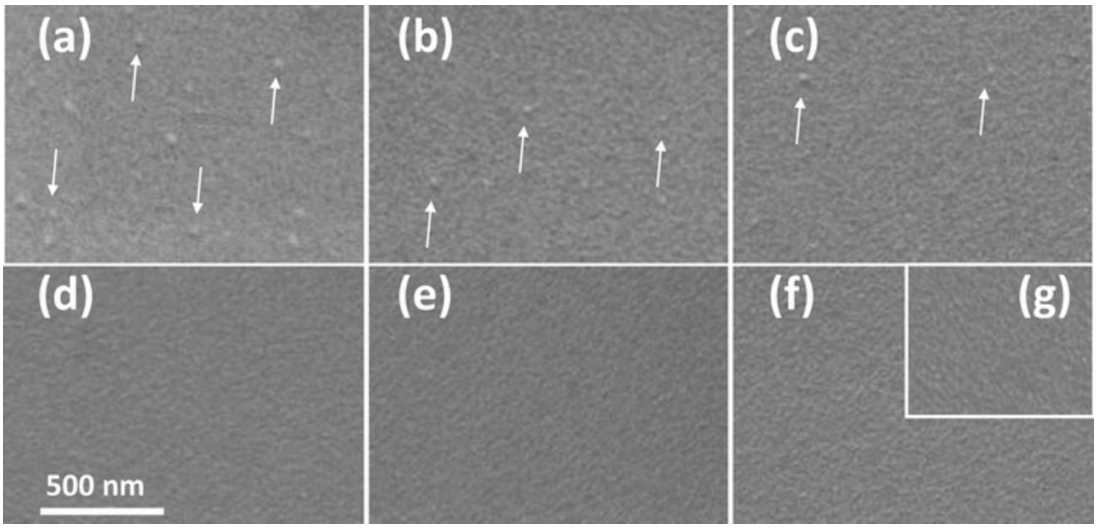

Figure 2-6. SEM images of cobalt nuclei deposited thin Co seed blanket wafer from solution containing 0.01 M Co with (a-c) 10 and (d-f) 100 ppm CHD at (a,d) -2, (b,e) -4, and (c,f) -10 mA/cm^2. The total charge was -6.5 mC/cm^2. The blanket substrate was shown in (g). White arrows were used to point at a few example nuclei.

A more pronounced suppression effect on nucleation was observed with the addition of CHD. The cobalt nucleation density and size with 10 ppm CHD were similar to the case

with 100 ppm DMG. This is consistent with the similarity in the double peak current transients observed in these two cases. There were very few cobalt nuclei observed at -4 and -10 mA/cm^2 when 10 ppm CHD was added into the solution. More cobalt nuclei were deposited at -2 mA/cm^2, but they are much less and smaller compared with the additive-free case. Increasing CHD concentration to 100 ppm led to no cobalt nuclei observed under SEM for all the current densities used.

To summarize the results, several interesting phenomena were observed: *i)* two current peaks were observed with the addition of median to low concentrations of DMG or CHD; *ii)* the height of first peak rises and the second peak diminishes upon the further addition of DMG or CHD; *iii)* the appearance of second peak delayed as the concentrations of DMG or CHD increase; *iv)* the addition of DMG or CHD suppressed the formation of cobalt nuclei dramatically, and this suppression was more pronounced for CHD than DMG at a same concentration.

Discussion

It is known that current transients reflect the physical and chemical changes during electrochemical nucleation process. In this study, several reactions are believed to occur simultaneously during the nucleation process and should be included in the discussion: Co^{2+} reduction reaction, Co^{2+} chelates reduction reaction, and hydrogen evolution reaction.

$$Co^{2+} + 2e \rightarrow Co$$

$$Co^{2+} + 2L^{-} \rightarrow CoL_2$$

$$CoL_2 + 2e \rightarrow Co + 2L^{-}$$

$$2H^{+} + 2e \rightarrow H_2$$

$$2H_2O + 2e \rightarrow H_2 + 2OH$$

where L stands for a ligand, and CoL_2 for a Co chelate consisting of one Co^{2+} and two dioxime molecules. While the above equations are used to represent the reduction reactions

in solution, the detailed mechanisms can involve adsorbed intermediates. For example, the electrodeposition of iron group metals, namely, Ni, Fe, and Co, typically involves a monovalent metal cation intermediate species adsorbed on the electrode surface.[32-35]

$$Co^{2+} + OH^- + e^- \rightarrow CoOH_{ads}$$

$$CoOH_{ads} + e^- \rightarrow Co + OH$$

Electrochemical nucleation and growth of metal on a foreign substrate have been extensively studied.[36-38] A 3D nucleation process can be typically characterized with a single current peak in the transient experiment. This single-peak current transient curve results from a synergistic interaction between a preferred deposition of metal on itself, the increase of total surface area of metal nuclei, and a consumption and depletion of metal cations in the solution in the vicinity of nuclei. Such a current peak has also been reported for Co deposition. However, for many cases in our studies, two current peaks were observed during the potentiostatic nucleation process. It is highly likely that two reactions happen separately and result in these two peaks. Attempts are made here to discuss the mechanisms for such a new nucleation behavior.

Proposed Mechanism

Figure 2-5 shows a diagram illustrating the proposed mechanism for the Co electrodeposition in a DMG-containing electrolyte. Initially, the Co solution contains Co^{2+} and $Co(DMG)_2$ complex before deposition. All the DMG molecules are present in the form of $Co(DMG)_2$ complex due to an extremely high stability constant of the complex and a much higher concentration of Co^{2+} than DMG.[39] A previous study[26] showed that the suppression effect of dioxime molecules on Co electrodeposition broke down at a potential closely related to the stability constants of Co-dioxime chelates. This suggests that the suppression effect results from a preferred adsorption of such chelates over Co^{2+} and the

suppression breaks down because of the reduction of the chelate at more negative potentials. With a stronger electro-adsorption of $Co(DMG)_2$ than Co^{2+}, the former is expected to preferably adsorb on the electrode and prevent the adsorption of CoOH intermediate. In other words, the electrode is occupied by $Co(DMG)_2$ complex. After that, the $Co(DMG)_2$ on the surface complex will be reduced to Co metal when a sufficiently negative potential is applied.

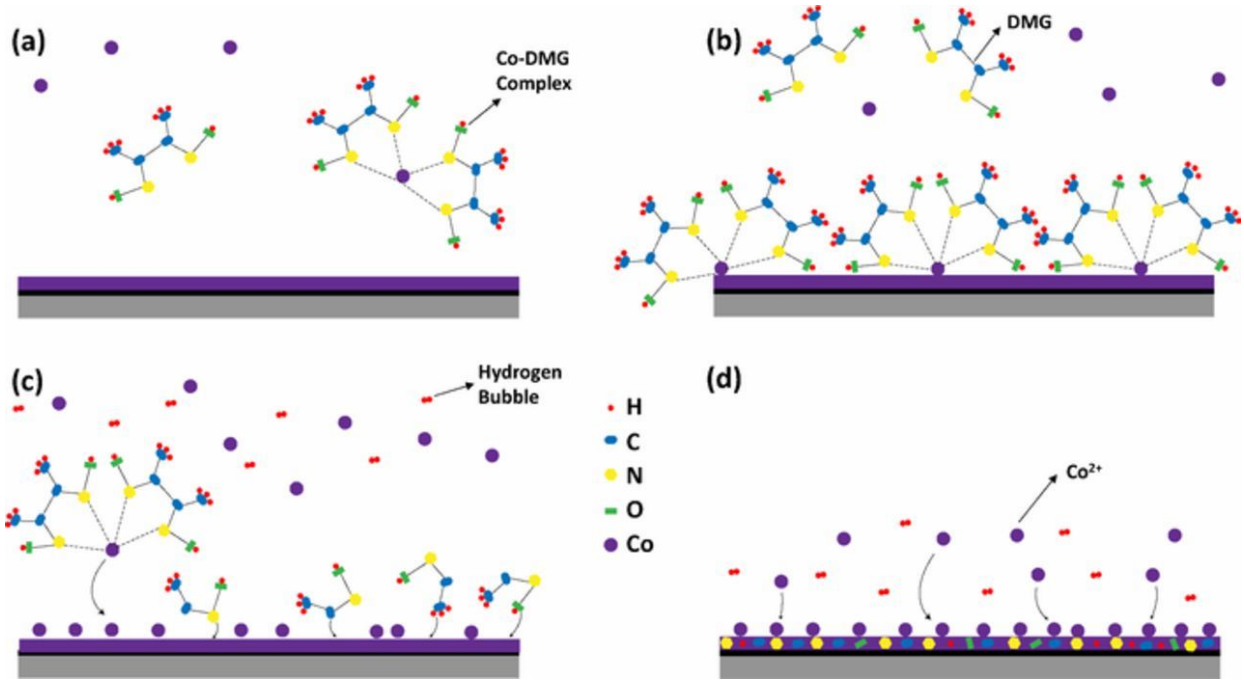

Figure 2-7. Diagrams showing the proposed two-step nucleation mechanism. (a) The solution contains Co^{2+}, DMG, and $Co(DMG)_2$ complex before reaction. (b) The adsorption of $Co(DMG)_2$ complex is stronger than Co^{2+}, and it preferably adsorbs on the electrode and prevents the adsorption of free Co^{2+} (c) Co^{2+} chelates reduction happens accompanying the hydrogen evolution reaction, which corresponds to the first current peak. (d) Co^{2+} reduction reaction happens accompanying the hydrogen evolution reaction, which corresponds to the second current peak. The reduction of $Co(DMG)_2$ results in a breakdown of suppression, incorporates organic fragments or elements into the film, and frees up electrode surface.

Upon the commence of deposition, the adsorbed $Co(DMG)_2$ complex would get incorporated into the Co film and the electrode surface is freed up. Such incorporation has been verified with second ion mass spectroscopy analysis (not shown here), where the carbon and cyanide impurity concentrations increased for about 5 and 20 times, respectively, upon the addition of DMG into electrolyte. The cyanide species is a direct measurement of

nitrogen in Co film due to DMG incorporation. While the electrode surface is freed up upon $Co(DMG)_2$ reduction and DMG incorporation, $Co(DMG)_2$ complex in electrolyte would preferably take up the empty active site, resulting a continuous reduction reaction of Co^{2+} chelates. Because the reduction potential of $Co(DMG)_2$ to Co metal is more negative than that of H^+ to H_2, the hydrogen evolution reaction inevitably occurs at the same time. In fact, the Co-dioxime chelate has been found a catalyst for hydrogen evolution reaction.[40] The combination of these two reactions corresponds to the first current peak in potentiostatic nucleation. As the chelate reduction continues, the chelate concentration in the vicinity of electrode decreases and the surface coverage of $Co(DMG)_2$ decreases. CoOH intermediate would eventually adsorb on the electrode upon the depletion of $Co(DMG)_2$ in solution. Subsequently, both the reduction of free Co^{2+} and hydrogen evolution would occur, resulting in the second nucleation current peak.

All the observations in this study can be explained with this proposed mechanism. Take DMG as an example, the concentration of $Co(DMG)_2$ complex in solution is pretty low when DMG concentration is 10 ppm (0.086 mM). Although the $Co(DMG)_2$ chelates reduction reaction occurs, its concentration is extremely low. Depletion of chelate in solution occurs soon after chelate reduction. The surface coverage of chelate is low and the impact on the reduction of free cation are believed to be minimal. The CoOH intermediate would take up most active sites and the current peak is mainly due to Co^{2+} reduction reaction. The concentration of $Co(DMG)_2$ complexes further increases upon the addition of 100 ppm (0.86 mM) DMG into the solution. The $Co(DMG)_2$ reduction reaction and hydrogen evolution reaction are strong enough to be seen as the first peak. In addition, it takes longer time to deplete the chelate in the vicinity of electrode and free up the surface for the reduction of free Co^{2+}, resulting in a delay of the second nucleation current peak. More $Co(DMG)_2$ complexes are formed with the addition of 300 ppm (2.58 mM) DMG. The height of the first peak rises

due to a high concentration of $Co(DMG)_2$ complexes and a higher hydrogen evolution reaction rate. On the other hand, the second current peak did not emerge up to 60 seconds at less negative potentials. At a high concentration of $Co(DMG)_2$, the complex in electrolyte would immediately adsorb on an active site on the electrode surface once such a site is freed up upon the reduction of an adsorbed chelate. Because the chelate reduction rate is slower at a less negative applied potential, it takes longer time to deplete $Co(DMG)_2$ complexes in the solution and it would take longer time than 60 seconds for the second current peak to evolve.

The same explanation can also be applied to the CHD studies. In this case, a much higher stability constant of $Co(CHD)_2$ than $Co(DMG)_2$ predicts a slower reduction of the adsorbed chelate at a same applied potential.[39] This translates to a slower depletion of the $Co(CHD)_2$ complex in the solution in the vicinity of electrode. Therefore, the $Co(CHD)_2$ chelates reduction reaction and hydrogen evolution reaction were observed as the first peak even at a lower concentration, 10 ppm (0.089 mM) CHD. The stronger suppression effect of CHD than DMG also resulted in a much more negative potential required for the chelate reduction and, therefore, a much lower current efficiency of Co deposition and a much lower cobalt nuclear density in galvanostatic nucleation.

A further discussion is provided here to validate the assignments of current peaks. The concentration of free Co^{2+} decreases and those of $Co(DMG)_2$ or $Co(CHD)_2$ complexes increase with the further addition of DMG or CHD. If free Co^{2+} reduction were assumed to result in the first current peak and chelate reduction as the second peak, the appearance of the second peak would have shifted earlier with the further addition of DMG or CHD as the time required to deplete free Co^{2+} would have decreased. This is however opposite to the observations.

Hydrogen evolution occurs inevitably throughout the nucleation studies and contributes to the current observed therein. However, it is believed that the hydrogen

evolution itself does not result in a stand-alone current peak. If the second peak were solely due to hydrogen evolution reaction, the hydrogen evolution reaction would have been more pronounced when more DMG or CHD was added since $Co(DMG)_2$ and $Co(CHD)_2$ complexes are catalysts for hydrogen evolution reaction. However, this is in contradictory with the observation in Figures 3c-3d. On the other hand, a dilemma is also encountered when the first peak is assigned to the hydrogen evolution reaction. If the first peak represented the hydrogen evolution reaction, the second peak would have been cobalt nucleation reaction, including the reduction of free Co^{2+} or chelates. Since the required potential for hydrogen evolution reaction is more positive than Co deposition, the only peak observed in 10 ppm (0.086 mM) DMG cases in Figure 2-3a should correspond to hydrogen evolution reaction. However, SEM images from galvanostatic study from galvanostatic study in figures 5d-5f clearly show that cobalt deposition occurs at various current densities for a small total charge, which corresponds to a deposition time well before the emerge of the only current peak in Figure 2-3a. Therefore, the hydrogen evolution reaction alone does not result in any of two current peaks whilst it occurs simultaneously with cobalt nucleation.

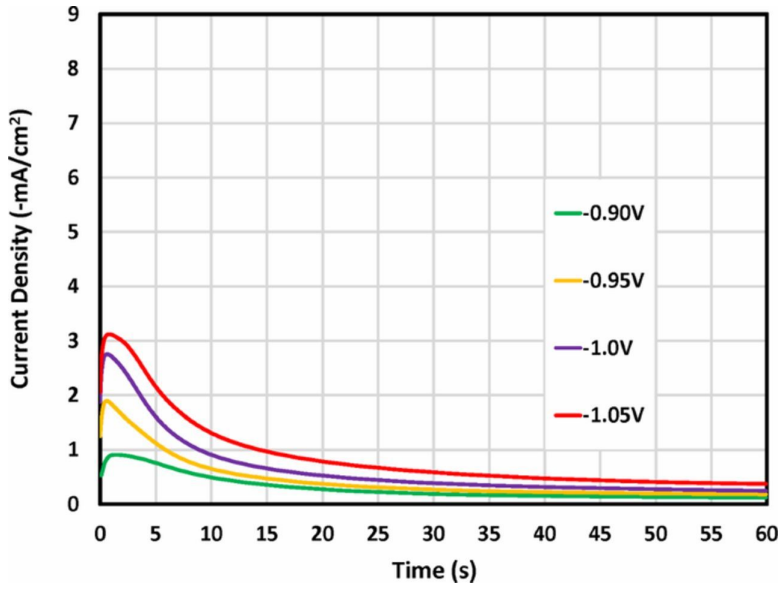

Figure 2-8. Current density-time transients for cobalt deposition on thin Co seed blanket wafer at different potentials with 0.4 mM Co and 100 ppm DMG in the solution.

Controlled experiment

The proposed mechanism was further confirmed with a control experiment, where 0.4 mM Co and 100 ppm (0.86 mM) DMG were used. In this study, no free Co^{2+} was expected to be present in the electrolyte because each Co^{2+} ion complexes with two DMG molecules,[41] forming a stable $Co(DMG)_2$ chelate. Figure 2-6 shows the current transients of the controlled experiments. Only one current peak was observed across all the potentials studied, corresponding to the first current peak in the two-peak cases in Figure 2-3. This current peak corresponds to the combination of Co^{2+} chelates reduction and hydrogen evolution, consistent with the proposed mechanism and the absence of free Co^{2+} cations.

Conclusions

The effects of DMG and CHD on cobalt nucleation process were studied on TiN substrate with extremely thin Co seed. CV study showed a typical 3D nucleation process controlled by hemispheric diffusion toward the nucleation centers. Potentiostatic studies showed several new findings: *i)* two current peaks were observed with the addition of DMG or CHD; *ii)* the height of first peak rises and the second peak diminishes upon the further addition of DMG or CHD; *iii)* the appearance of second peak delayed as the concentrations of DMG or CHD increase; *iv)* the addition of DMG or CHD suppressed the formation of cobalt nuclei dramatically. A two-step nucleation mechanism was proposed, involving i) a competitive surface adsorption between Co-dioxime chelate and monovalent Co intermediate, and ii) an incorporation of adsorbed chelate upon deposition and a release of surface adsorption site. The first current peak was therefore identified as the nucleation upon Co-dioxime chelate reduction, and the second peak as nucleation current from free Co^{2+} reduction. This mechanism was further confirmed with a controlled experiment, where only the first current peak was observed with all Co^{2+} being present as the chelate.

Galvanostatic DC deposition showed that CHD has stronger suppression effect on Co nucleation than DMG.

Acknowledgments

National Science Foundation is acknowledged for support through grant CMMI – 1662332. YH thanks the Graduate Council at University of Alabama for a fellowship support. Brett Baker-O'Neal at SUNY Polytech and Ahmed Shafaat at GlobalFoundries are acknowledged for providing the Co seed substrates for the studies. Central analytical facility at the University of Alabama is acknowledged for the access of equipment for characterization.

References

1. Steinhögl, W.; Schindler, G.; Steinlesberger, G.; Engelhardt, M., Size-dependent resistivity of metallic wires in the mesoscopic range. *Physical Review B* **2002,** *66* (7), 075414.

2. Wu, W.; Brongersma, S.; Van Hove, M.; Maex, K., Influence of surface and grain-boundary scattering on the resistivity of copper in reduced dimensions. *Appl. Phys. Lett.* **2004,** *84* (15), 2838-2840.

3. Zhang, W.; Brongersma, S. H.; Richard, O.; Brijs, B.; Palmans, R.; Froyen, L.; Maex, K., Influence of the electron mean free path on the resistivity of thin metal films. *Microelectron. Eng.* **2004,** *76* (1-4), 146-152.

4. Wei, C.-C.; Chou, E.; Shih, S.; Lin, S.-M. In *Bottom-up Filling of Damascene Trenches with Cobalt By Electroplating Process*, Meeting Abstracts, The Electrochemical Society: 2015; pp 949-949.

5. Kelly, J.; Chen, J.-C.; Huang, H.; Hu, C.; Liniger, E.; Patlolla, R.; Peethala, B.; Adusumilli, P.; Shobha, H.; Nogami, T. In *Experimental study of nanoscale Co damascene BEOL interconnect structures*, Interconnect Technology Conference/Advanced Metallization Conference (IITC/AMC), 2016 IEEE International, IEEE: 2016; pp 40-42.

6. West, A. C.; Mayer, S.; Reid, J., A superfilling model that predicts bump formation. *Electrochem. Solid-State Lett.* **2001,** *4* (7), C50-C53.

7. Moffat, T.; Wheeler, D.; Huber, W.; Josell, D., Superconformal electrodeposition of copper. *Electrochem. Solid-State Lett.* **2001,** *4* (4), C26-C29.

8. Moffat, T. P.; Wheeler, D.; Josell, D., Electrodeposition of copper in the SPS-PEG-Cl additive system I. Kinetic measurements: Influence of SPS. *J. Electrochem. Soc.* **2004,** *151* (4), C262-C271.

9. Akolkar, R.; Landau, U., A time-dependent transport-kinetics model for additive interactions in copper interconnect metallization. *J. Electrochem. Soc.* **2004,** *151* (11), C702-C711.

10. Vereecken, P. M.; Binstead, R. A.; Deligianni, H.; Andricacos, P. C., The chemistry of additives in damascene copper plating. *IBM Journal of Research and Development* **2005,** *49* (1), 3.

11. Gallaway, J. W.; West, A. C., PEG, PPG, and their triblock copolymers as suppressors in copper electroplating. *J. Electrochem. Soc.* **2008,** *155* (10), D632-D639.

12. Gallaway, J. W.; Willey, M. J.; West, A. C., Copper filling of 100 nm trenches using PEG, PPG, and a triblock copolymer as plating suppressors. *J. Electrochem. Soc.* **2009,** *156* (8), D287-D295.

13. Ahmed, S.; Huang, Q.; Cheng, T. J.; Findeis, P.; Koli, D. R.; Troung, C. N.; Grunow, S. In *Damascene Copper Plating Recipe Engineering for Defectivity, Health of Line (HOL) and Reliability Improvement*, Meeting Abstracts, The Electrochemical Society: 2016; pp 1909-1909.

14. Oskam, G.; Long, J.; Natarajan, A.; Searson, P., Electrochemical deposition of metals onto silicon. *J. Phys. D: Appl. Phys.* **1998,** *31* (16), 1927.

15. Correia, A.; Machado, S.; Avaca, L., Direct observation of overlapping of growth centres in Ni and Co electrocrystallisation using atomic force microscopy. *J. Electroanal. Chem.* **2000,** *488* (2), 110-116.

16. Bubendorff, J.; Meny, C.; Beaurepaire, E.; Panissod, P.; Bucher, J., Electrodeposited cobalt films: hcp versus fcc nanostructuring and magnetic properties. *The European Physical Journal B-Condensed Matter and Complex Systems* **2000,** *17* (4), 635-643.

17. Sahari, A.; Azizi, A.; Fenineche, N.; Schmerber, G.; Dinia, A., Electrochemical study of cobalt nucleation mechanisms on different metallic substrates. *Mater. Chem. Phys.* **2008,** *108* (2-3), 345-352.

18. Ramsperger, U.; Vaterlaus, A.; Pfaeffli, P.; Maier, U.; Pescia, D., Growth of Co on a stepped and on a flat Cu (001) surface. *Physical Review B* **1996,** *53* (12), 8001.

19. Azizi, A.; Sahari, A.; Felloussia, M.; Schmerber, G.; Mény, C.; Dinia, A., Growth and properties of electrodeposited cobalt films on Pt/Si (1 0 0) surface. *Appl. Surf. Sci.* **2004,** *228* (1-4), 320-325.

20. Mendoza-Huizar, L. H.; Rios-Reyes, C., Cobalt electrodeposition on polycrystalline palladium. Influence of temperature on kinetic parameters. *J. Solid State Electrochem.* **2012,** *16* (9), 2899-2906.

21. Gomez, E.; Marin, M.; Sanz, F.; Valles, E., Nano-and micrometric approaches to cobalt electrodeposition on carbon substrates. *J. Electroanal. Chem.* **1997,** *422* (1-2), 139-147.

22. Soto, A.; Arce, E.; Palomar-Pardave, M.; Gonzalez, I., Electrochemical nucleation of cobalt onto glassy carbon electrode from ammonium chloride solutions. *Electrochim. Acta* **1996,** *41* (16), 2647-2655.

23. Palomar-Pardavé, M.; González, I.; Soto, A. B.; Arce, E. M., Influence of the coordination sphere on the mechanism of cobalt nucleation onto glassy carbon. *J. Electroanal. Chem.* **1998,** *443* (1), 125-136.

24. Quinet, M.; Lallemand, F.; Ricq, L.; Hihn, J. Y.; Delobelle, P.; Arnould, C.; Mekhalif, Z., Influence of organic additives on the initial stages of copper electrodeposition on polycrystalline platinum. *Electrochim. Acta* **2009,** *54* (5), 1529-1536.

25. Huang, Q.; Lyons, T.; Sides, W., Electrodeposition of Cobalt for Interconnect Application: Effect of Dimethylglyoxime. *J. Electrochem. Soc.* **2016,** *163* (13), D715-D721.

26. Lyons, T.; Huang, Q., Effects of Cyclohexane-Monoxime and Dioxime on the Electrodeposition of Cobalt. *Electrochim. Acta* **2017,** *245*, 309-317.

27. Liang, D.; Liu, J.; Reuter, K.; Baker-O'Neal, B.; Huang, Q., Electroplating of Fe-Rich NiFe alloys in Sub-50 nm lines. *J. Electrochem. Soc.* **2014,** *161* (5), D301-D308.

28. Lee, C. H.; Bonevich, J. E.; Davies, J. E.; Moffat, T. P., Superconformal Electrodeposition of Co and Co–Fe Alloys Using 2-Mercapto-5-benzimidazolesulfonic Acid. *J. Electrochem. Soc.* **2009,** *156* (8), D301-D309.

29. Zheng, X.; Shi, Y.-N.; Lu, K., The Combination Addition of 2-Mercapto-5-benzimidazolesulfonic Acid and Thiourea to Watts Bath in Controllable Electro-Healing Cracks in Nickel. *J. Electrochem. Soc.* **2016,** *163* (8), D349-D354.

30. Oura, K.; Katayama, M.; Zotov, A.; Lifshits, V.; Saranin, A., Elementary Processes at Surfaces I. Adsorption and Desorption. In *Surf. Sci.*, Springer: 2003; pp 295-323.

31. Cottrell, F. G., Der Reststrom bei galvanischer Polarisation, betrachtet als ein Diffusionsproblem. *Z. Phys. Chem.* **1903,** *42* (1), 385-431.

32. Jeffrey, M.; Choo, W.; Breuer, P., The effect of additives and impurities on the cobalt electrowinning process. *Miner. Eng.* **2000,** *13* (12), 1231-1241.

33. Deligianni, H.; Romankiw, L. T., In situ surface pH measurement during electrolysis using a rotating pH electrode. *IBM Journal of Research and Development* **1993,** *37* (2), 85-95.

34. Hessami, S.; Tobias, C. W., A Mathematical Model for Anomalous Codeposition of Nickel-Iron on a Rotating Disk Electrode. *J. Electrochem. Soc.* **1989,** *136* (12), 3611-3616.

35. Gangasingh, D.; Talbot, J. B., Anomalous Electrodeposition of Nickel-Iron. *J. Electrochem. Soc.* **1991,** *138* (12), 3605-3611.

36. Radisic, A.; West, A. C.; Searson, P. C., Influence of additives on nucleation and growth of copper on n-Si (111) from acidic sulfate solutions. *J. Electrochem. Soc.* **2002,** *149* (2), C94-C99.

37. Huang, Q.; Deligianni, H.; Romankiw, L., Electrodeposition of gold on silicon nucleation and growth phenomena. *J. Electrochem. Soc.* **2006,** *153* (5), C332-C336.

38. Ramírez, C.; Arce, E. M.; Romero-Romo, M.; Palomar-Pardavé, M., The effect of temperature on the kinetics and mechanism of silver electrodeposition. *Solid State Ionics* **2004,** *169* (1-4), 81-85.

39. Martell, A. E.; Smith, R. M., *Critical stability constants*. Springer: 1974; Vol. 1.

40. Jacques, P.-A.; Artero, V.; Pécaut, J.; Fontecave, M., Cobalt and nickel diimine-dioxime complexes as molecular electrocatalysts for hydrogen evolution with low overvoltages. *Proceedings of the National Academy of Sciences* **2009,** *106* (49), 20627-20632.

41. Ma, F.; Jagner, D.; Renman, L., Mechanism for the electrochemical stripping reduction of the nickel and cobalt dimethylglyoxime complexes. *Anal. Chem.* **1997,** *69* (9), 1782-1784.

CHAPTER 3. INFLUENCE OF FURIL DIOXIME ON COBALT ELECTROCHEMICAL NUCLEATION AND GROWTH

Published Work Disclosure: This chapter is based on previously published paper (Hu, Y.; Lyons, T.; Huang, Q., Influence of Furil Dioxime on Cobalt Electrochemical Nucleation and Growth. J. Electrochem. Soc. 2020, 167 (2), 022509.)

Summary

The nucleation and growth of cobalt (Co) on blanket Si with extremely thin Co seed was studied in the presence of furil dioxime (FD). Cyclic voltammetry (CV), chronoamperometry, and galvanostatic nucleation studies were conducted to understand the effects of FD on Co nucleation process. A potential dependent suppression effect was observed at low potential with a breakdown of the suppression at high potential, resulting in a hysteresis in CV. The potentiostatic current transient experiments showed that side reactions and adsorption process both greatly affected Co nucleation. A well-established model, which deconvolutes the individual contributions to the total current transient, was applied to fit the experimental curves. Progressive and instantaneous Co nucleation were observed across different FD concentrations and applied potentials. Galvanostatic studies further proved the suppression effect of FD and the effects on film morphology were studied at different conditions.

Introduction

As the semiconductor integrated circuits evolve into 7 nm technology and beyond,[1] the concerns about copper (Cu) interconnects increase. The resistance of the finest copper lines at the ground rule metal level in back-end-of-line interconnects no longer linearly scales with dimension.[2-3] Instead, the resistivity starts to increase exponentially because the electron

scattering at grain boundaries and interfaces rapidly dominates the overall resistance.[4-5] High resistivity not only consumes more energy and demands faster heat dissipation, but also results in a greater RC delay in the circuit.[6] This cancels out the performance gain resulted from scaling and front-end device innovations. To address the resistivity issue, alternative metals like cobalt (Co) is thought as a promising material due to its higher melting point and shorter mean free path. The former relates to a lower risk of electromigration, whilst the latter decreases the contribution from electron scattering at grain boundaries and interfaces.

Copper bottom-up filling process has been well established.[7-15] Varieties of additives known as accelerator, suppressor and leveler were systematically classified.[16] Different influencing factors such as electrolyte,[14, 17-18] applied potential[19] were thoroughly investigated. Curvature Enhanced Accelerator Coverage (CEAC) mechanism[11] was proposed not only to explain how additives affect the Cu filling process but also to enable the filling of other metals such as gold,[20-22] silver[23-25] and nickel.[26] However, studies on Co electro-filling process has been rarely reported until recently. S-shaped negative differential resistance (S-NDR) mechanism was introduced to explain the superconformal Co electrodeposition in high aspect ratio through silicon vias (TSV).[27] Recently, defect-free filling of Co has been achieved using proprietary additives. The additives play an important role in such processes creating differential plating rates between the feature bottom and field regions because of a current efficiency difference[28-29] or a hydrogen-induced deactivation of additives.[30] Different functional groups in organic additives were found to influence the deposition kinetics.[31-34] In our previous study,[35-37] additives with a conjugated pair of oxime groups such as dimethylglyoxime (DMG) and cyclohexane dioxime (CHD) displayed strong suppression effects on Co deposition and a suppression breakdown occurred upon the reduction of adsorbed Co^{2+}-dioxime chelates.

Previous study[35] on the Co nucleation with DMG and CHD showed an interesting "two-peak" phenomenon, where two different nucleation peaks were observed in presence of these dioximes due to a hypothesized two-step reduction mechanism. This paper presents a study of the effects of furil dioxime (FD), a molecule with not only the pair of conjugated oxime groups but also additional multiple conjugated C=C bonds in the furil groups, on Co nucleation process. Cyclic voltammetry, galvanostatic deposition, potentiostatic nucleation, as well as numerical curve fitting were carried out not only to understand the effects of FD on Co deposition and nucleation but also to deconvolute the current contributions from nucleation and other competing reactions. A descriptive model of the nucleation process was provided.

Experimental

A traditional three-compartment electrochemical cell was used for the experimental studies, where the catholyte and anolyte were separated by a glass frit. A saturated calomel electrode (SCE, 0.24 V vs NHE) was used as the reference electrode, and all potentials were referred to this SCE in this report. The reference electrode compartment was connected to the catholyte through a capillary. The counter electrode was a Co foil with a surface area much larger than the cathode. Si coupons cleaved from a 12-inch blanket wafer with Co (5 nm, CVD) on TiN (5 nm, CVD) were used as cathodes. A circular deposition area of 0.385 cm^2 was defined with plating tape. The thin Co seed was used to mimic the substrates used in industry and to provide enough conductivity for the electrodeposition studies. However, this seed layer was not expected to be continuous and Co electrodeposition behavior was strongly influenced by the underneath TiN layer. The wafers were shipped and stored in ultrahigh pure nitrogen ambient until immediately before the experiments to minimize the surface oxidation. The substrates were used as received without further treatment.

The Co makeup solution for CV studies was the same as our previous study,[35] containing 0.3 M $CoSO_4 \cdot 7H_2O$, 0.4 M H_3BO_3, and 0.1 g l^{-1} sodium dodecyl sulfate (SDS). The pH was adjusted to 4.0 with H_2SO_4 and NaOH. Concentrated furil dixoime (FD) solutions (2800 ppm) were prepared by dissolving the corresponding chemical powder in a 1:1 water ethanol mixture. Calculated amounts of the concentrate were then added into the Co makeup solution up to various final concentrations. Another diluted version of Co makeup solution containing 0.01 M $CoSO_4 \cdot 7H_2O$, 0.1 M Na_2SO_4, 0.4 M H_3BO_3, and 0.1 g l^{-1} SDS with a pH of 4.0 was used to study the Co nucleation process. All salts and organic additives were at least ACS grade and used as received. Deionized (DI) water with a resistivity of 18.2 MOhm-cm was used in all studies.

Co nucleation was studied using electrochemical techniques (cyclic voltammetry, chronoamperometry and galvanostatic deposition). An Autolab 302 N potentiostat was used for all electrochemical studies. The chronoamperometry curves acquired during nucleation were analyzed and fit using the Polynomial Fit option in Origin™ 8.0. Surface morphology of the deposited Co nuclei was examined with a JEOL 7000 field emission scanning electron microscope (SEM) operated at 30 kV.

Results and Discussion

The impact of FD on Co electrodeposition was first studied with cyclic voltammetry (CV) in the Co makeup electrolytes. Figure 3-1 shows the CV results at different concentrations of FD. The current density started to decrease at around -0.70 V in the absence of FD, but the drop of current density at the beginning did not result from Co deposition. The chronoamperometry studies on the nucleation (Figure 3-2a) showed that the Co deposition started between -0.80 V and -0.85 V when no additive was added. Therefore, the initial decrease of the current density was considered as hydrogen evolution reaction. The addition of 10 ppm FD caused a minor suppression of Co deposition, where Co deposition was seen at

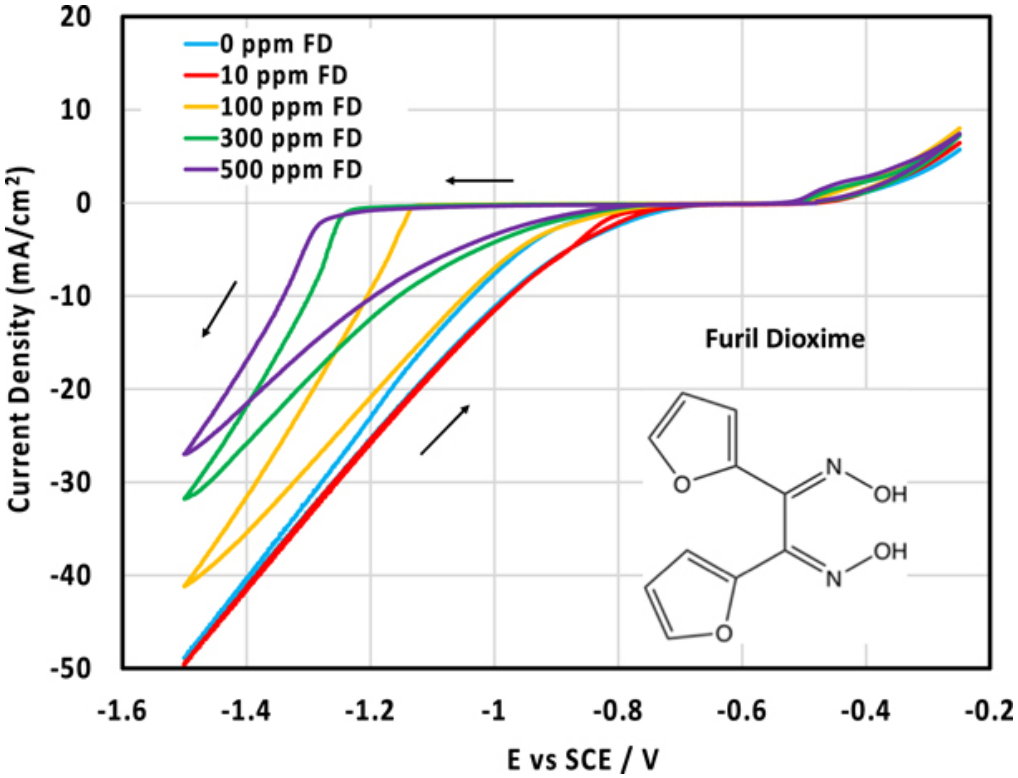

Figure 3-1. Cyclic voltammetry of Co electrodeposition at different FD concentrations.

a potential of -0.82 V. A small hysteresis was observed, where the current density was slightly higher on the reverse (anodic) sweep at around −0.82 V. Increasing FD concentration to 100 ppm further suppressed the Co deposition till up to -1.1 V. The deposition current density increased rapidly from -0.5 mA cm^{-2} to -10 mA cm^{-2} when the potential scanned from -1.10 V to -1.20 V. The Co deposition potential was further delayed to -1.23 V and -1.30 V with the addition of 300 ppm and 500 ppm FD, respectively. In our previous study,[37] the Co deposition potential was respectively delayed to -1.0 V and -1.05 V with the addition of 300 ppm DMG and CHD, which indicated that the suppression effect of FD was stronger than these two different dioxime additives. A pronounced hysteresis was observed for all the three cases with over 100 ppm FD. While a stronger suppression was observed in the forward scan when the FD concentration increased from 100 to 300 and 500 ppm, the deposition current extended to a same potential of about -0.85 V on the reverse scan for all three cases. The surface adsorption of Co^{2+}-dioxime complex and its reduction was proposed as the

mechanism for the suppression and consumption-based suppression breakdown. The higher stability constant between Co^{2+} and FD than DMG and CHD is consistent with the stronger suppression reported here.

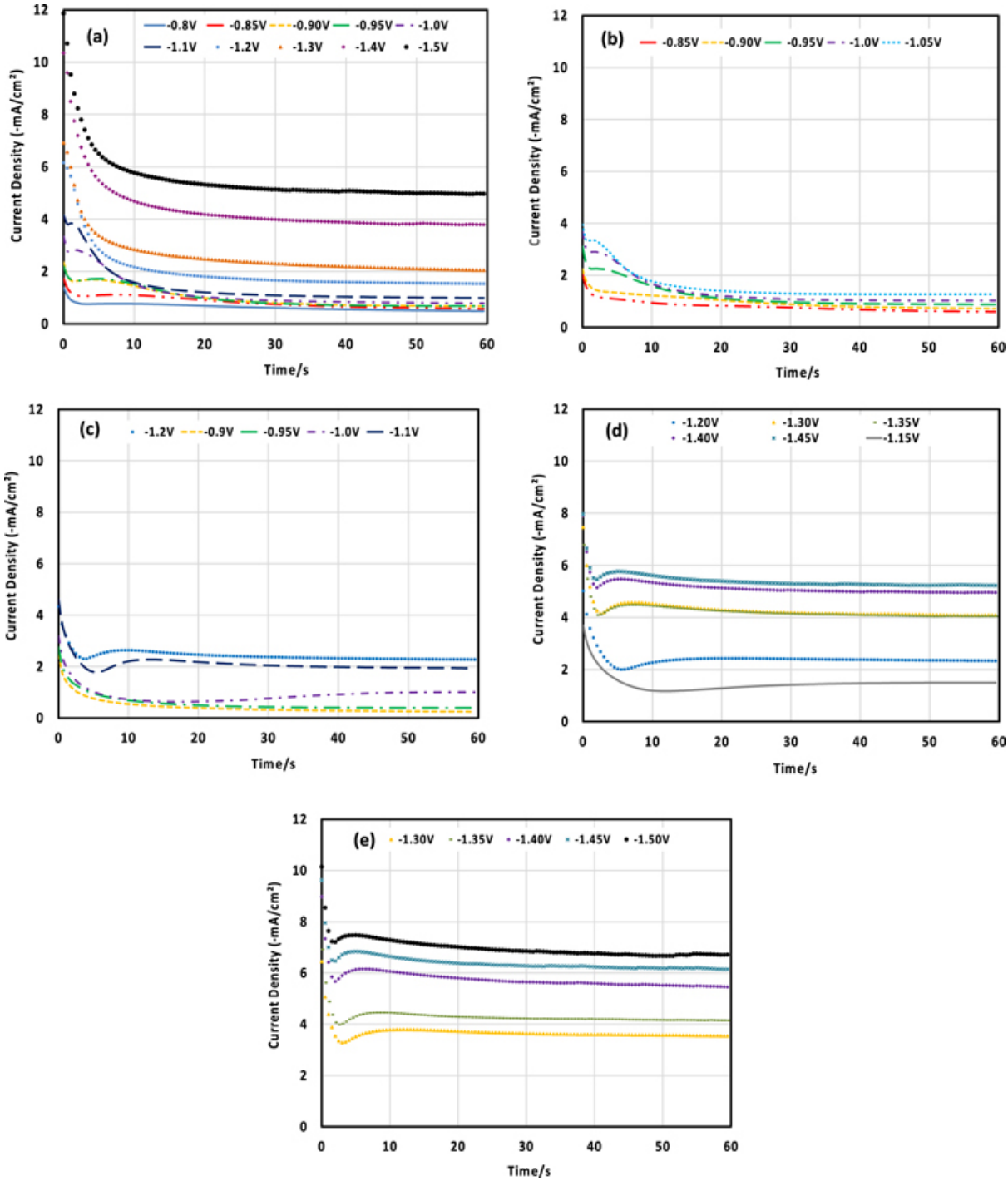

Figure 3-2. Current transients for cobalt deposition on thin Co seed blanket wafer at different potentials in 0.01 M Co solutions with (a) 0-ppm (b) 10-ppm (c) 100-ppm (d) 300-ppm (e) 500-ppm FD.

Figure 3-2 depicts families of potentiostatic current density transients obtained during cobalt nucleation and growth on blanket wafer at different overpotentials. Figure 3-2a shows the Co nucleation results without FD. Co nucleation did not happen at -0.80 V because the threshold overpotential for deposition was not reached, as discussed in the CV curves (Figure 3-1). It was clear that Co nucleation occurred at -0.85, -0.90, -0.95, -1.0, and -1.1 V. An initial sharp current decay was observed, which corresponded to the double layer charging and surface adsorption. The current decay is potential dependent and does not follow the $t^{-1/2}$ relation described by the Cottrell's equation for mass transport limited decay. Instead, it follows an exponential decay, a characteristic of capacitive behavior. This rapid decay was followed by a current rise due to an increase in the deposition area associated with nucleus formation on the substrate. After reaching a maximum, the current density gradually decreased again upon the development of a mass transport limited process. All cases at these five potentials followed the same trend. An ideal mass transport limited current decay during potentiostatic deposition can be described with the so-called Cottrell equation.[38] However, the currents in this study did not decay to 0 but stayed at a constant of around -1.5 mA cm^{-2}. This steady state current density was believed to relate to the side reactions such as the two below.

$$2H^+ + 2e \rightarrow H_2$$

$$2H_2O + 2e \rightarrow H_2 + 2OH^-$$

Since cobalt deposition occurs at a comparably negative potential, the hydrogen evolution reaction inevitably occurs. However, the nucleation current peaks were still evident in the curves because they emerged at a time where the capacitance currents had significantly decayed and the side reaction currents were low. On the other hand, the proton reduction and water reduction dominated the total current when the overpotential was more negative than -1.1 V, resulting in the rapid increase of steady state current density as the potential became

more negative. For example, while this current density was only around -1.5 mA cm^{-2} at -1.1 V, it reached -5.5 mA cm^{-2} at -1.5 V as the water reduction became more pronounced at such a negative potential.

Figure 3-2b shows the same current transients during Co nucleation with 10 ppm FD. Co nucleation did not take place at -0.85 or -0.90 V but -0.95 V due to the suppression effect of FD. It seemed to contradict with the CV results, where the Co deposition occurred at around -0.82 V with the addition of 10 ppm FD. However, it is worth noting that two different concentrations of Co, 0.3 M and 0.01 M, were separately used for CV and nucleation studies. The small amount of FD was not enough to completely deplete free Co^{2+} in either solution and the deposition behaviors were expected to be similar as there were plenty of Co^{2+} near the electrode. Nevertheless, the suppression effect would be more evident when a low overall concentration of Co^{2+} is used, which explains why more negative potential was required to initiate the Co deposition in the nucleation study. Figure 3-2c describes the same studies with 100 ppm FD, where a stronger suppression effect was observed. Co nucleation started at a more negative threshold potential of -1.0 V. As shown in Figures 3-2d and 3-2e, increasing the FD concentration to 300 ppm or 500 ppm further suppressed the Co nucleation. In addition, the higher FD concentration also resulted in a significant increase in the steady state current density. For instance, the magnitude of steady state current density at -1.4 V was 4 mA cm^{-2} in the FD-free electrolyte, while it increased to 5.5 mA cm^{-2} with 500 ppm FD. Co^{2+}-dioxime complex is known to act as an electrocatalyst for hydrogen evolution reactions.[39-40] While the detailed chemical mechanism and the exact speciation of the catalyst are still under debate,[41-43] the Co cation chelated with multiple N-atoms and the conjugated C=C and C=N double bonds in the organic molecule is expected to be involved. It is believed that such a complex accelerated the production of hydrogen on the surface of newly deposited Co,[44] resulting in the increase of steady state current density.

The current transient curves during potentiostatic nucleation of Co with a simpler dioxime molecule, dimethylglyoxime or DMG, were reported previously to show two current peaks, resulting from a two-step reduction reaction. The first peak corresponded to the reduction of Co^{2+}-dioxime chelate adsorbed on the surface, and the reduction of free Co^{2+} cations was responsible for the second peak. While such double peak curves were not observed in this study, it is believed that the two-step deposition mechanism remains the same in presence of FD. The Co^{2+} reduction reaction is related to the nucleation peak in the FD-free electrolyte. As the potential decreases to below -1.2 V, the proton and water reduction reactions gradually become more pronounced and dominant. When 10 ppm FD is added into the solution, only a small amount of Co-FD complexes are formed and the majority of Co^{2+} cations remain free in the solution. The nucleation curves are similar to the FD-free cases.

In the presence of 100 ppm or more FD, the complexed Co^{2+}-FD chelates are still of a small fraction of the total Co^{2+}. The complex adsorbs on an active site on the electrode resulting in strong suppression. Subsequently, the Co^{2+} chelate reduction reaction occurs upon the application of a voltage more negative than the threshold value and the chelate is quickly reduced. Co nuclei are formed on the electrode and the organic fragments of dioxime are desorbed from electrode or get incorporated into the film during this process. Immediately afterwards, the reduction of free Co^{2+} cation starts. These two Co reduction processes both lead to nuclei formed on the electrode and an increase of the overall reactive area. They would have also resulted in two distinct nucleation peaks in an ideal situation. However, the strong suppression effect of FD requires a highly negative potential to overcome, at which the reduction of free Co^{2+} becomes extremely rapid. Therefore, the Cottrell decay is expected to occur immediately upon the reduction of Co-FD complex, convoluting the two nucleation steps. In addition, and probably more importantly, the surface

area of nuclei increases rapidly and the hydrogen evolution reaction on the newly emerged surface becomes so overwhelming at these potentials that they not only amplify the nucleation current, i.e. the increase of nucleus surface area, but also further mask and convolute the two nucleation current peaks. It is believed that this "amplification effect" is the main reason for the single nucleation peak observed across all high FD concentrations.

Metal deposition on foreign substrates including thin seeded substrate typically follows the so-called Volmer-Weber three-dimensional nucleation with diffusion-controlled growth of nuclei.[45-46] Such behaviors have been well studied and mathematically described.[47-48] For the two extreme cases, the ideal progressive and instantaneous nucleation processes, the current transient responses for a potential step on a stagnant electrode are described by the following equations:

Instantaneous nucleation

$$i(t) = \frac{zFD^{1/2}c}{\pi^{1/2}t^{1/2}}[1 - \exp(-N\pi kDt)]$$

Progressive nucleation

$$i(t) = \frac{zFD^{1/2}c}{\pi^{1/2}t^{1/2}}\left[1 - \exp\left(-\frac{1}{2}AN_{\infty}\pi k'Dt^2\right)\right]$$

where z is the number of electrons transferred during Co nucleation, F is the Faraday constant, D is the diffusion coefficient of Co^{2+}, c is the bulk concentration of Co^{2+}, t is the time, A is the steady state nucleation rate constant per site, N is the number of nuclei, N_{∞} is the maximum number of nuclei obtainable, k and k' are dimensionless constant, where $k = (8\pi cM/\rho)^{1/2}$ and $k' = 4/3(8\pi cM/\rho)^{1/2}$. A simplified form can be obtained by nondimensionalizing the current and time with the values at the current peak, i_{max} and t_{max}.

Instantaneous nucleation

$$\frac{i(t)}{i_{max}} = \left\{\frac{1.9542}{(t/t_{max})}\left[1 - \exp\left(-1.2564\frac{t}{t_{max}}\right)\right]^2\right\}^{1/2}$$

Progressive nucleation

$$\frac{i(t)}{i_{max}} = \left\{\frac{1.2254}{(t/t_{max})}\left[1 - \exp\left(-2.3367\left(\frac{t}{t_{max}}\right)^2\right)\right]^2\right\}^{1/2}$$

The nucleation current transients in Figure 3-2 where a current peak was observed were normalized with the current peaks and are presented together with the ideal instantaneous and progressive nucleation cases in Figure S 3-1 in Supplemental Material. Since the total current is the result of different processes, and cannot be treated as Co nucleation alone, the deviation of experimental data from ideal model is observed in all cases studied. Efforts are therefore aimed to deconvolute the total current density following a method proposed by Manuel Palomar-Pardavé et al., where the side reactions and adsorption process were taken into consideration.[49-53] Hydrogen produced in the side reactions are assumed to dissolve into the electrolyte or detach from the electrode immediately upon formation. Such detachment is possible as SDS is used in the electrolytes as a surfactant. However, the bubbles have to be extremely small so that the agitation effect of such detachments can be negligible during the nucleation process. While the experimental quantification of the effects of hydrogen bubble is extremely challenging and worth future exploration, the assumption here that the hydrogen produced from the side reaction does not block the electrode surface simplifies the decomposition of the total current. The contributions from diffusion controlled 3-dimensional nucleation and growth, $i_{3D}(t)$, as well as other processes including the capacitive adsorption, $i_{ad}(t)$, and side reactions on the surface of Co nuclei, $i_{side}(t)$, can be described with the following equations.

$$i_{total}(t) = i_{ad}(t) + i_{3D}(t) + i_{side}(t)$$

$$i_{ad}(t) = i_{ad0} \exp\left(-t/\tau_{ad}\right)$$

$$i_{3D}(t) = C_{cottrell}\, t^{-\frac{1}{2}} \frac{\phi}{\varphi}\, \theta(t)$$

$$i_{side}(t) = C_{side}\, \frac{\phi}{\varphi}\, \theta(t)$$

In these equations, i_{ad0}, τ_{ad}, $C_{cottrell}$, and C_{side} are time independent constants characterizing various processes. While some of them can be further described with physical parameters, some only depend on empirical parameters. Nevertheless, these time independent constants can be potential dependent and therefore can be obtained by fitting experimental current transients at different potentials. On the other hand, θ is the actual fraction of area covered by diffusion zone, ϕ is the "retardation" of the current by slow nucleation,[54] and φ is the "retardation" of the growth of the extended coverage.[54] The ratio between ϕ and φ represents a correction factor to covert the projected 2D extended surface coverage, θ, into the actual 3D surface area of nuclei. All these three are time dependent parameters and have to be further described as functions of time with time independent coefficients, as shown in following equations.

$$\theta(t) = 1 - \exp\left[-C_{coverage} \cdot t \cdot \varphi(t)\right]$$

$$\varphi(t) = 1 - \frac{1-\exp(-At)}{At}$$

$$\phi(t) = 1 - \frac{\exp(-At)}{(At)^{\frac{1}{2}}} \int_0^{(At)^{\frac{1}{2}}} \exp(\lambda^2)\, d\lambda \cong 1 - \frac{0.0513 + 0.479 \cdot (A \cdot t)^{\frac{1}{2}}}{\left[1 - 1.207 \cdot (A \cdot t)^{\frac{1}{2}} + 1.186 \cdot (A \cdot t)\right] \cdot (A \cdot t)^{\frac{1}{2}}}$$

The numerical values of A, the steady state nucleation rate constant per site, and other parameters such as $C_{coverage}$ are both independent of time and could be obtained by fitting the current transient curves. Thus, the model described can be used to fit the experimental Co current transients and allow the deconvolution of each different contribution during the Co nucleation. Overall, there are six fit parameters, i_{ad0}, τ_{ad}, $C_{cottrell}$, C_{side}, $C_{coverage}$, and A, all of which are all potential or additive concentration dependent.

Figure 3-3 shows some examples of experimental current transients at different potentials and FD concentrations and the current breakdown obtained with non-linear fitting of the experimental data. The fit parameters are listed in Table 1. It can be seen that i_{ad0} and τ_{ad} are strongly dependent on the applied potential, but the effect of additive concentration is

Table 3-1. The fit parameters used to decompose the experimental current transients

Potential (V)	FD concentration	i_{ad0} (mA/cm^2)	$1/\tau_{ad}$ (s^{-1})	$C_{cottrell}$ (mA/cm^{2}s$^{1/2}$)	C_{side} (mA/cm^2)	$C_{coverage}$ (s^{-1})	A (s^{-1})
-1.0V	0-ppm	2.7300	0.21377	1.27475	0.58594	2.29474	0.20237
-1.0V	10-ppm	3.2155	0.21853	1.20417	0.83724	0.61919	0.55943
-1.2V	100-ppm	5.6418	0.78972	2.05634	1.98398	0.32457	1.49307
-1.2V	300-ppm	4.9966	0.46934	1.95293	2.06556	0.16650	2.65070
-1.4V	500-ppm	8.7783	0.41869	0.49378	5.35393	0.46385	0.46211

minimal. On the other hand, the two parameters describing surface coverage and cobalt nucleation rate, $C_{coverage}$ and A, are strongly dependent on the additive concentration. The time independent prefixed ratio constants for the time dependent current transients of Co deposition and hydrogen evolution reaction, $C_{cottrell}$ and C_{side}, respectively, are mainly dependent on the diffusion coefficients of cation species and are both relatively independent of additive concertation. Figure 3-3(a) shows the Co nucleation at -1.0 V without FD. It is evident that the experimental current transient can be well described with the theoretical equations with the fit parameters. The adsorption process started immediately when the potential was applied and this capacitive current decayed to a negligible value after 23 seconds. The Co nucleation and side reaction also started simultaneously upon the application of potential, gradually increasing with time. The descriptive model here assumed that both the Co nucleus growth and hydrogen evolution reactions only occurred on the Co nuclei. Therefore, both currents increased simultaneously along with the surface coverage, θ, corrected with the ratio between the 3-dimensional surface area and the 2-dimensional coverage projected on the electrode surface, ϕ/φ. As the deposition continued, the Co nucleation current density, i_{3D}, gradually became governed by the Cottrell decay, as described by the $t^{-\frac{1}{2}}$ term, resulting in a current peak. On the other hand, the side reaction remained at a constant after 10 seconds because the surface coverage, θ, approaches 1, and the water molecules were in excessive amount. Figure 3-3(b) shows the Co nucleation at -1.0 V with 10 ppm FD. The steady state current density for side reactions slightly increased. This was believed to relate to the catalytic effect of $Co(FD)_2$

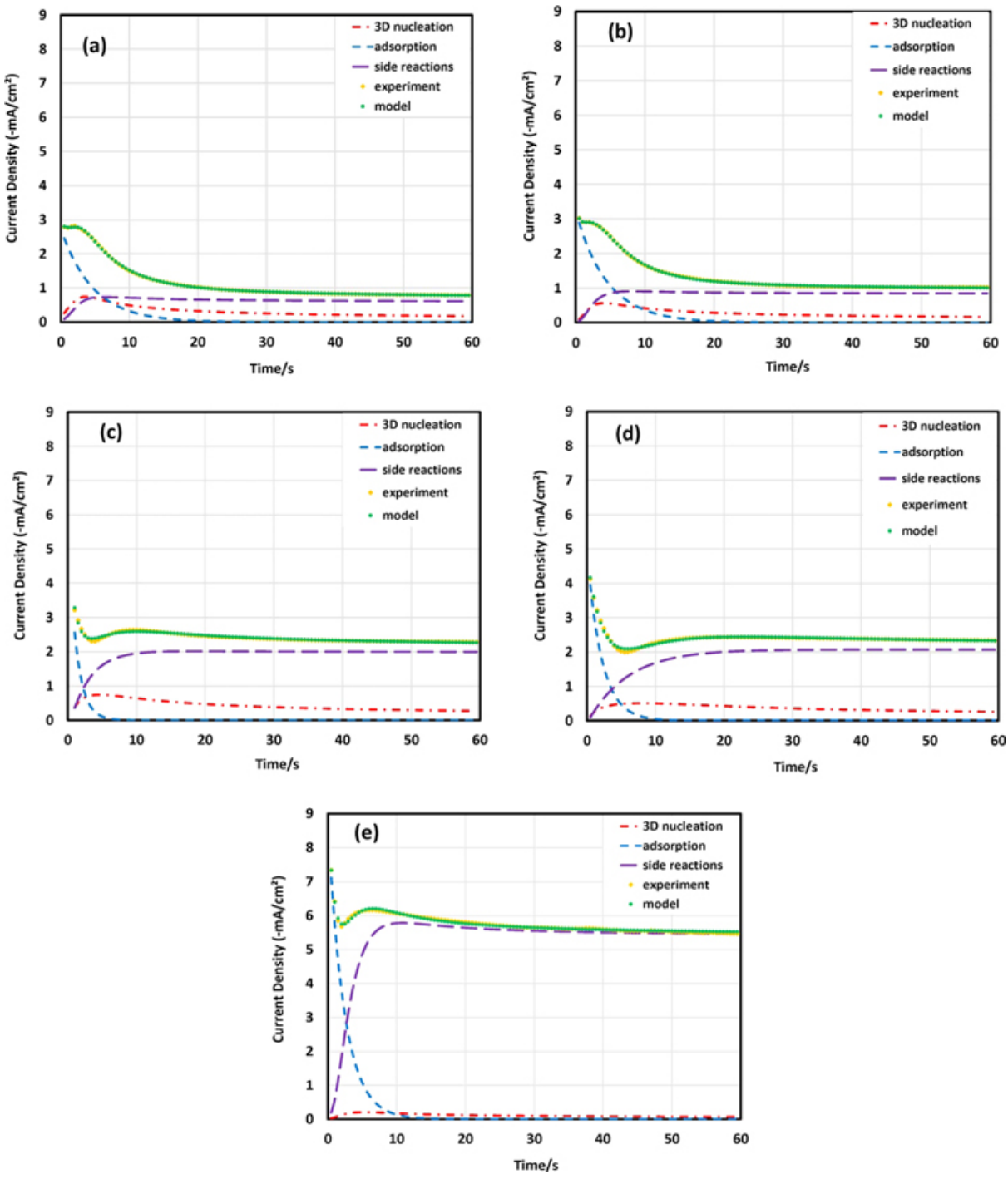

Figure 3-3. Individual contributions to the experimental Co nucleation current transients due to the adsorption process, Co nucleation process and side reactions at (a) 0-ppm, −1.0 V (b) 10-ppm, −1.0 V (c) 100-ppm, −1.2 V (d) 300-ppm, −1.2 V (e) 500-ppm, −1.4 V.

for hydrogen evolution reaction. Due to the presence of conjugated C=C bonds and the C=N bonds, the catalytic effect was expected to be even stronger than those without conjugated C=C bonds such as DMG and CHD.[55] On the other hand, the current density for Co nucleation

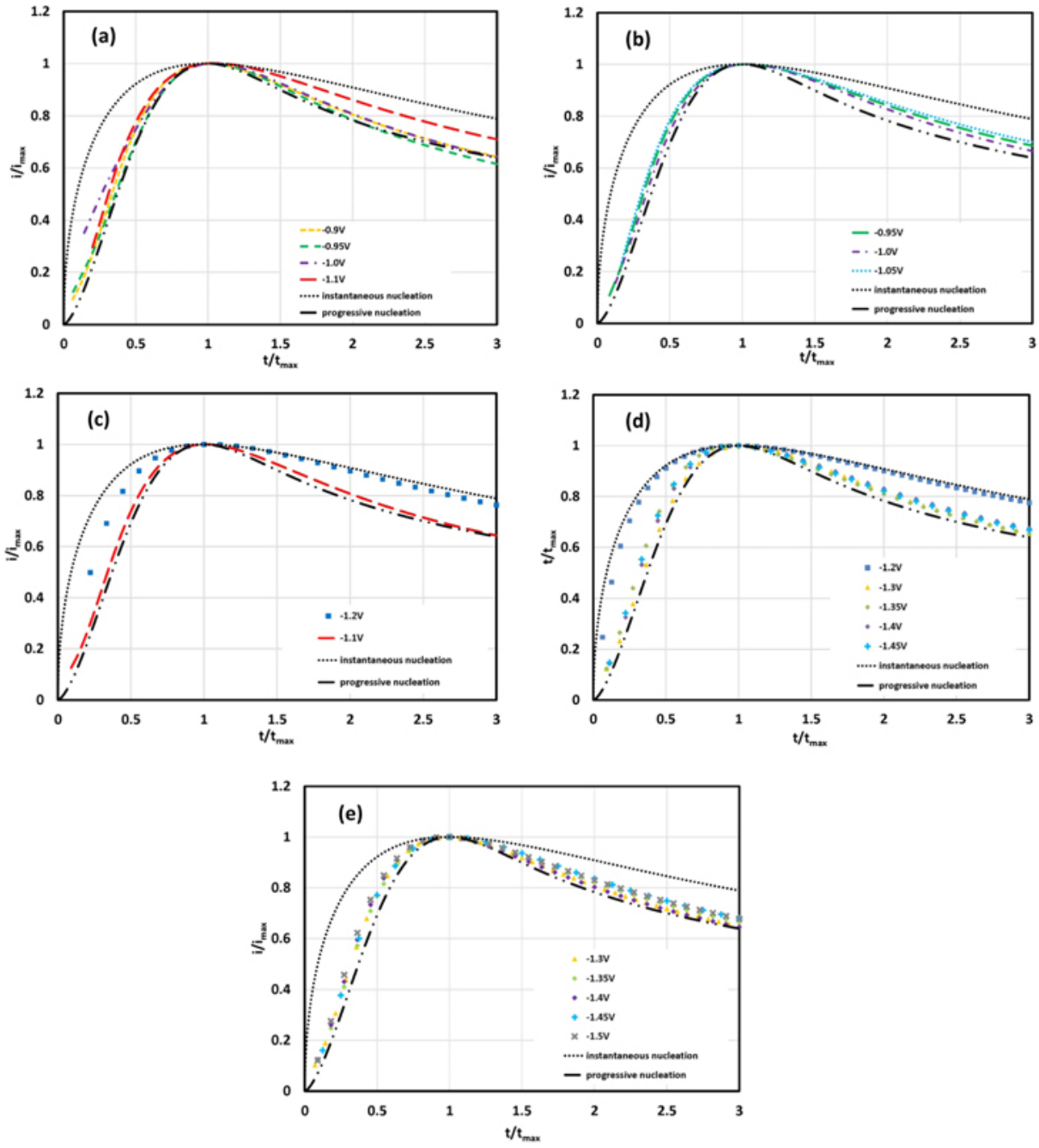

Figure 3-4. Comparison of experimental normalized Co nucleation current transients with instantaneous and progressive nucleation model at (a) 0-ppm (b) 10-ppm (c) 100-ppm (d) 300-ppm (e) 500-ppm FD.

remained unchanged or slightly decreased from the FD-free case because of the suppression effect of FD on Co deposition. Figures 3-3(c-d) show the decomposed current densities during Co nucleation with two FD concentrations at -1.2 V, where a similar trend was observed in both cases. Namely, as the FD increased from 100 ppm to 300 ppm, the current density of side

reaction increased whilst Co nucleation current slightly dropped. The enhancement of side reaction was insignificant in this case, where the catalytic effect of $Co(FD)_2$ had been saturated at this applied potential. Figure 3-3(e) shows the Co nucleation with 500 ppm FD at -1.4 V, where an overwhelming water reduction was clearly observed.

The numerical fitting and deconvolution of the chronoamperometry curves not only allow to break down the contributions of different electrochemical reactions on the surface, but also enable further analysis of the nucleation behavior. Figure 3-4 shows the Co nucleation current transients obtained from the numerical fitting shown in Figure 3-3, normalized with the current peak. The ideal progressive and instantaneous nucleation processes were also included for comparison. It was interesting to find that almost all the Co cases studied followed a progressive nucleation process. The two exceptions were the cases with 100 ppm and 300 ppm FD at -1.2 V, where a more instantaneous nucleation character was observed. Progressive nucleation has been widely observed in electrochemical deposition of metal on non-metallic substrates, such as Si and glassy carbon.[49, 56-57] The TiN substrate used in this study was expected to have a thin layer of oxide, resulting in a non-metallic surface.

Galvanostatic deposition at different current densities of -2, -4 and -10 mA cm^{-2} were carried out to microscopically examine the effects of FD on Co nucleation. A constant charge density of -15.58 mC cm^{-2} was used. The deposition time needed for this charge density varied up to 7.79 s, corresponding to a small portion at the beginning of current transients shown in Figure 3-2. Figure 3-5 shows the top down SEM images of deposits. Needle-shaped Co nuclei were deposited from the additive free electrolyte. Nuclei with various sizes were observed, consistent with the progressive nucleation behavior determined on the current transients in Figure 3-4. Deposition at -4 mA cm^{-2} resulted in the highest density and the largest size of Co nuclei, which may correspond to the highest current efficiency. Little suppression effect was observed at a low concentration of 10 ppm FD on Co deposition, consistent with the results

from electrochemical studies. The nucleation density significantly decreased as the FD concentration increased to 100 ppm at -4 mA cm^{-2}, and a smaller size of cobalt nuclei was observed at -2 and -10 mA cm^{-2}. A change in nucleus shape and decrease in nucleus number were observed upon the further addition of FD up to 300 ppm. Spherical Co nuclei in addition to the needle-shaped ones were observed across all current densities studied. Specifically, the number of Co nuclei drastically decreased and only two spherical Co nuclei were observed at -4 mA cm^{-2}. The addition of 500 ppm FD resulted in little difference compared with the 300 ppm FD case. One interesting finding was that there were more needle-shaped Co nuclei at -2 mA cm^{-2} with 500 ppm FD. However, more spherical Co nuclei were formed at -10 mA cm^{-2}.

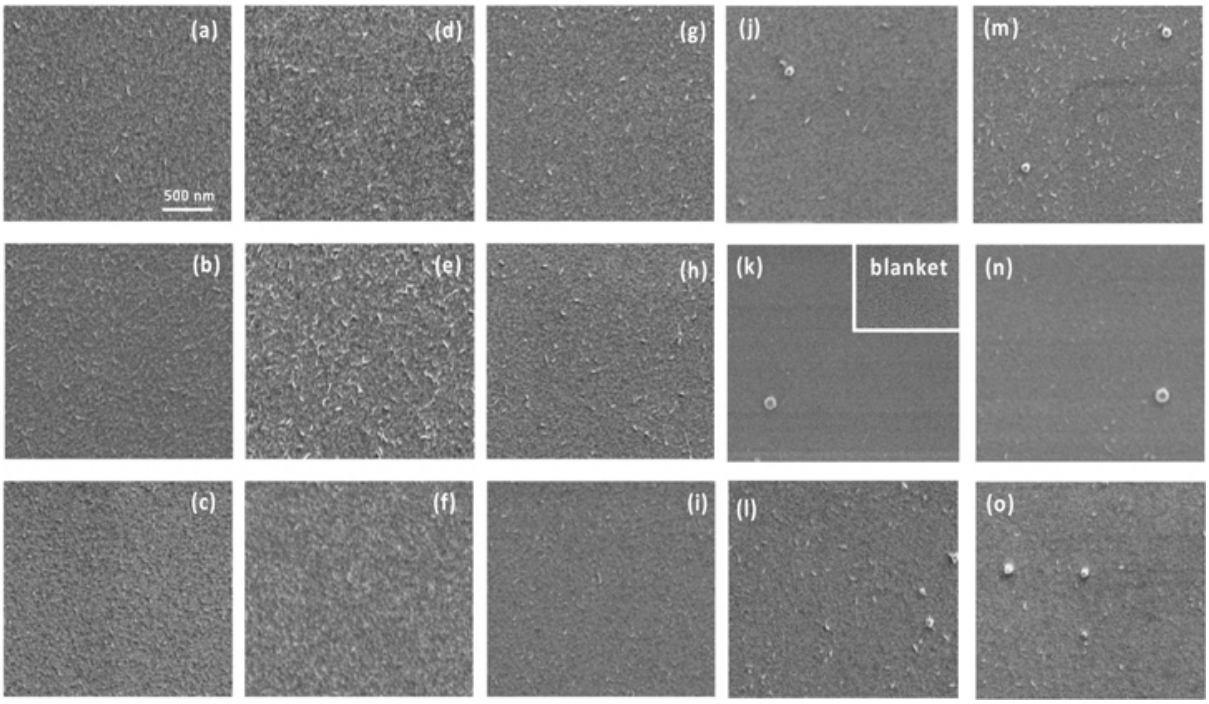

Figure 3-5. SEM images of cobalt nuclei deposited thin Co seed blanket wafer from solution containing 0.01 M Co with (a-c) 0, (d-f) 10, (g-i) 100, (j-l) 300, (m-o) 500 ppm FD at (a,d,g,j,m) -2, (b,e,h,k,n) -4, and (c,f,I,l,o) -10 mA cm^{-2}. The total deposition charge was -15.58 mC cm^{-2}. The blanket substrate was shown in (k).

Galvanostatic deposition with extended deposition time was conducted to further study the morphology of Co film, i.e., the growth of Co grains. In this set of experiments, Co deposition was respectively conducted at -2 and -4 mA cm^{-2} for 500 s with the addition of 100

ppm FD in 0.01 M Co solution. Figure 3-6 shows the top down SEM images of the deposits. The Co nuclei grew much bigger with the grains of 100 nm. However, needle-shaped ridges of Co grains were still evident regardless of the deposition current used in the study. Also, fewer Co nuclei with needle-shaped ridge were observed at -4 mA cm^{-2} than -2 mA cm^{-2}.

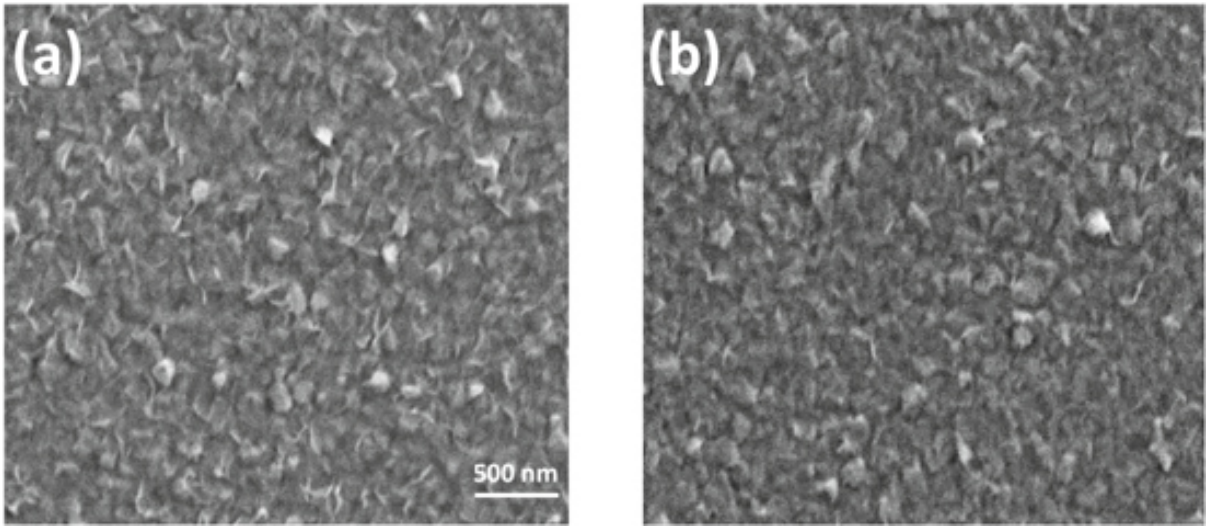

Figure 3-6. SEM images of cobalt nuclei deposited thin Co seed blanket wafer from solution containing 0.01 M Co with (a) 100-ppm FD and -2 mA cm^{-2} (b) 100-ppm FD and -4 mA cm^{-2} for 500 s.

Surfactants are known to alter the crystal growth behavior by selectively adsorbing and blocking certain crystalline facets.[58-60] The crystals formed therein grow preferably in the unblocked facets and result in planes or ridges in different directions. A lower current is expected to allow the nuclei or grains to grow at a more equilibrium state, where a strong influence by the surfactant adsorbates would be expected. On the other hand, a higher current density may force the crystals to grow even at the facets with surfactant adsorbate, resulting in less ridges and more randomly shaped grains, as observed in Figure 3-6b.

Conclusions

The effect of a dioxime molecule with conjugated C=C bonds, furil dioxime, on Co electrodeposition was studied. Suppression effect on Co deposition by FD was observed in CV

as well as chronoamperometry nucleation studies. While the threshold potential for nucleation decreased upon the increase of FD concentration, the reduction reactions of proton and water were much facilitated at the same time. The total current transients during potentiostatic nucleation were deconvoluted into contributions from the capacitive charging, 3-D Co nucleation and growth, and the surface area dependent side reaction. Not only the $Co(FD)_2$ complex was confirmed to enhance the side reaction rate, but also the initial Co deposition was found to follow the progressive nucleation behavior for almost all cases. Galvanostatic deposition along with electron microscopic characterization was carried out and the nucleus shape, nucleation density as well as the morphology of thick films were found highly dependent on the FD concentration and deposition current.

Acknowledgments

National Science Foundation is acknowledged for support through Grant CMMI-1662332. YH thanks the Graduate Council at University of Alabama for a fellowship support. Brett Baker-O'Neal at SUNY Polytech and Ahmed Shafaat at GlobalFoundries were acknowledged for providing the Co seed substrates for the studies. Central analytical facility at the University of Alabama is acknowledged for the access of equipment for characterization.

References

1. Steinhögl, W.; Schindler, G.; Steinlesberger, G.; Engelhardt, M., Size-dependent resistivity of metallic wires in the mesoscopic range. *Physical Review B* **2002,** *66* (7), 075414.

2. Wu, W.; Brongersma, S.; Van Hove, M.; Maex, K., Influence of surface and grain-boundary scattering on the resistivity of copper in reduced dimensions. *Appl. Phys. Lett.* **2004,** *84* (15), 2838-2840.

3. van der Veen, M. H.; Heyler, N.; Pedreira, O. V.; Ciofi, I.; Decoster, S.; Gonzalez, V. V.; Jourdan, N.; Struyf, H.; Croes, K.; Wilson, C. In *Damascene Benchmark of Ru, Co and Cu in Scaled Dimensions*, 2018 IEEE International Interconnect Technology Conference (IITC), IEEE: 2018; pp 172-174.

4. Graham, R. L.; Alers, G.; Mountsier, T.; Shamma, N.; Dhuey, S.; Cabrini, S.; Geiss, R. H.; Read, D. T.; Peddeti, S., Resistivity dominated by surface scattering in sub-50 nm Cu wires. *Appl. Phys. Lett.* **2010,** *96* (4), 042116.

5. Wang, P.-I.; Frey, M. D.; Washington, M.; Nayak, S.; Lu, T.-M., Resistivity of sub-50 nm copper lines epitaxially grown on Si (100) substrate. *Thin Solid Films* **2012,** *520* (19), 6106-6108.

6. He, M.; Zhang, X.; Nogami, T.; Lin, X.; Kelly, J.; Kim, H.; Spooner, T.; Edelstein, D.; Zhao, L., Mechanism of Co liner as enhancement layer for Cu interconnect gap-fill. *J. Electrochem. Soc.* **2013,** *160* (12), D3040-D3044.

7. Wei, C.-C.; Chou, E.; Shih, S.; Lin, S.-M. In *Bottom-up Filling of Damascene Trenches with Cobalt By Electroplating Process*, Meeting Abstracts, The Electrochemical Society: 2015; pp 949-949.

8. Hayase, M.; Taketani, M.; Aizawa, K.; Hatsuzawa, T.; Hayabusa, K., Copper bottom-up deposition by breakdown of PEG-Cl inhibition. *Electrochem. Solid-State Lett.* **2002,** *5* (10), C98-C101.

9. Moffat, T.; Wheeler, D.; Huber, W.; Josell, D., Superconformal electrodeposition of copper. *Electrochem. Solid-State Lett.* **2001,** *4* (4), C26-C29.

10. Moffat, T. P.; Bonevich, J.; Huber, W.; Stanishevsky, A.; Kelly, D.; Stafford, G.; Josell, D., Superconformal electrodeposition of copper in 500–90 nm features. *J. Electrochem. Soc.* **2000,** *147* (12), 4524-4535.

11. Moffat, T. P.; Wheeler, D.; Edelstein, M. D.; Josell, D., Superconformal film growth: Mechanism and quantification. *IBM Journal of Research and Development* **2005,** *49* (1), 19-36.

12. Cha, S. H.; Kim, S.-S.; Cho, S. K.; Kim, J. J., Copper bottom-up filling by electroplating without any additives on patterned wafer. *Electrochem. Solid-State Lett.* **2007,** *10* (2), D22-D24.

13. Lee, C. H.; Lee, S. C.; Kim, J. J., Bottom-up filling in Cu electroless deposition using bis-(3-sulfopropyl)-disulfide (SPS). *Electrochim. Acta* **2005,** *50* (16-17), 3563-3568.

14. Chang, C.; Lu, X.; Lei, Z.; Wang, Z.; Zhao, C., 2-Mercaptopyridine as a new leveler for bottom-up filling of micro-vias in copper electroplating. *Electrochim. Acta* **2016,** *208*, 33-38.

15. Lu, X.; Yao, L.; Ren, S.; Wang, Z., A study of bottom-up electroplated copper filling by the potential difference between two rotating speeds of a working electrode. *J. Electroanal. Chem.* **2014,** *712*, 25-32.

16. Broekmann, P.; Fluegel, A.; Emnet, C.; Arnold, M.; Roeger-Goepfert, C.; Wagner, A.; Hai, N.; Mayer, D., Classification of suppressor additives based on synergistic and antagonistic ensemble effects. *Electrochim. Acta* **2011,** *56* (13), 4724-4734.

17. Kelly, J. J.; West, A. C., Copper deposition in the presence of polyethylene glycol I. Quartz crystal microbalance study. *J. Electrochem. Soc.* **1998,** *145* (10), 3472-3476.

18. Kelly, J. J.; West, A. C., Copper deposition in the presence of polyethylene glycol II. Electrochemical impedance spectroscopy. *J. Electrochem. Soc.* **1998,** *145* (10), 3477-3481.

19. Reid, J., Copper electrodeposition: principles and recent progress. *Japanese journal of applied physics* **2001,** *40* (4S), 2650.

20. Josell, D.; Moffat, T., Extreme bottom-up filling of through silicon vias and damascene trenches with gold in a sulfite electrolyte. *J. Electrochem. Soc.* **2013,** *160* (12), D3035-D3039.

21. Josell, D.; Beauchamp, C.; Kelley, D.; Witt, C.; Moffat, T., Gold superfill in sub-micrometer trenches. *Electrochem. Solid-State Lett.* **2005,** *8* (3), C54-C57.

22. Josell, D.; Wheeler, D.; Moffat, T. P., Gold superfill in submicrometer trenches: Experiment and prediction. *J. Electrochem. Soc.* **2006,** *153* (1), C11-C18.

23. Baker, B.; Freeman, M.; Melnick, B.; Wheeler, D.; Josell, D.; Moffat, T. P., Superconformal electrodeposition of silver from a KAg (CN) 2 KCN KSeCN electrolyte. *J. Electrochem. Soc.* **2003,** *150* (2), C61-C66.

24. Moffat, T. P.; Baker, B.; Wheeler, D.; Bonevich, J. E.; Edelstein, M.; Kelly, D.; Gan, L.; Stafford, G. R.; Chen, P.; Egelhoff, W., Superconformal electrodeposition of silver in submicrometer features. *J. Electrochem. Soc.* **2002,** *149* (8), C423-C428.

25. Baker, B.; Witt, C.; Wheeler, D.; Josell, D.; Moffat, T. P., Superconformal silver deposition using KSeCN derivatized substrates. *Electrochem. Solid-State Lett.* **2003,** *6* (5), C67-C69.

26. Josell, D.; Baker, B.; Witt, C.; Wheeler, D.; Moffat, T. P., Via filling by electrodeposition superconformal silver and copper and conformal nickel. *J. Electrochem. Soc.* **2002,** *149* (12), C637-C641.

27. Josell, D.; Silva, M.; Moffat, T. P., Superconformal Bottom-Up Cobalt Deposition in High Aspect Ratio Through Silicon Vias. *J. Electrochem. Soc.* **2016,** *163* (14), D809-D817.

28. Rigsby, M. A.; Brogan, L. J.; Doubina, N. V.; Liu, Y.; Opocensky, E. C.; Spurlin, T. A.; Zhou, J.; Reid, J. D., Superconformal Cobalt Fill through the Use of Sacrificial Oxidants. *ECS Transactions* **2017,** *80* (10), 767-776.

29. Rigsby, M. A.; Brogan, L. J.; Doubina, N. V.; Liu, Y.; Opocensky, E. C.; Spurlin, T. A.; Zhou, J.; Reid, J. D., The Critical Role of pH Gradient Formation in Driving Superconformal Cobalt Deposition. *J. Electrochem. Soc.* **2019,** *166* (1), D3167-D3174.

30. Wu, J.; Wafula, F.; Branagan, S.; Suzuki, H.; van Eisden, J., Mechanism of Cobalt Bottom-Up Filling for Advanced Node Interconnect Metallization. *J. Electrochem. Soc.* **2019,** *166* (1), D3136-D3141.

31. Quinet, M.; Lallemand, F.; Ricq, L.; Hihn, J. Y.; Delobelle, P.; Arnould, C.; Mekhalif, Z., Influence of organic additives on the initial stages of copper electrodeposition on polycrystalline platinum. *Electrochim. Acta* **2009,** *54* (5), 1529-1536.

32. Liang, D.; Liu, J.; Reuter, K.; Baker-O'Neal, B.; Huang, Q., Electroplating of Fe-Rich NiFe alloys in Sub-50 nm lines. *J. Electrochem. Soc.* **2014,** *161* (5), D301-D308.

33. Lee, C. H.; Bonevich, J. E.; Davies, J. E.; Moffat, T. P., Superconformal Electrodeposition of Co and Co–Fe Alloys Using 2-Mercapto-5-benzimidazolesulfonic Acid. *J. Electrochem. Soc.* **2009,** *156* (8), D301-D309.

34. Zheng, X.; Shi, Y.-N.; Lu, K., The Combination Addition of 2-Mercapto-5-benzimidazolesulfonic Acid and Thiourea to Watts Bath in Controllable Electro-Healing Cracks in Nickel. *J. Electrochem. Soc.* **2016,** *163* (8), D349-D354.

35. Hu, Y.; Huang, Q., Effects of Dimethylglyoxime and Cyclohexane Dioxime on the Electrochemical Nucleation and Growth of Cobalt. *J. Electrochem. Soc.* **2019,** *166* (1), D3175-D3181.

36. Huang, Q.; Lyons, T.; Sides, W., Electrodeposition of Cobalt for Interconnect Application: Effect of Dimethylglyoxime. *J. Electrochem. Soc.* **2016,** *163* (13), D715-D721.

37. Lyons, T.; Huang, Q., Effects of Cyclohexane-Monoxime and Dioxime on the Electrodeposition of Cobalt. *Electrochim. Acta* **2017,** *245*, 309-317.

38. Cottrell, F. G., Der Reststrom bei galvanischer Polarisation, betrachtet als ein Diffusionsproblem. *Z. Phys. Chem.* **1903,** *42* (1), 385-431.

39. Jacques, P.-A.; Artero, V.; Pécaut, J.; Fontecave, M., Cobalt and nickel diimine-dioxime complexes as molecular electrocatalysts for hydrogen evolution with low overvoltages. *Proceedings of the National Academy of Sciences* **2009,** *106* (49), 20627-20632.

40. Ma, F.; Jagner, D.; Renman, L., Mechanism for the electrochemical stripping reduction of the nickel and cobalt dimethylglyoxime complexes. *Anal. Chem.* **1997,** *69* (9), 1782-1784.

41. Valdez, C. N.; Dempsey, J. L.; Brunschwig, B. S.; Winkler, J. R.; Gray, H. B., Catalytic hydrogen evolution from a covalently linked dicobaloxime. *Proceedings of the National Academy of Sciences* **2012,** *109* (39), 15589-15593.

42. McCrory, C. C.; Uyeda, C.; Peters, J. C., Electrocatalytic hydrogen evolution in acidic water with molecular cobalt tetraazamacrocycles. *JACS* **2012,** *134* (6), 3164-3170.

43. Kaeffer, N.; Morozan, A.; Fize, J.; Martinez, E.; Guetaz, L.; Artero, V., The dark side of molecular catalysis: diimine–dioxime cobalt complexes are not the actual hydrogen evolution electrocatalyst in acidic aqueous solutions. *ACS Catalysis* **2016,** *6* (6), 3727-3737.

44. Kaeffer, N.; Chavarot-Kerlidou, M.; Artero, V., Hydrogen evolution catalyzed by cobalt diimine–dioxime complexes. *Acc. Chem. Res.* **2015,** *48* (5), 1286-1295.

45. Oura, K.; Lifshits, V.; Saranin, A.; Zotov, A.; Katayama, M., *Surface science: an introduction*. Springer Science & Business Media: 2013.

46. Electrochemical nucleation: part I. general considerations. *J. Electroanal. Chem. Interfac. Electrochem.* **1982,** *138*, 225.

47. Scharifker, B.; Mostany, J., Three-dimensional nucleation with diffusion controlled growth: Part I. Number density of active sites and nucleation rates per site. *Journal of electroanalytical chemistry and interfacial electrochemistry* **1984,** *177* (1-2), 13-23.

48. Mostany, J.; Mozota, J.; Scharifker, B., Three-dimensional nucleation with diffusion controlled growth: Part II. The nucleation of lead on vitreous carbon. *Journal of electroanalytical chemistry and interfacial electrochemistry* **1984,** *177* (1-2), 25-37.

49. Palomar-Pardavé, M.; Scharifker, B.; Arce, E.; Romero-Romo, M., Nucleation and diffusion-controlled growth of electroactive centers: Reduction of protons during cobalt electrodeposition. *Electrochim. Acta* **2005,** *50* (24), 4736-4745.

50. Aldana-González, J.; Romero-Romo, M.; Robles-Peralta, J.; Morales-Gil, P.; Palacios-González, E.; Ramírez-Silva, M.; Mostany, J.; Palomar-Pardavé, M., On the electrochemical formation of nickel nanoparticles onto glassy carbon from a deep eutectic solvent. *Electrochim. Acta* **2018,** *276*, 417-423.

51. Mendoza-Huizar, L. H.; Robles, J.; Palomar-Pardavé, M., Nucleation and growth of cobalt onto different substrates: Part I. Underpotential deposition onto a gold electrode. *J. Electroanal. Chem.* **2002,** *521* (1-2), 95-106.

52. Mendoza-Huizar, L. H.; Robles, J.; Palomar-Pardavé, M., Nucleation and growth of cobalt onto different substrates: Part II. The upd-opd transition onto a gold electrode. *J. Electroanal. Chem.* **2003,** *545*, 39-45.

53. Mejía-Caballero, I.; Aldana-González, J.; Le Manh, T.; Romero-Romo, M.; Arce-Estrada, E.; Campos-Silva, I.; Ramírez-Silva, M.; Palomar-Pardavé, M., Mechanism and kinetics of chromium electrochemical nucleation and growth from a choline chloride/ethylene glycol deep eutectic solvent. *J. Electrochem. Soc.* **2018,** *165* (9), D393-D401.

54. Heerman, L.; Tarallo, A., Theory of the chronoamperometric transient for electrochemical nucleation with diffusion-controlled growth. *J. Electroanal. Chem.* **1999,** *470* (1), 70-76.

55. A computational study of the mechanism of hydrogen evolution by cobalt (diimine-dioxime) catalysts. *Chem.—Eur. J.* **2013,** *19*, 15166.

56. Electrochemistry of gold deposition on n-Si (100). *J. Electrochem. Soc.* **2000,** *147*, 2199.

57. Munoz, A.; Salinas, D.; Bessone, J., First stages of Ni deposition onto vitreous carbon from sulfate solutions. *Thin Solid Films* **2003,** *429* (1-2), 119-128.

58. Wang, C.; Wang, Y.; Cheng, Y.; Huang, W.; Zou, B.; Cao, X., Effects of surfactants on the structure and crystal growth behavior of Sm2Zr2O7 nanocrystalline. *Powder Technol.* **2012,** *225*, 130-135.

59. Kandel, D.; Kaxiras, E., Surfactant mediated crystal growth of semiconductors. *Phys. Rev. Lett.* **1995,** *75* (14), 2742.

60. Mosquera-Giraldo, L. I.; Trasi, N. S.; Taylor, L. S., Impact of surfactants on the crystal growth of amorphous celecoxib. *Int. J. Pharm.* **2014,** *461* (1-2), 251-257.

Supporting Information

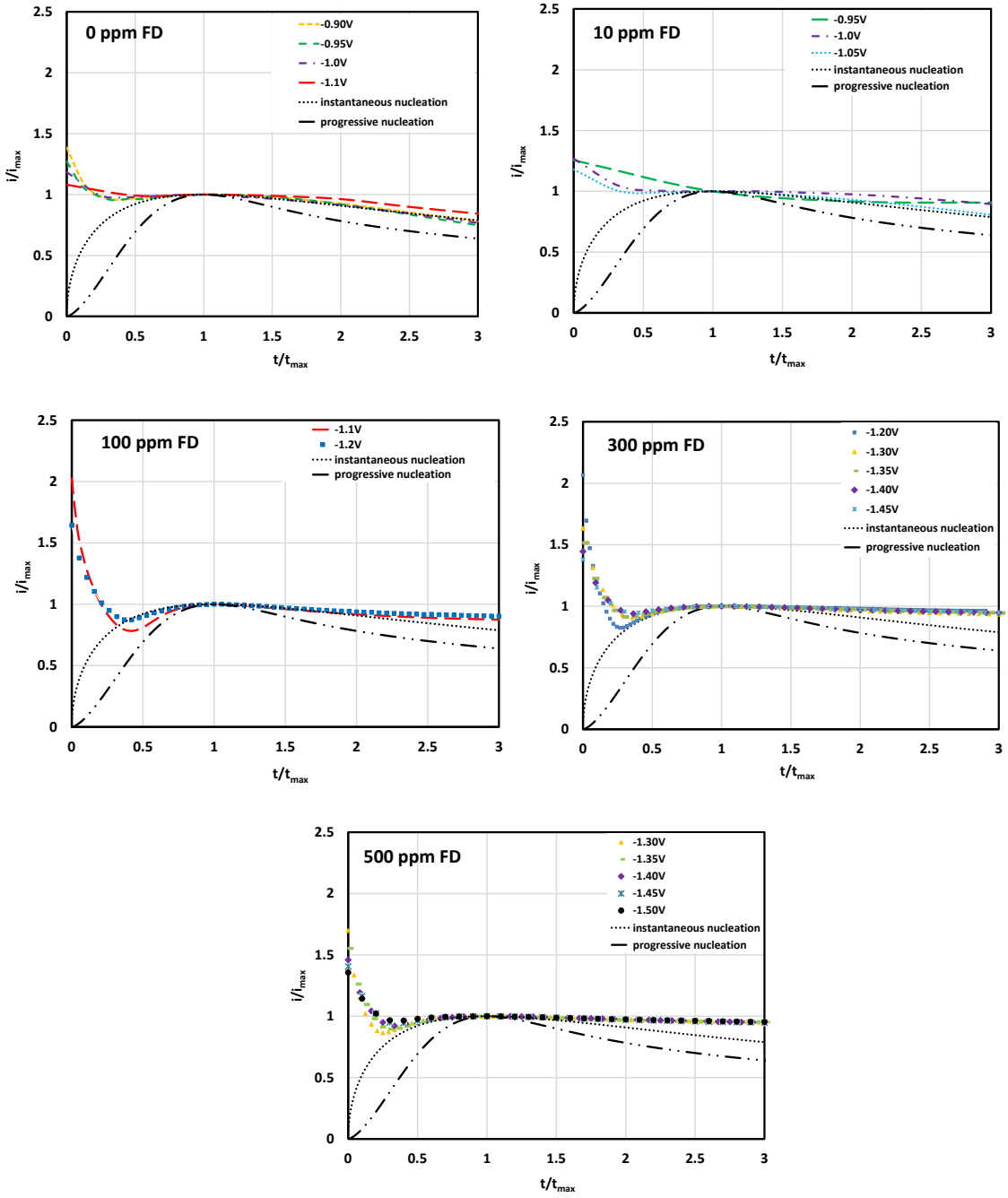

Figure S 3-1. shows the normalized Co nucleation current transients at different concentrations of FD together with the ideal instantaneous and progressive nucleation cases. For 0 and 10 ppm cases, the experimental data fit well with the ideal instantaneous nucleation model when $t/t_{max} > 1$, but these $i - t$ plots significantly deviate from the ideal case when $t/t_{max} < 1$. The deviation becomes even more evident as FD concentration increases. When 100, 300, and 500 ppm FD are added to the solution, a significant deviation from the ideal case is observed across the entire time scale. While the capacitive current causes the deviation at $t/t_{max} < 1$, side reactions such as hydrogen evolution or water reduction are believed to be responsible for the deviation at $t/t_{max} > 1$.

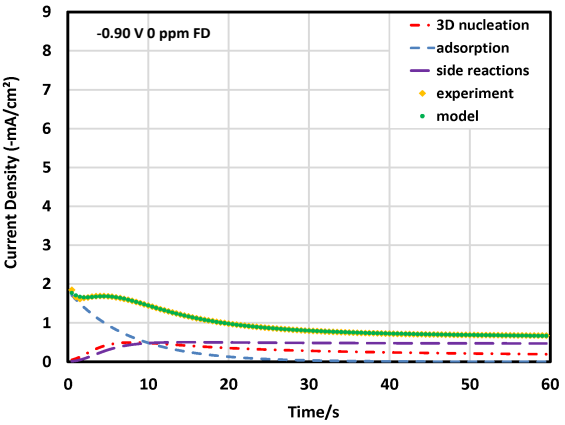
-0.90 V 0 ppm FD
3D nucleation
adsorption
side reactions
experiment
model
Current Density (-mA/cm²)
Time/s

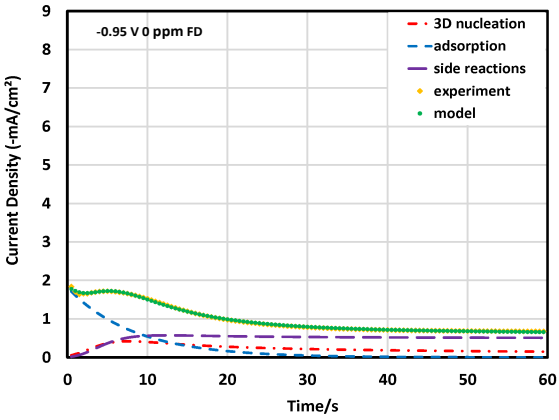
-0.95 V 0 ppm FD
3D nucleation
adsorption
side reactions
experiment
model
Current Density (-mA/cm²)
Time/s

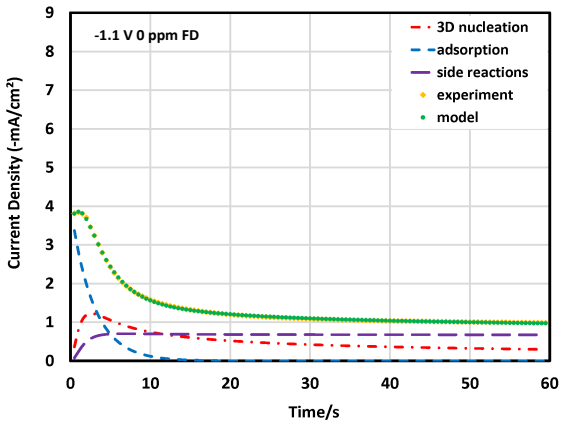
-1.1 V 0 ppm FD
3D nucleation
adsorption
side reactions
experiment
model
Current Density (-mA/cm²)
Time/s

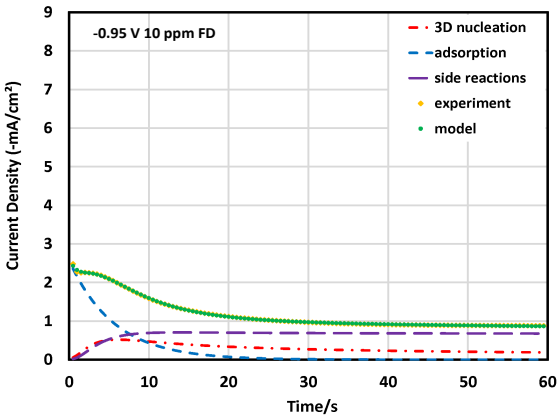
-0.95 V 10 ppm FD
3D nucleation
adsorption
side reactions
experiment
model
Current Density (-mA/cm²)
Time/s

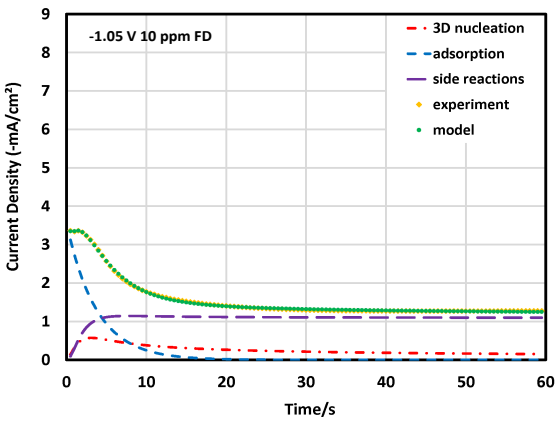
-1.05 V 10 ppm FD
3D nucleation
adsorption
side reactions
experiment
model
Current Density (-mA/cm²)
Time/s

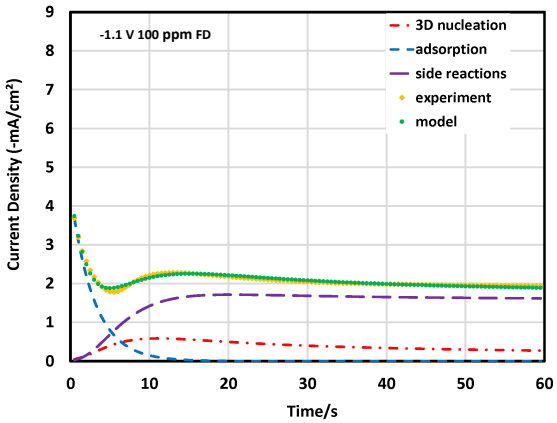
-1.1 V 100 ppm FD
3D nucleation
adsorption
side reactions
experiment
model
Current Density (-mA/cm²)
Time/s

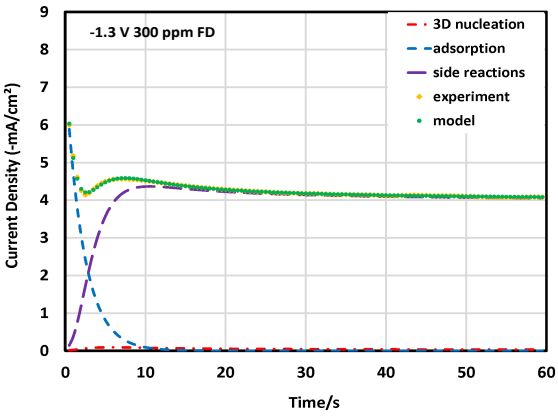
-1.3 V 300 ppm FD
3D nucleation
adsorption
side reactions
experiment
model
Current Density (-mA/cm²)
Time/s

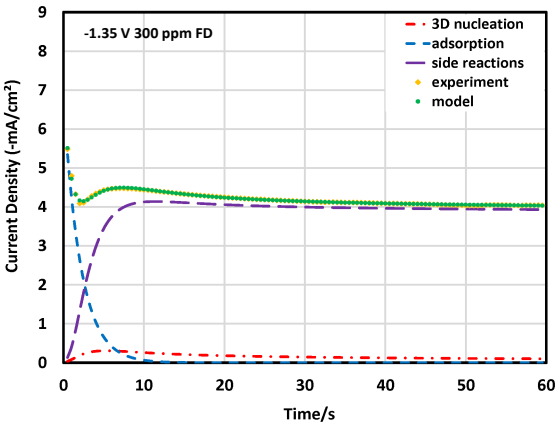
-1.35 V 300 ppm FD
3D nucleation
adsorption
side reactions
experiment
model
Current Density (-mA/cm²)
Time/s

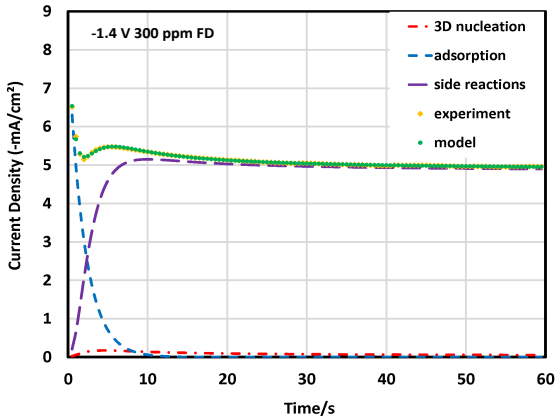
-1.4 V 300 ppm FD
3D nucleation
adsorption
side reactions
experiment
model
Current Density (-mA/cm²)
Time/s

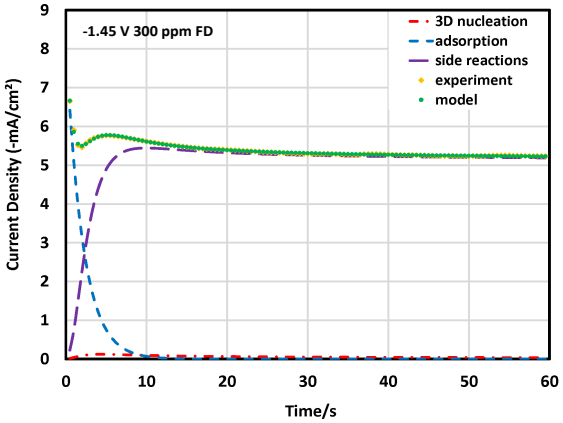
-1.45 V 300 ppm FD
3D nucleation
adsorption
side reactions
experiment
model
Current Density (-mA/cm²)
Time/s

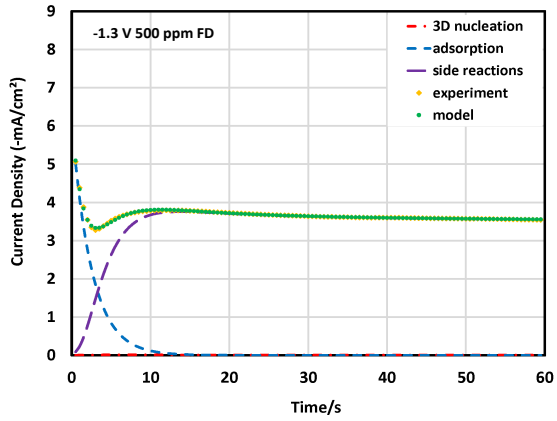
-1.3 V 500 ppm FD
3D nucleation
adsorption
side reactions
experiment
model
Current Density (-mA/cm²)
Time/s

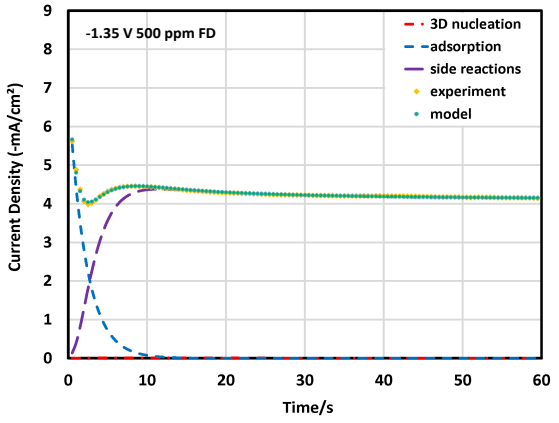
-1.35 V 500 ppm FD
3D nucleation
adsorption
side reactions
experiment
model
Current Density (-mA/cm²)
Time/s

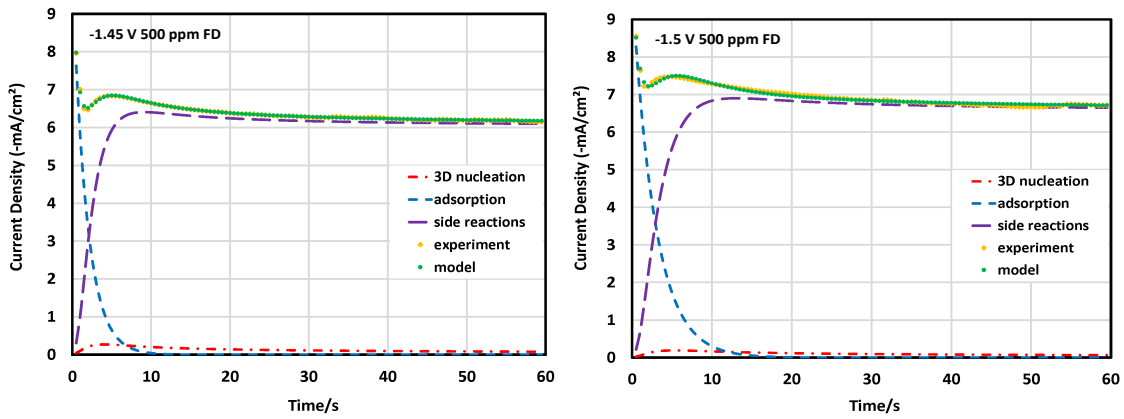

Figure S 3-2. shows the nucleation current transients at different potentials and FD concentrations together with the three deconvoluted contributions from capacitive charging, 3D nucleation, and side reaction. The currents from different contributions are well resolved for all the experimental curves where a peak is observed. It is evident from these results that the Co nucleation current gradually decays and the side reactions becomes more pronounced and dominates the overall deposition current as the potential becomes more negative or the FD concentration increases.

CHAPTER 4: OSCILLATORY BEHAVIOR IN COBALT ELECTRODEPOSITION WITH 3-MERCAPTO-1-PROPANESULFONATE

Published Work Disclosure: This chapter is based on previously published paper (Hu, Y.; Huang, Q., Oscillatory Behavior in Cobalt Electrodeposition with 3-Mercapto-1-Propanesulfonate. The Journal of Physical Chemistry C 2020.)

Summary

A potential oscillation was observed during galvanostatic deposition of Co in the presence of 3-mercapto-1-propanesulfonate (MPS) and a systematic study was conducted. A suppression effect on Co deposition by MPS was seen in cyclic voltammetry (CV) and such effect was not affected by pH. To fully understand the suppression effect and oscillation mechanism, several influencing factors in the galvanostatic process such as pH, Co^{2+} and MPS concentrations, agitation, and a buffer agent were thoroughly investigated. Moreover, mercaptopropionic acid, an alternative additive with a similar molecular structure as MPS, was used to determine the roles of thiol and sulfonate groups during the oscillation. Based on the experiment results, a kinetically controlled mechanism including a potential-dependent adsorption–desorption of the Co-MPS complex accompanied by the accumulation and dissolution of $Co(OH)_2$ was proposed.

Introduction

The damascene copper/low-k interconnect scheme has been used ubiquitously in semiconductor integrated circuits but are continuously facing difficulties in achieving defect-free Cu filling as the dimension of interconnect structure continues to decrease.[1] More importantly, the exponential increase of Cu resistivity as the dimension falls below the electron mean free path of Cu results in the greater RC delay,[2-3] jeopardizing the performance

gain earned from device innovations. Therefore, metals with shorter electron mean free path, such as cobalt (Co), have been explored as an alternative conductor. There are two main advantages in Co: (i) the relatively high melting point of Co is advantageous for electromigration; (ii) despite a higher bulk resistivity, Co shows a lower resistivity than Cu when the critical dimension of feature is approaching or smaller than Cu electron mean free path (about 38 nm).[4]

Organic additives are used in damascene Cu chemistries not only to achieve void-free metal filling process but also to control the impurity incorporation and grain structures of deposited Cu.[5-7] The former is achieved as a result of the interplay between multiple additive components.[8] The metal cation reduction kinetics are thus altered upon various mechanisms, such as an interaction between metal cations and additives in bulk electrolytes,[9] the adsorption, desorption, and breakdown of a catalytic or inhibitive intermediate species adsorbed on electrode surface,[10] or competitive adsorption between multiple intermediates on electrode surface.[11-12] These mechanisms at certain conditions can trigger electrochemical oscillation, where either the potential or current changes periodically within certain range during galvanostatic or potentiostatic deposition, respectively. Electrochemical oscillation phenomena in general have been reported in various systems,[13-17] where an autocatalytic reaction leads to a positive feedback loop. They can be classified based on the role of double layer potential, whether it is a non-essential component in a purely chemical autocatalytic loop, or is a slow changing factor with its effect gradually accumulating and eventually triggering an abrupt change of the direction of the autocatalytic reaction, or even forms the autocatalytic loop itself.[18]

Among damascene Cu chemistries, oscillation processes have also been reported. For most additive-containing cases, oscillation has been attributed to polarization curves that contain a region of negative differential resistance (NDR), where the current decreases with

increasing driving force.[14, 19-20] The extremely rapid (autocatalytic) self-breakdown kinetics of a suppressor-accelerator complex molecule conjugated through a cuprous ion, together with the slow kinetics of the formation and accumulation of such a complex on electrode surface, constructs the key elements of the oscillation. This chemical oscillation on the electrode surface was manifested through the electrochemical deposition of copper, where the different surface adsorbates change the reduction kinetics of copper resulting in electrochemical oscillation. However, NDR is not a requirement for Cu oscillation in additives-containing chemistries. For example, Cu oscillation occurred upon the addition of benzyl viologen and bis (3-sulfopropyl)disulfide (SPS), where NDR was not observed in the CV curves.[21] Studies using rotating ring-disk electrode suggested that the oscillation process is related to the potential dependent adsorption and desorption of two different additives, while such process can also be mediated by cuprous ions as other studies suggest. In addition, Cu oscillation process was also reported in simple electrolyte with complexing carboxyl acid, such as lactate and tartrate, where nanoscale multilayers or mixture between Cu and Cu_2O can be formed.[15, 22-23]

Although Cu oscillation has been well studied, oscillation during Co electrodeposition with additives has not been reported. The only oscillatory Co deposition, to the best of our knowledge, was reported during dendrite growth within a nanometric thin layer of additive-free electrolyte.[24] The mass transport in the confined configuration was confined as 2-dimensional diffusion, which limits the supply of Co cation and results in potential variation during galvanostatic deposition in that report. In this paper, potential oscillation is reported for Co electrodeposition in an electrolyte containing 3-mercapto-1-propanesulfonate, or MPS, the monomer version of the commonly used dimer accelerator, SPS. MPS is of interest to Co deposition as its adsorption and incorporation enable the tuning of impurity and control of grain structure of electrodeposited Co. The effects of critical parameters including pH, Co^{2+}

and MPS concentrations, as well as agitation, on the oscillation are systematically investigated here. Mercaptopropionic acid (MPA), a carboxyl acid with similar molecular structure as MPS, is used to dissect the roles the thiol and sulfonate groups play. A competitive adsorption mechanism is proposed to explain the observations.

Methods

A traditional three-compartment electrochemical cell was used for the experimental studies, where the catholyte and anolyte are separated by a glass frit. A saturated Ag/AgCl electrode (0.197 V vs. NHE) was used as the reference electrode, and all potentials were referred to this electrode in this paper. The reference electrode compartment is connected to the catholyte through a capillary. The counter electrode was a 99.96+% Co foil with a surface area much larger than the cathode. Platinum (Pt) rotating disk electrode (RDE) was used as cathode and the deposition area is 0.196 cm^2. Pt RDE is typically stripped and cleaned after use before storage. It was therefore used as is only after 1 M H_2SO_4 clean and DI water rinse.

The Co electrolyte at various concentrations of $CoSO_4$ were used in the studies. The solution pH was adjusted with H_2SO_4 and NaOH. Concentrated MPS solution (17800 ppm, or 0.1 M), concentrated mercaptopropionic acid (MPA) solution (10614 ppm, or 0.1 M), and boric acid (H_3BO_3, 0.4 M) were prepared by dissolving the corresponding chemicals in water. Calculated amounts of the concentrate were then added into the Co makeup solution up to various final concentrations. All salts and organic additives were at least ACS grade and used as received. Deionized (DI) water with a resistivity of 18.2 MOhm-cm was used in all studies. An Autolab 302N potentiostat with a frequency analyzer was used for all electrochemical studies. The impedance spectra were acquired using a 10 mV sinusoidal potential wave with frequency from 100 kHz to 100 mHz. An Apreo scanning electron microscope (SEM) was used to characterize the morphology of electrodeposited Co films.

Results & Discussion

Cyclic voltammetry

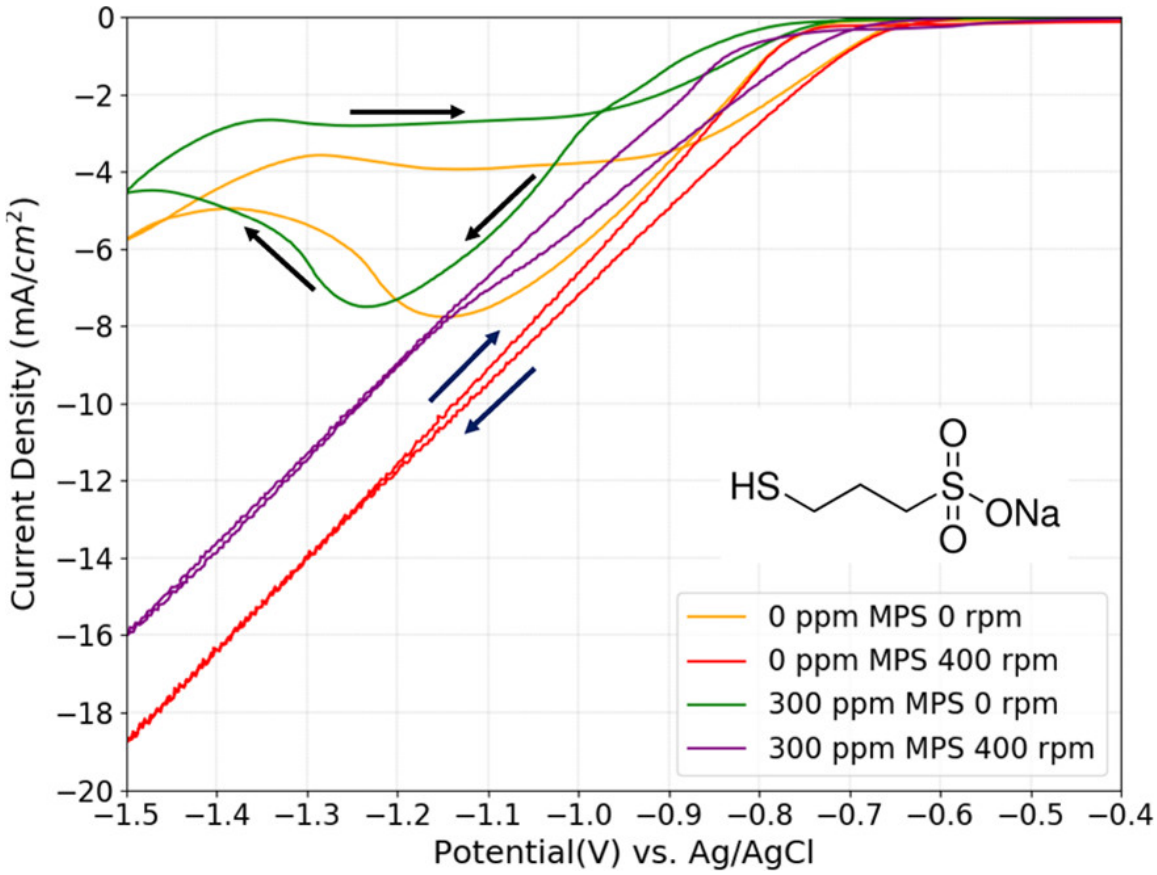

Figure 4-1. Cyclic voltammetry of Co electrodeposition on Pt RDE at different rotation rates in 0.05 M Co solutions with different MPS concentrations at pH = 4. Scan rate = 20 mV/s.

Figure 4-1 shows the cyclic voltammetry (CV) of Co electrodeposition on Pt electrode at two different rotation rates, where a suppression effect of MPS was observed. The electrolyte comprised 50 mM $CoSO_4$, scan rate was 20 mV/s and the pH was adjusted to 4. Co deposition started at around -0.70 V in absence of additive and rotation. As the potential reached more negative than -1.1 V, the depletion of Co^{2+} caused a decrease of the current density, a classic feature of stationary CV. Since the Pt electrode was not pre-plated with Co, Co deposition in the cathodic and anodic scans occurred on the Pt and Co surface, respectively, causing a crossover at -0.90 V on the reverse (anodic) sweep. Adding 300 ppm MPS into the electrolyte resulted in a suppression in Co deposition, where the magnitude of

current density was always lower than additive-free case in the kinetically controlled regime, i.e., the cathodic sweep before the peak. The crossover disappeared when a finite rotation rate, for example 400 rpm, was applied, as the mass transport was facilitated by the rotation and the diffusion limited current decay was eliminated. Similar suppression effect was also seen with MPS at 400 rpm, where a nearly constant potential shift was observed between the CVs with and without 300 ppm MPS. The study shown in Figure 4-1 was carried out at a pH of 4 and the same trend was also observed at other pH's studied, as shown in Figure S 4-1 in Supporting Information. It is worth noting here that MPS was added as a sodium salt and no pH change was observed upon this addition. Therefore, the above observations are attributed to MPS rather than any side effects of pH change. In addition, the ohmic resistance of the electrolytes were measured with impedance spectroscopy as shown in Figure S 4-2 in Supporting Information. The CVs were not corrected with the ohmic drop to allow easy comparison with the potential transient reading in galvanostatic deposition. However, the addition of MPS only slightly lower the ohmic resistance, therefore, the suppression effect characterized as the potential drift in CV is indeed slightly underestimated.

In our previous work, a class of dioxime molecules suppresses Co deposition through an adsorbed Co^{2+}-dioxime complex and this suppression breaks down as the cationic adsorbate is reduced and incorporated into Co film as impurities.[25-27] This suppression breakdown results in a hysteresis in CV curves, where the anodic sweep is of no difference from the additive free case as the adsorbate is being incorporated. However, the suppression effect of MPS observed here is different, where the magnitude of current density is always lower than additive-free case in cathodic and anodic sweeps. Complex structures between metal cations and MPS or other sulfur-bearing compounds are not uncommon in electrodeposition systems. For example, Hai et al.[19] proved the formation of H_2O-Cu(I)-MPS complex, where the addition of MPS into the Cu^{2+} solution led to a color change from blue to

yellow, which directly correlated with the formation of Cu(I)-MPS complex. Moreover, it was reported that thiol terminated molecules could bond to Co substrate to form a monolayer of the molecular.[28] In addition, secondary ion mass spectrometry (SIMS) analysis[29] showed that the addition of MPS caused a high incorporation of sulfur in the electrodeposited Co film and a lower content of nitrogen from dioxime. It is therefore believed that MPS could adsorb on the Co electrode surface and form Co-MPS complex adsorbate through the thiol group. This adsorbate not only blocks the electrode surface and moderately slows the charge transfer but also gets incorporated into the Co film as impurities. In addition, because no pH buffer agent is present in the electrolyte, the pH near electrode surface can rise significantly and $Co(OH)_2$ can be formed on electrode surface when the potential is highly negative, namely, when hydrogen evolution reaction (HER) reaches its mass transport limit or when water reduction reaction starts. While $Co(OH)_2$ adsorbate has indeed been proposed as an intermediate species in a two-step Co electrodeposition mechanism,[30] the formation of excessive hydroxide adsorbate at a high surface pH is expected to block electrode surface and completely prohibit metal deposition. It, therefore, is often avoided in film deposition. Nevertheless, either one of the two adsorbates, Co-MPS complex or $Co(OH)_2$, is believed to be sufficient for the kinetic suppression effect observed in the CVs.

Chronopotentiometry - Influence of Current

Figure 4-2 shows the potential transients during galvanostatic deposition of Co with the same electrolyte in Figure 4-1, with 50 mM $CoSO_4$ and pH of 4. The transients were acquired in a single experiment with multiple current steps. Three consecutive doses of 100 ppm MPS were added to the solution at 100, 200, and 300 s, respectively, as Co was deposited at -2.55 mA/cm^2 and 400 rpm. The addition of 300 ppm MPS caused a small decrease of the potential of about 100 mV, consistent with the suppression effect observed in CV studies. Further increasing current density to -4.08 mA/cm^2 led to an oscillation in

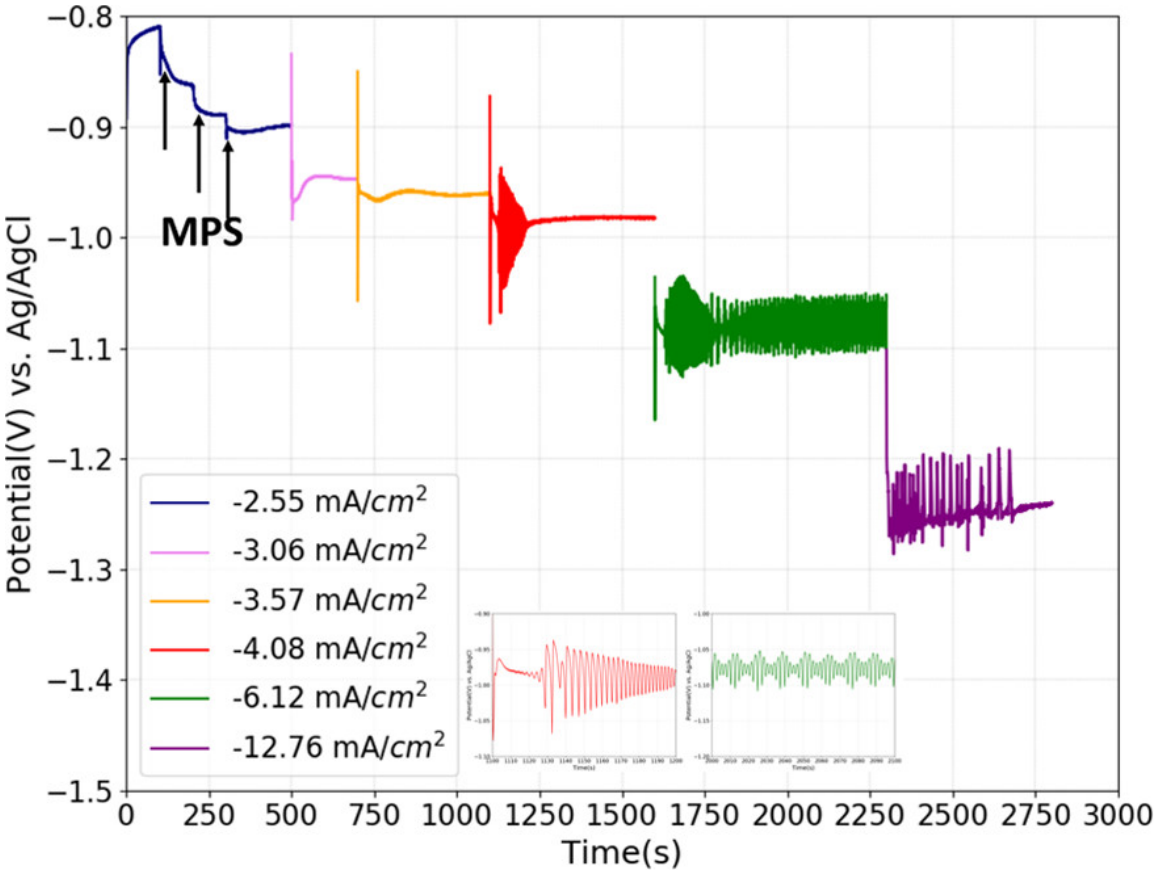

Figure 4-2. Potential transients for Co deposition at 400 rpm and different current densities in 0.05 M Co solutions with the addition of 300 ppm MPS at pH = 4. The detailed oscillation curves at -4.08 and -6.12 mA/cm^2 are shown in the inset.

potential. The detailed oscillation curves were included as the inset in the Figure 4-2. Upon the increase of current, the potential suddenly dropped to -1.08 V, followed by a rapid increase to -0.96 V. The potential oscillation gradually started afterwards and remained within a range from -0.95 to -1.05 V. The frequency of this potential oscillation was as high as 0.3 Hz or 3.33 s per cycle based on the observation from 1100 to 1200 s. However, this oscillation was unstable at this condition, where it started at around 1130 s with a continuously diminishing amplitude and eventually disappeared after about 100 seconds. A steady state potential of -0.99 V was obtained afterwards. A stable oscillation was observed when the current was further increased to -6.12 mA/cm^2. The average potential at this current density, about -1.07 V, was about 80 mV more negative than that at -4.08 mA/cm^2. On the other hand, electrochemical impedance analysis (Figure S 4-2 in Supporting Information)

showed that the ohmic resistance of electrolyte was about 180 Ω. An increase of current density from -4.08 to -6.12 mA/cm^2 on a 0.5 cm RDE translated to a potential shift of -72 mV. Therefore, the oscillations observed at these different current densities were believed to stem from the same electrochemical reactions at a same potential after the ohmic correction. Potential oscillation at a much higher current density of -12.76 mA/cm^2 seemed to be significantly inhibited, where the potential stayed at around -1.26 V for most of time with sporadic "spikes" at a less negative potential of -1.20 V.

Chronopotentiometry - Influence of pH

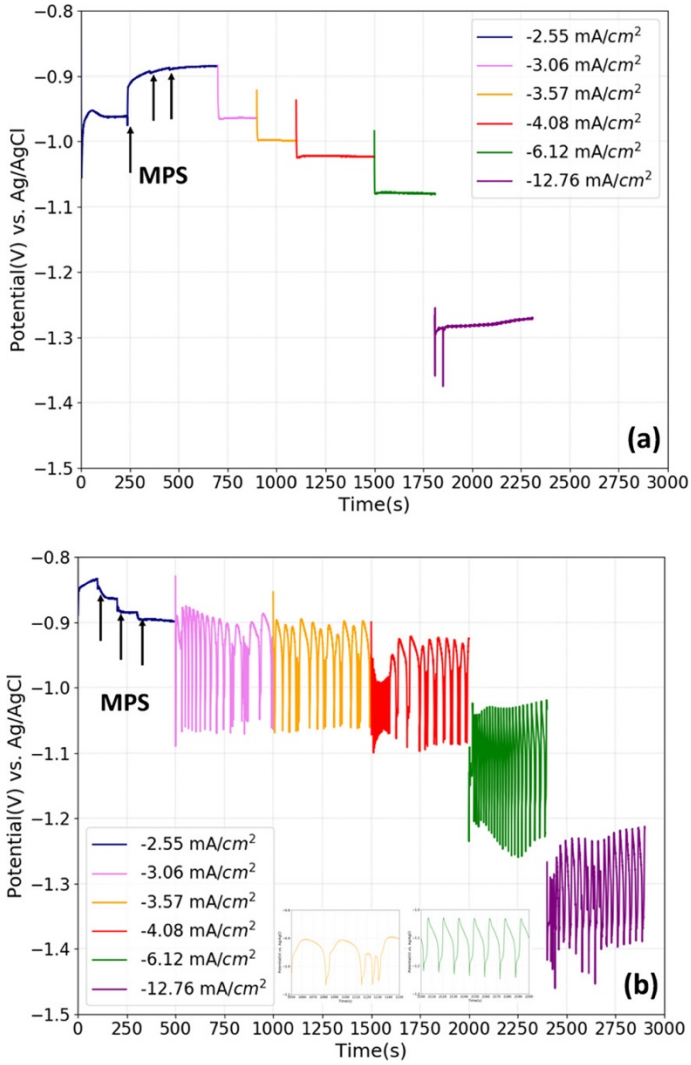

Figure 4-3. Potential transients for Co deposition at 400 rpm and different current densities in 0.05 M Co solutions with the addition of 300 ppm MPS at (a) pH = 3 and (b) pH = 5.67. The detailed oscillation curves at -3.57 and -6.12 mA/cm^2 are shown in the inset.

The influence of pH on Co deposition in presence of MPS was studied. Figure 4-3 (a) shows the potential transients during galvanostatic deposition of Co at a fixed rotation of 400 rpm in an electrolyte with 50 mM $CoSO_4$ and a pH of 3. Similar to the previous study, three doses of 100 ppm MPS were consecutively added into the Co solution at 250, 350, and 450 s with the current density kept at a constant of -2.55 mA/cm^2. Based on the pH measurement, the addition of 300 ppm MPS did not change the pH of Co^{2+} solution. The galvanostatic study showed that the addition of MPS caused depolarization at low current density, which was opposite to the suppression effect observed in CV study (Figure 4-1). It is possibly because the concertation of H^+ in electrolyte is much higher in this study, and the side reactions such as HER are expected to be more pronounced than Co deposition. Increasing current density to -4.08, -6.12, and -12.76 mA/cm^2 led to increasingly more negative potentials and typical steady state galvanostatic transients were seen for all the current densities studied.

Figure 4-3(b) shows the same galvanostatic study at a higher pH of 5.67. Same as the case with pH 4.0, the suppression effect on Co deposition with the addition of 300 ppm MPS was observed again at -2.55 mA/cm^2. The oscillation emerged at a current density of -3.06 mA/cm^2, much lower than -4.08 mA/cm^2 for a pH of 4. Despite of the different applied current densities, the lower bound (negative) potentials of oscillation were similar between the two cases, indicating that the mechanism of oscillation process is very likely potential dependent. Based on the magnified oscillation data shown as the inset from 1800 to 1900 s, the oscillation at the same -4.08 mA/cm^2 comprised two different modes, full oscillations between -0.9 and -1.1 V and partial oscillations between -1 and -1.1 V. The periods were about 50 s and 5 s for the full and partial oscillations, respectively. While such oscillations may seem to be slower than the acidic case (pH = 4 in Figure 4-2), the oscillations in the latter resembled the partial oscillation mode and were not stable, disappearing completely

after only 100 seconds. Moreover, the oscillations at pH 4 resemble the partial oscillation mode. The partial oscillations disappeared and only full oscillation with a period of 14.3 s were observed as the current density changed from -4.08 mA/cm^2 to -6.12 mA/cm^2. The morphology of a typical film obtained with oscillatory deposition was characterized with SEM and is presented in Figure S 4-3 in the Supporting Information. A film prepared without MPS or oscillation is included for comparison. Both two films showed a net style morphology or a flake-shaped deposit, however, at different scales. The films prepared with oscillation resulted in larger and probably deeper voids between the flakes. Dense films were obtained in both cases confirmed with cross-sectional characterization. No modulated layer structure was observed in a similar way in Cu, probably related to the fast oscillation.

The observation in Figure 4-2 and Figure 4-3 can be summarized as the following. i) The oscillation phenomenon is potential dependent and only occurs when the negative potential is below a threshold value. ii) This threshold potential is necessary but not sufficient for the oscillation and no oscillation can be enabled at a pH of 3 or below. iii) When an oscillation occurs, this threshold potential seems to be independent of pH. Although different current densities are needed at different pH's to enable the oscillation, the lower bound potential of the oscillations are similar. iv) The oscillation period is not only pH dependent but also current dependent. Partial oscillations are often observed at a lower pH or lower current density, with shorter periods or higher frequencies than the full oscillations, and accompanied by a lower upper bound potential. v) At a pH of 4 or above, a sharp drop followed by a rapid increase of potential was always observed immediately after the increase of current density.

As mentioned above, Co and MPS could form a complexed adsorbate on electrode surface. Based on the observations in Figure 4-3, we hypothesized that the adsorption and desorption of such complex is potential dependent, favored at less and more negative

potentials, respectively. Once a certain negative potential is reached, the desorption of Co-MPS complex accelerates and its surface coverage decreases, mitigating the suppression effect and resulting in a rise of potential in galvanostatic deposition. Meanwhile, as the potential becomes less negative, the side reactions like proton and water reduction reactions become less active, the pH at electrode surface decreases, the coverage of adsorbed $Co(OH)_2$ decreases, and the potential further increases. This forms a positive feedback loop for $Co(OH)_2$ desorption or dissolution triggered by the desorption of Co-MPS complex. In addition, the incorporation of Co-MPS complex into the deposit may form another positive feedback itself, as reported for many other systems.[9, 14]

Once the majority of Co-MPS complexes get incorporated into the deposit and most adsorbed $Co(OH)_2$ are dissolved, the potential reaches a maximum value, corresponding to the upper bound potential in the oscillation. However, Co-MPS complex in the solution will gradually adsorb and accumulate on the substrate surface, suppressing the deposition of Co and decreasing the potential at a constant current. More importantly, the latter facilitates the side reactions and increases the pH at electrode surface. Therefore, $Co(OH)_2$ starts to form in the vicinity of electrode surface, blocking the electrode surface. This, in the same way as above, results in a positive feedback loop of $Co(OH)_2$ adsorption triggered by the adsorption of Co-MPS complex. The potential gradually decreases in this loop until it reaches a minimum value, or the lower bound potential in the oscillation, which corresponds to a maximum coverage of Co-MPS complex and $Co(OH)_2$ on the electrode surface. The Co-MPS complex desorption starts at this point, triggering the positive feedback loops of $Co(OH)_2$ desorption and Co-MPS consumption and leading the next cycle of oscillation.

In this hypothesized mechanism, the formation/dissolution of the $Co(OH)_2$ adsorbate is a fast autocatalytic kinetics and the adsorption/desorption of MPS is a relative slow kinetics. The latter is highly potential dependent and serves as the trigger for the oscillation

and results in a threshold potential required for the oscillation. On the other hand, the former serves as the main positive feedback and a sufficiently high current density is necessary to drive the reaction rate to be faster than the rate the system equilibrates. When an intermediate current is used, damping oscillations that gradually disappear can occur, depending on the initial condition of the electrode surface. On the other hand, when the electrolyte pH is low, the system equilibrates faster, preventing the emerge of oscillation or resulting in partial oscillations. In addition, the potential range or the magnitude of oscillation highly depends on the surface adsorbate situation or the coverages of the two different adsorbates, which can also depend on the initial coverages and the rate of reaction, i.e., the applied current density.

The unstable oscillation in Figure 4-2 at -4.08 mA/cm^2 is believed to relate to an initial surface coverage off equilibrium. Oscillation emerged driven by the intermediate current and disappeared as the surface coverages readjusted themselves throughout the oscillation and reached a steady state situation. Again, this steady state was reached because the current was not high enough, allowing sufficient time for the adsorption/desorption of two competitive adsorbates to reach an equilibrium.

A close look at the stable oscillation at -6.12 mA/cm^2 in Figure 4-4(a) showed that a full oscillation cycle is not symmetrical but composed of several distinct segments. Each rise or drop segment of the potential transients comprises two stages, one slow change followed by a rapid change, consistent with the hypothesized Co-MPS and Co-OH kinetics, respectively. As shown in Figure 4-4(a), while the lower bound voltage varies significantly for each oscillation, the four distinct segments starts at much more consistent potentials. The former could result from a nonuniform over-formation and precipitation of $Co(OH)_2$ adsorbate, which however dissolves immediately at certain surface pH. The four distinct potentials suggest the surface coverage situation are repeatable for each oscillation. As shown in the diagrams in Figure 4-4(b), we here consider the upper bound potential represents clean

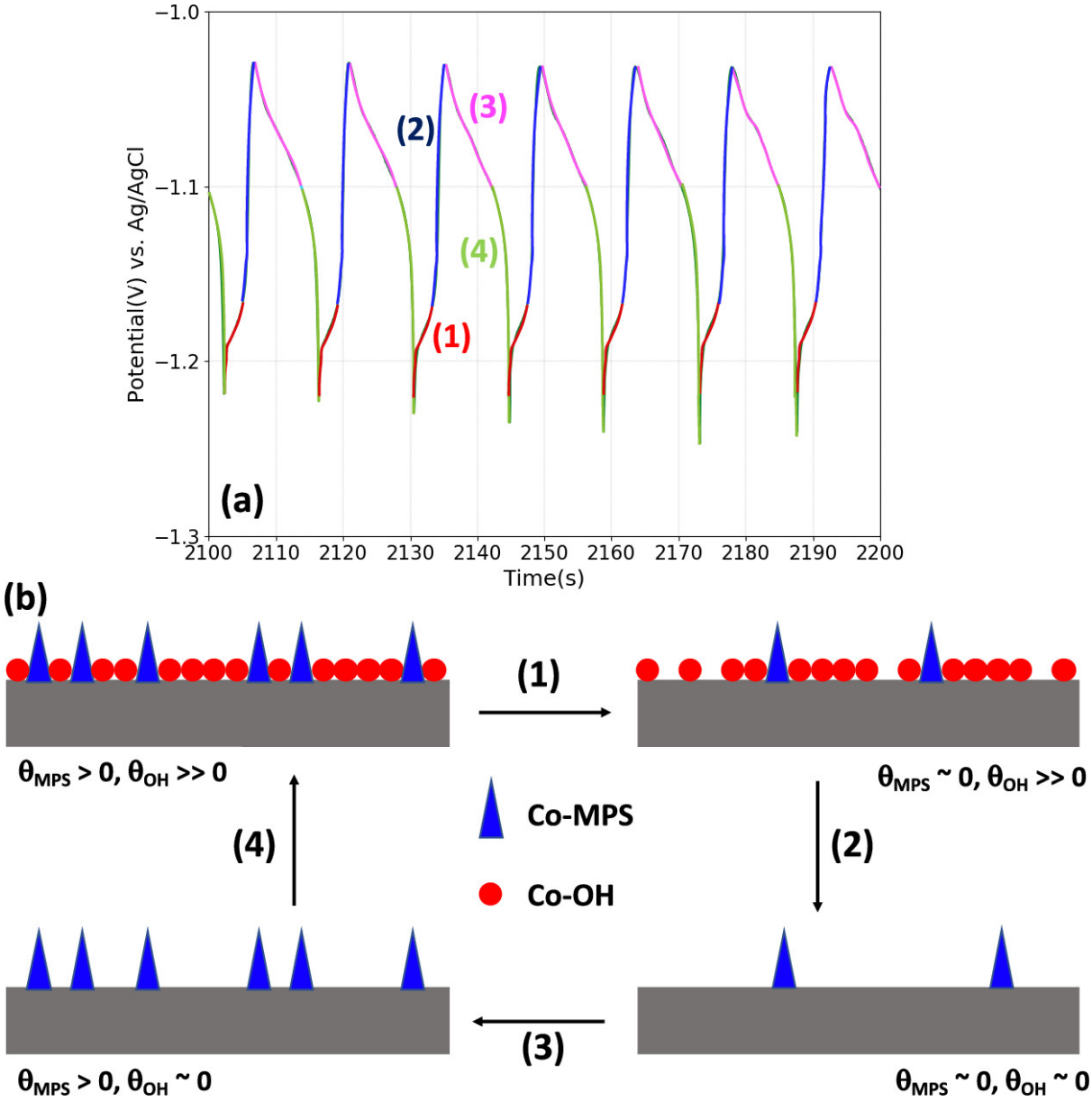

Figure 4-4. (a) Close look of the potential oscillation at 400 rpm and -6.12 mA/cm^2 in 0.05 M Co solutions with 300 ppm MPS and pH = 5.67 and (b) diagram showing the four steps of (1) Co–MPS desorption, (2) $Co(OH)_x$ dissolution, (3) Co-MPS adsorption, and (4) $Co(OH)_x$ accumulation.

surface free of either adsorbate (or minimum coverage) and the lower bound corresponds a maximum coverage of mixture between Co-MPS and Co-OH. It is clear that the rapid formation and dissolution of Co-OH are triggered at about -1.10 V and -1.19 V, respectively, reflecting the different adsorbate coverages on the electrode. Furthermore, the rise of potential in a cycle is fast while the drop of potential takes longer time, due to a slower

adsorption and faster desorption of Co-MPS complex. We use the word "desorption" to refer to the decrease of Co-MPS coverage, but it indeed should include other breakdown mechanisms such as reduction, consumption, or incorporation.

When the applied current decreases, the rate of side reaction, such as the reduction of proton and water, decreases. Therefore, the formation and adsorption of $Co(OH)_2$ will be slowed, decreasing the oscillation frequency. On the other hand, at a higher current density, the surface concentration of $Co(OH)_2$ is high due to the strong side reactions, which facilitates the adsorption of $Co(OH)_2$ process and decreases the oscillation period. This explanation is consistent with the experimental results in Figure 4-3(b), where the oscillation period decreases as the current density is changed from -4.08 mA/cm^2 to -6.12 mA/cm^2. It is noted here that we use the period of full oscillation because the partial cycles do not involve the complete breakdown of Co-OH and the adsorption of Co-MPS and the cycles are much faster and not stable.

Based on the hypothesized mechanism, the formation and breakdown of Co-MPS and Co-OH adsorbates on electrode surface underpin the oscillations. Therefore, studies are carried out to probe the effects of constituents of such complexes.

Influence of Co^{2+} and MPS Concentrations

Figure 4-5 shows the galvanostatic study of Co deposition with different concentrations of Co^{2+} and MPS. Figure 4-5(a) shows the Co deposition in an electrolyte similar to Figure 4-3(b), with 300 ppm MPS and a natural pH of 5.75, but a higher Co^{2+} concentration of 0.1 M. Similar to the 0.05M Co^{2+} case, suppression effect was observed with the addition of MPS at -2.55 mA/cm^2. However, oscillation did not happen until the current density was increased to -6.12 mA/cm^2, much higher than -3.06 mA/cm^2 required in 0.05 M Co^{2+} case. In addition, the oscillation was unstable at -6.12 mA/cm^2 and stopped after around 1000 s. Stable oscillations for over 1000 s was achieved at a higher current density of -12.76

mA/cm^2. These observations are consistent with a lower effective current density of side reactions due to the increased concentration of metal ion, namely a lower driving current for the Co-OH positive feedback loop. The detailed oscillation curves are shown as the inset in Figure 4-5(a). The oscillations resemble the partial oscillation mode in observed at lower current densities in Figure 4-3(b), and this is also consistent with the lower effective driving current due to the higher concentration of Co^{2+}.

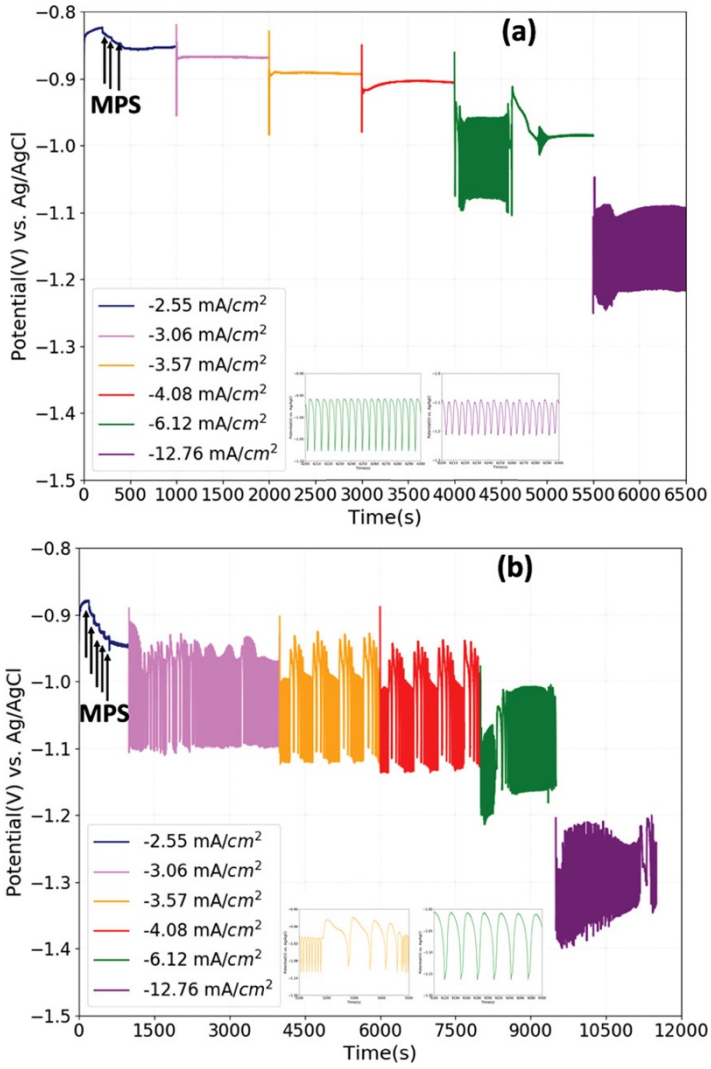

Figure 4-5. Potential transients for Co deposition at 400 rpm and different current densities in (a) 0.1 M Co solutions with the addition of 300 ppm MPS at measured pH = 5.75 and (b) 0.05 M Co solutions with the addition of 500 ppm MPS at pH = 5.67. The detailed oscillation curves are shown in the inset.

The effect of MPS concentration was studied with an electrolyte similar to Figure 4-3(b), with 0.05 M Co^{2+} and a pH of 5.67, but a higher MPS concentration of 500 ppm. The

potential transients are shown in Figure 4-5(b). Oscillations with partial mode started at -3.06 mA/cm^2, similar to the 300 ppm MPS case. The transformation from partial oscillation to full oscillation started at -3.57 mA/cm^2. Stable oscillation was achieved at -6.12 mA/cm^2. Comparison between Figure 4 and the inset in Figure 4-5(b) at a same current density of -6.12 mA/cm^2 clearly shows that the Co-MPS adsorption segment is much less distinctive at higher MPS concentration. This is consistent with the expectation that higher MPS concentration facilitates the adsorption of Co-MPS during the dissolution/desorption of $Co(OH)_2$, disabling a completely adsorbate free surface to be achieved, or resulting in a higher minimum surface coverage.

Influence of Rotation

Another way of probing the electrode kinetics is to change the agitation, namely, the supply rate of chemical species toward the electrode. Figure 4-6 shows the oscillatory transients with the disk electrode at various rotation rates. The studies were also carried out in an electrolyte same as Figure 4-3(b), i.e., with 50 mM Co^{2+}, 300 ppm MPS, and a pH of 5.67. A fixed current density of -6.12 mA/cm^2 was used. These conditions were used because stable oscillations could be achieved at 400 rpm. Different rotation rates from 0 to 1600 rpm were used over a course of 7000 s deposition, and each rotation rate was maintained for enough time till stable oscillations were observed. The stable oscillations for each rotation rate were cropped together and is shown in Figure 4-6. Stable oscillations with four distinct segments were observed for all rotation rates beyond 0 rpm. The potential range of oscillation seemed to be similar until the rotation rates were below 100 rpm, consistent with the constant current used and the hypothesized mechanism. The lower boundary of the oscillation varied and was consistently more negative at low rotation rates. This is believed to be consistent with the hypothesized mechanism, where the formation and precipitation of Co-OH is

expected to be less controlled and more likely to run over the equilibrium at low rotation rates, leading to a more negative potential overshoot.

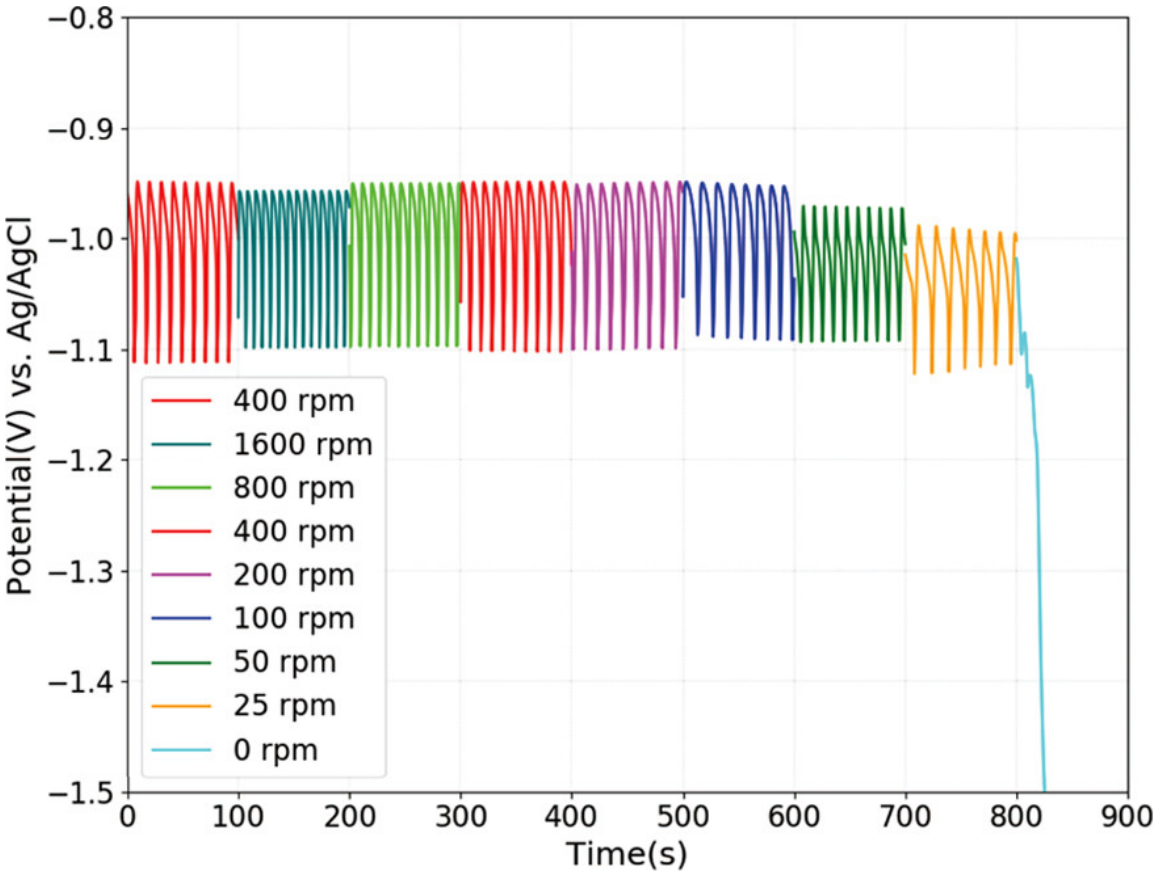

Figure 4-6. Potential transients for Co deposition at different rotation rates in 0.05 M Co solutions with the addition of 300 ppm MPS at pH = 5.67. The applied current density is -6.12 mA/cm^2.

The average period for the stable oscillations at different rotation rates were obtained by counting the total time of 10 oscillations and are summarized in Table I. The rotation rate of 400 rpm was used multiple times during the experiment as an experimental control and the period was found reproducible and independent of the experimental sequence or electrode history. In general, the stable oscillations seemed to be slightly faster at a higher rotation rate, with the period dropped from 14 s at 25 rpm to 7 s at 1600 rpm. While this correlation suggests that mass transport plays a role in the oscillation process, the effect is not strong. The period merely decreased into half with the rotation rates increased by 64 times. It is interesting to find that the main reason for the increase of period was due to the slowdown of

Table 4-1. The oscillatory periods at different rotation rates obtained from the potential transients shown in **Figure 4-6**.

Rotation Rate (rpm)	Cycles per 100 seconds	Oscillation Period (s/cycle)
400	10	10.0
1600	14	7.1
800	11	9.1
400	10	10.0
200	9	11.1
100	8	12.5
50	10	10.0
25	7	14.3
0	0	Infinity (no oscillation)

the slow kinetic segments while the fast kinetics or the sharp potential change remained sharp. This is consistent with the hypothesized mechanism as well, where the sharp change is hypothesized to result from a positive feedback of Co-OH formation and dissolution. This process highly relies on the surface pH change, which is expected to be more pronounced as rotation decreases. That is, this rapid positive feedback is not expected to be mitigated at low rotation rates. On the other hand, the slow kinetics, which is hypothesized to be the adsorption and desorption of Co-MPS complex, is expected to be related to the surface concentration of such complex and, therefore, the rotation rates. As the rotation rate decreases, the supply of Co-MPS to electrode or the dilution from electrode surface slows down, resulting in a slower adsorption or desorption. However, when the agitation is completely stopped, the surface concentrations of all species can be drastically different from bulk electrolyte. As the metal ion is depleted, side reactions dominate, surface pH increases

indefinitely, the surface is completely blocked by Co-OH complex. The potential decreases to extremely negative values to enable water reduction on this completely blocked electrode, and, of course, oscillation completely ceases.

The influence of H_3BO_3

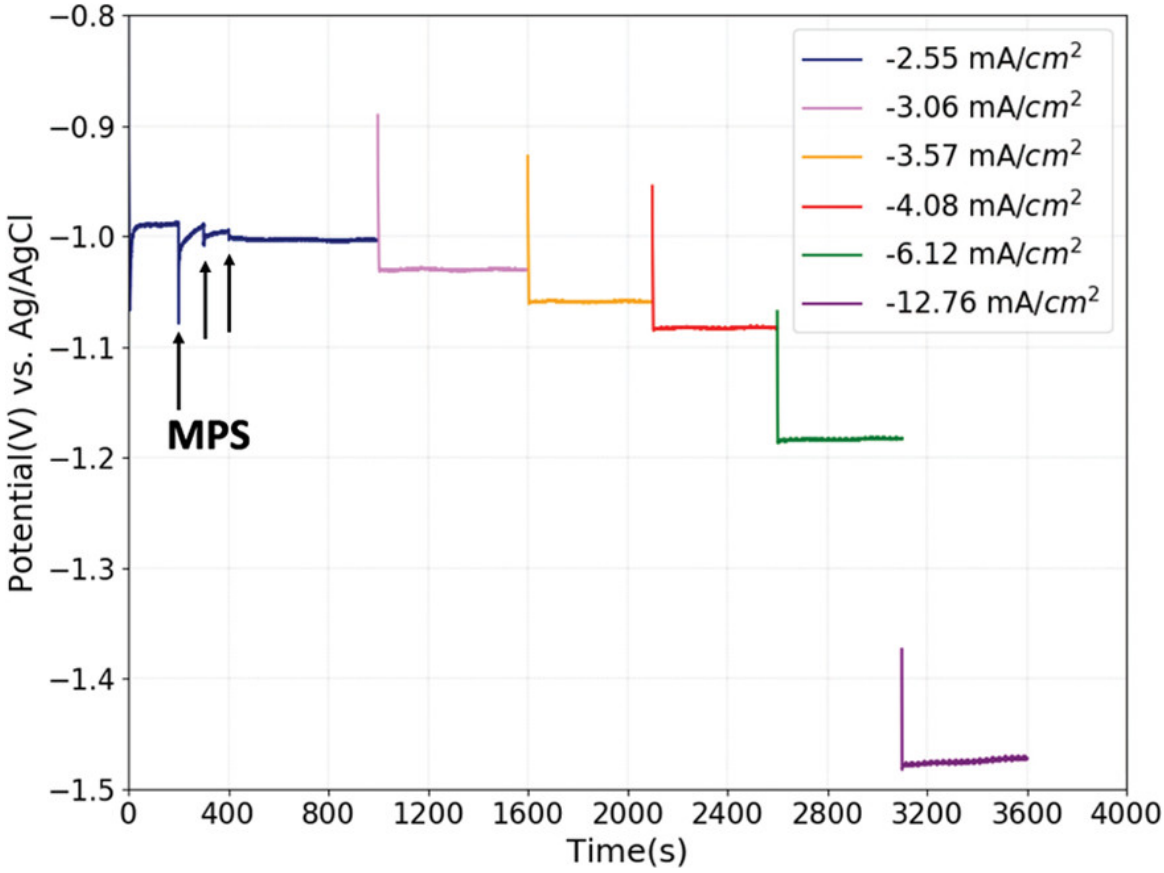

Figure 4-7. Potential transients for Co deposition at 400 rpm and different current densities in 0.05 M Co solutions with the addition of 300 ppm MPS and 0.4 M H_3BO_3 at measured pH = 4.3.

In order to further test the role of surface pH in oscillation, we conducted another study on the effect of a pH buffer, H_3BO_3. An electrolyte similar to Figure 4-3(b), with 0.05 M Co^{2+} and 300 ppm MPS, was used. But the pH was changed from 5.67 to 4.3 upon the addition of 0.4 M H_3BO_3. As discussed in Figures 4-2 and 4-3, electrolytes without boric acid at pH of 4 and 5.67 both showed oscillation, albeit starting at different current densities. Therefore, this different bulk pH of 4.3 was not expect to cause significant change in oscillation. The potential transients at different current densities in this buffered electrolyte are presented in Figure 4-7. Not only were oscillations not observed regardless of the current

densities, but also less negative overall deposition potentials were resulted. Such observations are similar to the pH = 3 case in Figure 4-3(a). Boric acid is a pH buffer with a pKa of 9.24, commonly used in iron-group magnetic alloy electrodeposition to prevent extremely high pH and hydroxide incorporation in the films.[31] The absence of oscillation here further confirms that a high surface pH and the formation of $Co(OH)_2$ plays an important role in the oscillation.

The Influence of Mercaptopropionic Acid

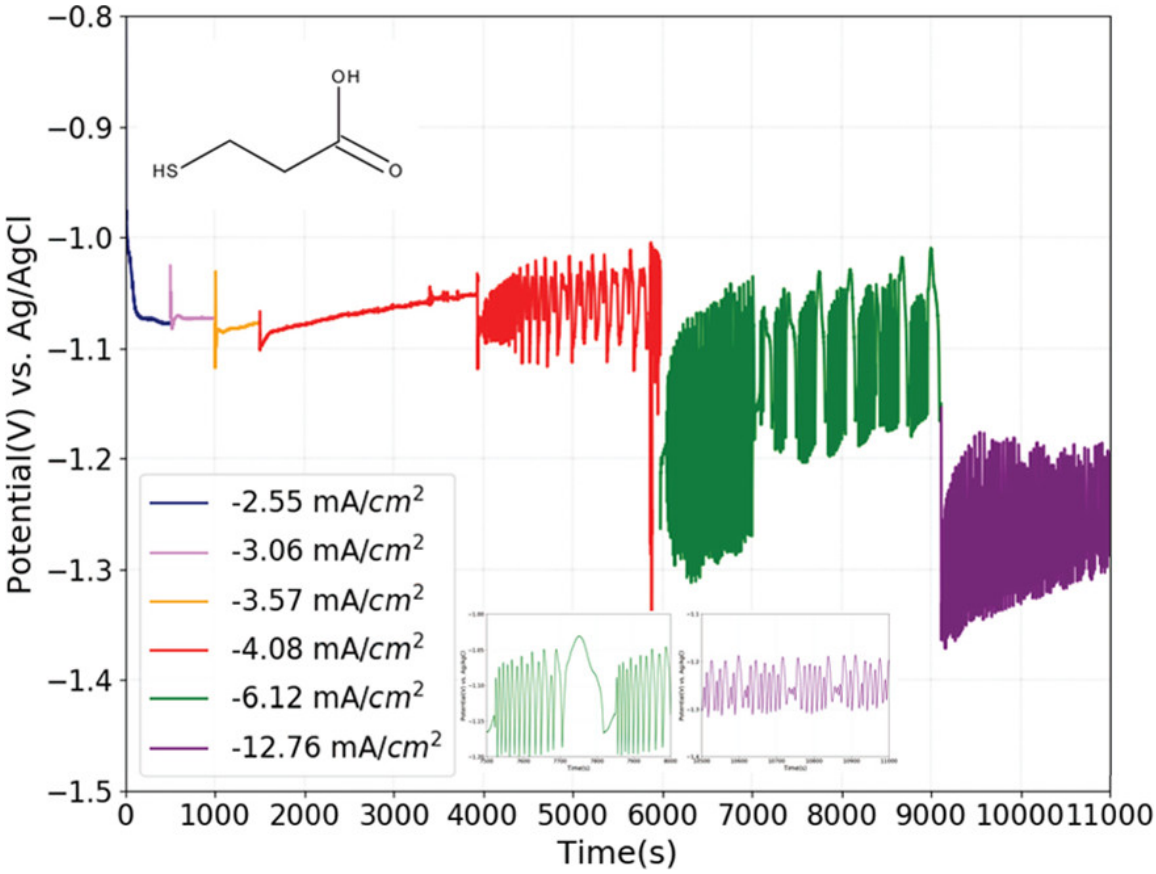

Figure 4-8. Potential transients for Co deposition at different current densities in 0.05 M Co solutions with the addition of 300 ppm MPA at adjusted pH = 5.67.

To further understand the structure of Co^{2+}-MPS complex, mercaptopropionic acid, or MPA, an acid with a similar structure as MPS, was used in place of MPS. The only structural difference between the two is that MPS contains the sulfonate group and MPA contains the carboxyl group. Figure 4-8 shows the potential transients with the addition of 300 ppm MPA in 0.05 M Co^{2+} electrolyte. While the addition of 300 ppm MPA significantly decreased the

solution pH from 5.67 to around 3.76, pH was re-adjusted back to 5.67 prior to the galvanostatic deposition study. The pKa of the carboxyl group is 4.6,[32] and no buffering is expected from this carboxyl group in this electrolyte with the pH of 5.67. The oscillation was observed at -4.08 mA/cm^2, but only after the current was applied for nearly 2500 s. As shown in the inset, the oscillation was not stable and partial oscillations were also observed, where the lower bound potential or the maximum surface coverage by Co-OH was not fully reached. Further increasing the current density did not lead to stable oscillation. Since the formation of complex is important for the oscillation behavior, this experiment result confirms that Co will interact with thiol group to form the Co-MPS or Co-MPA complex on the electrode surface. The CVs of MPA are provided in Figure S 4-4 in Supporting Information, where a stronger suppression effect was observed for MPA than MPS. This is also consistent with the fact that MPA has additional carboxyl group which, in conjunction with the thiol group, prefer to chelate with the bivalent Co^{2+} to form a more stable complex Co-$(MPA)_2$ with a stability constant around 13.[32] This stronger suppressive adsorbate apparently not only drives the deposition potential to a more negative range but also alters the competitive surface coverage and the oscillation behavior.

Conclusion

A potential oscillation was observed during galvanostatic deposition of Co in the presence of MPS, which mildly suppressed the deposition. The fast autocatalytic kinetics of the accumulation and dissolution of $Co(OH)_2$ were proposed as the main positive feedback loops for this oscillation, which were respectively triggered by the slow but potential dependent adsorption and desorption of Co-MPS complex. This mechanism was verified by a systematic study on the effects of parameters including bulk pH, Co^{2+} and MPS concentration, rotation rate, as well as pH buffer. In addition, oscillation was also observed

when an alternative additive, MPA, was used, confirming the formation of Co-MPS complex through the thiol group and the critical role such complex played in the oscillation.

Acknowledgements

National Science Foundation is acknowledged for support through Grant CMMI-1662332. YH thanks the Graduate Council at University of Alabama for a fellowship support. Central analytical facility at the University of Alabama is acknowledged for the access of equipment for characterization.

References

1. Steinhögl, W.; Schindler, G.; Steinlesberger, G.; Engelhardt, M., Size-dependent resistivity of metallic wires in the mesoscopic range. *Physical Review B* **2002,** *66* (7), 075414.

2. He, M.; Zhang, X.; Nogami, T.; Lin, X.; Kelly, J.; Kim, H.; Spooner, T.; Edelstein, D.; Zhao, L., Mechanism of Co liner as enhancement layer for Cu interconnect gap-fill. *J. Electrochem. Soc.* **2013,** *160* (12), D3040-D3044.

3. Wu, W.; Brongersma, S.; Van Hove, M.; Maex, K., Influence of surface and grain-boundary scattering on the resistivity of copper in reduced dimensions. *Appl. Phys. Lett.* **2004,** *84* (15), 2838-2840.

4. Gall, D., Electron mean free path in elemental metals. *J. Appl. Phys.* **2016,** *119* (8), 085101.

5. Moffat, T.; Wheeler, D.; Huber, W.; Josell, D., Superconformal electrodeposition of copper. *Electrochem. Solid-State Lett.* **2001,** *4* (4), C26-C29.

6. Huang, Q.; Avekians, A.; Ahmed, S.; Parks, C.; Baker-O'Neal, B.; Kitayaporn, S.; Sahin, A.; Sun, Y.; Cheng, T., Impurities in the electroplated sub-50 nm Cu lines: The effects of the plating additives. *J. Electrochem. Soc.* **2014,** *161* (9), D388-D394.

7. Kelly, J.; Nogami, T.; Van der Straten, O.; Demarest, J.; Li, J.; Penny, C.; Vo, T.; Parks, C.; DeHaven, P.; Hu, C.-K., Electrolyte additive chemistry and feature size-dependent impurity incorporation for Cu interconnects. *J. Electrochem. Soc.* **2012,** *159* (10), D563-D569.

8. Moffat, T. P.; Wheeler, D.; Kim, S.-K.; Josell, D., Curvature enhanced adsorbate coverage model for electrodeposition. *J. Electrochem. Soc.* **2006,** *153* (2), C127-C132.

9. Hai, N.; Furrer, J.; Gjuroski, I.; Bircher, M.; Cascella, M.; Broekmann, P., On the Acceleration of Cu Electrodeposition by TBPS (3, 3-thiobis-1-propanesulfonic acid): A Combined Electrochemical, STM, NMR, ESI-MS and DFT Study. *J. Electrochem. Soc.* **2013,** *160* (12), D3158.

10. Chiu, Y.-D.; Dow, W.-P.; Krug, K.; Liu, Y.-F.; Lee, Y.-L.; Yau, S.-L., Adsorption and desorption of Bis-(3-sulfopropyl) disulfide during Cu electrodeposition and stripping at Au electrodes. *Langmuir* **2012,** *28* (40), 14476-14487.

11. Walker, M. L.; Richter, L. J.; Moffat, T. P., Competitive adsorption of PEG, Cl−, and SPS/MPS on Cu: an in situ ellipsometric study. *J. Electrochem. Soc.* **2006,** *153* (8), C557-C561.

12. Moffat, T. P.; Wheeler, D.; Josell, D., Electrodeposition of copper in the SPS-PEG-Cl additive system I. Kinetic measurements: Influence of SPS. *J. Electrochem. Soc.* **2004,** *151* (4), C262-C271.

13. Orban, M.; Epstein, I. R., Oscillations and bistability in hydrogen-platinum-oxyhalogen systems. *JACS* **1981,** *103* (13), 3723-3727.

14. Hai, N. T.; Odermatt, J.; Grimaudo, V.; Krämer, K. W.; Fluegel, A.; Arnold, M.; Mayer, D.; Broekmann, P., Potential oscillations in galvanostatic Cu electrodeposition: antagonistic and synergistic effects among SPS, chloride, and suppressor additives. *The Journal of Physical Chemistry C* **2012,** *116* (12), 6913-6924.

15. Bohannan, E. W.; Huang, L.-Y.; Miller, F. S.; Shumsky, M. G.; Switzer, J. A., In situ electrochemical quartz crystal microbalance study of potential oscillations during the electrodeposition of Cu/Cu2O layered nanostructures. *Langmuir* **1999,** *15* (3), 813-818.

16. Strasser, P.; Eiswirth, M.; Ertl, G., Oscillatory instabilities during formic acid oxidation on Pt (100), Pt (110) and Pt (111) under potentiostatic control. II. Model calculations. *The Journal of chemical physics* **1997,** *107* (3), 991-1003.

17. Strasser, P.; Lübke, M.; Raspel, F.; Eiswirth, M.; Ertl, G., Oscillatory instabilities during formic acid oxidation on Pt (100), Pt (110) and Pt (111) under potentiostatic control. I. Experimental. *The Journal of chemical physics* **1997,** *107* (3), 979-990.

18. Strasser, P.; Eiswirth, M.; Koper, M. T., Mechanistic classification of electrochemical oscillators—an operational experimental strategy. *J. Electroanal. Chem.* **1999,** *478* (1-2), 50-66.

19. Hai, N. T.; Krämer, K. W.; Fluegel, A.; Arnold, M.; Mayer, D.; Broekmann, P., Beyond interfacial anion/cation pairing: The role of Cu (I) coordination chemistry in additive-controlled copper plating. *Electrochim. Acta* **2012,** *83*, 367-375.

20. Hai, N.; Furrer, J.; Barletta, E.; Lüdi, N.; Broekmann, P., Copolymers of imidazole and 1, 4-butandiol diglycidyl ether as an efficient suppressor additive for copper electroplating. *J. Electrochem. Soc.* **2014,** *161* (9), D381-D387.

21. Barkey, D.; Chang, R.; Liu, D.; Chen, J., Observation of a limit cycle in potential oscillations during copper electrodeposition in a leveler/accelerant system. *J. Electrochem. Soc.* **2014,** *161* (3), D97-D101.

22. Switzer, J. A.; Hung, C.-J.; Huang, L.-Y.; Miller, F. S.; Zhou, Y.; Raub, E. R.; Shumsky, M. G.; Bohannan, E. W., Potential oscillations during the electrochemical self-assembly of copper/cuprous oxide layered nanostructures. *J. Mater. Res.* **1998,** *13* (4), 909-916.

23. Leopold, S.; Herranen, M.; Carlsson, J.-O., Spontaneous potential oscillations in the Cu (II)/tartrate and lactate systems, aspects of mechanisms and film deposition. *J. Electrochem. Soc.* **2001,** *148* (8), C513-C517.

24. Huang, X.-P.; Han, W.; Shi, Z.-L.; Wu, D.; Wang, M.; Peng, R.-W.; Ming, N.-B., Electrodeposition of periodically nanostructured straight cobalt filament arrays. *The Journal of Physical Chemistry C* **2009,** *113* (5), 1694-1697.

25. Huang, Q.; Lyons, T.; Sides, W., Electrodeposition of Cobalt for Interconnect Application: Effect of Dimethylglyoxime. *J. Electrochem. Soc.* **2016,** *163* (13), D715-D721.

26. Lyons, T.; Huang, Q., Effects of Cyclohexane-Monoxime and Dioxime on the Electrodeposition of Cobalt. *Electrochim. Acta* **2017,** *245*, 309-317.

27. Hu, Y.; Huang, Q., Effects of Dimethylglyoxime and Cyclohexane Dioxime on the Electrochemical Nucleation and Growth of Cobalt. *J. Electrochem. Soc.* **2019,** *166* (1), D3175-D3181.

28. Caruso, A.; Wang, L.; Jaswal, S.; Tsymbal, E. Y.; Dowben, P. A., The interface electronic structure of thiol terminated molecules on cobalt and gold surfaces. *Journal of materials science* **2006,** *41* (19), 6198-6206.

29. Hu, Y.; Huang, Q. In *Thermal Annealing and Impurities Incorporation of Electrodeposited Cobalt Thin Film*, Meeting Abstracts, The Electrochemical Society: 2019; pp 1256-1256.

30. Santos, J.; Trivinho-Strixino, F.; Pereira, E., Investigation of Co (OH) 2 formation during cobalt electrodeposition using a chemometric procedure. *Surf. Coat. Technol.* **2010,** *205* (7), 2585-2589.

31. Andricacos, P.; Arana, C.; Tabib, J.; Dukovic, J.; Romankiw, L., Electrodeposition of Nickel-Iron Alloys: I. Effect of Agitation. *J. Electrochem. Soc.* **1989,** *136* (5), 1336.

32. Martell, A. E.; Smith, R. M., *Critical stability constants*. Springer: 1974; Vol. 1.

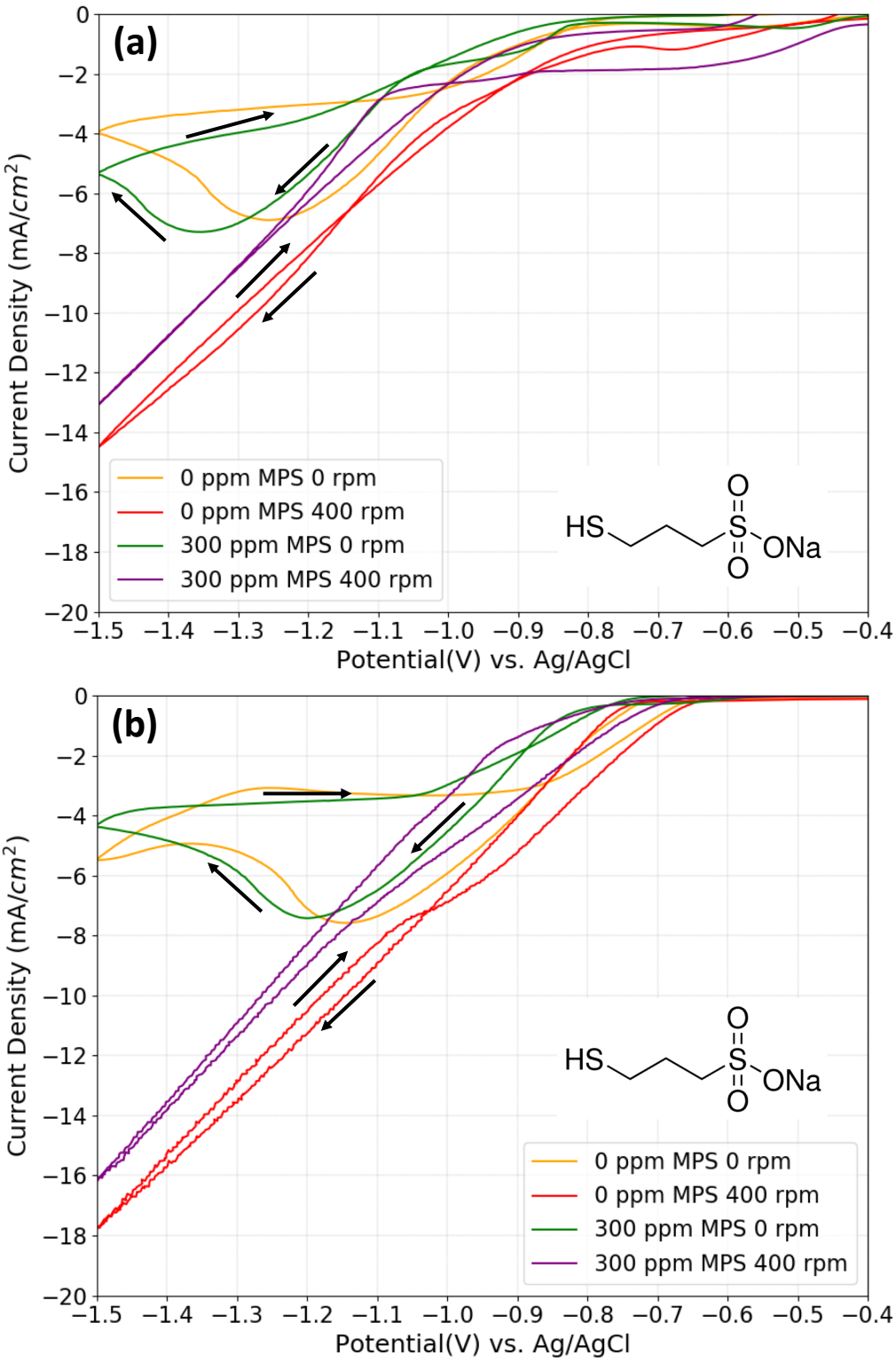

Figure S 4-1. Cyclic voltammetry of Co electrodeposition on Pt RDE at different rotation rates in 0.05 M Co solutions with different MPS concentrations at (a) pH = 3, (b) pH = 5.67. Scan rate = 20 mV/s.

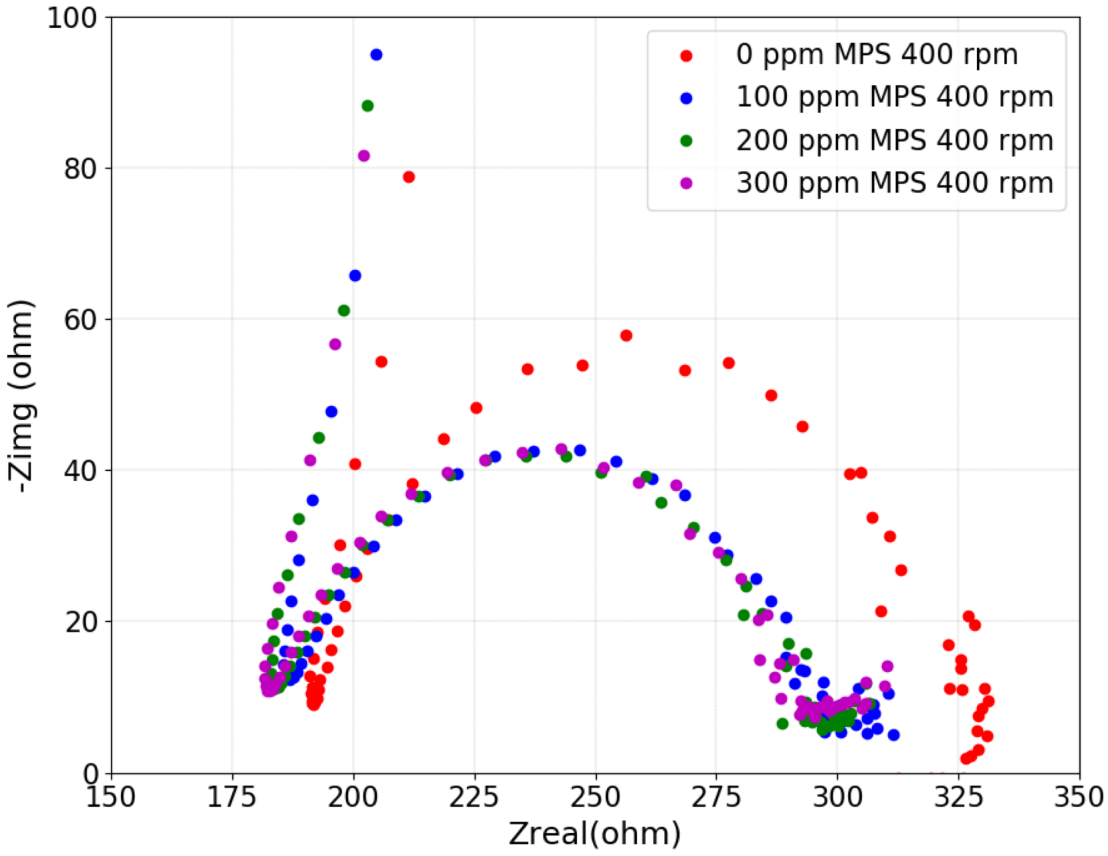

Figure S 4-2. Electrochemical impedance spectra of Co deposition in 0.05 M Co solutions with different MPS concentrations at pH = 3. The rotation rate was 400 rpm and the applied current density was -2.55 mA/cm^2. The resistance of solution was high and similar regardless of the addition of MPS.

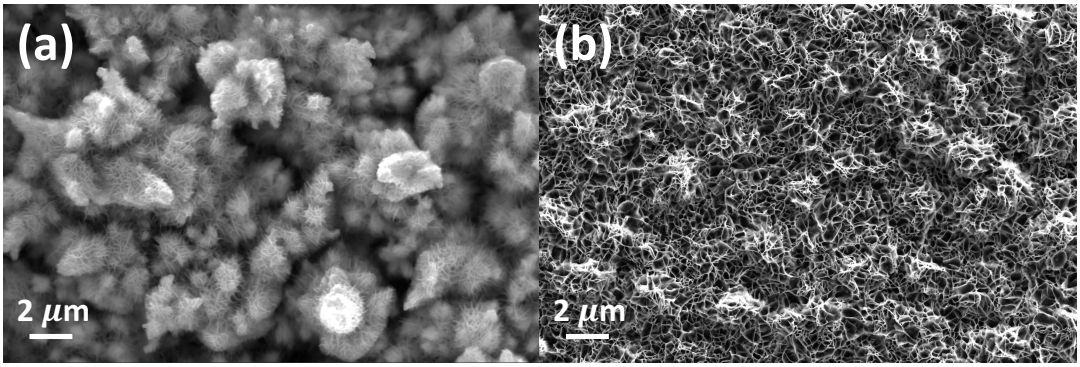

Figure S 4-3. Top down SEM micrographs of the surface morphology of cobalt films deposited at -5.10 mA/cm^2 and 400 rpm in 0.05M Co electrolyte at pH=5.67 with (a) 0 ppm MPS with no oscillation observed, and (b) 300 ppm MPS, where oscillation was observed.

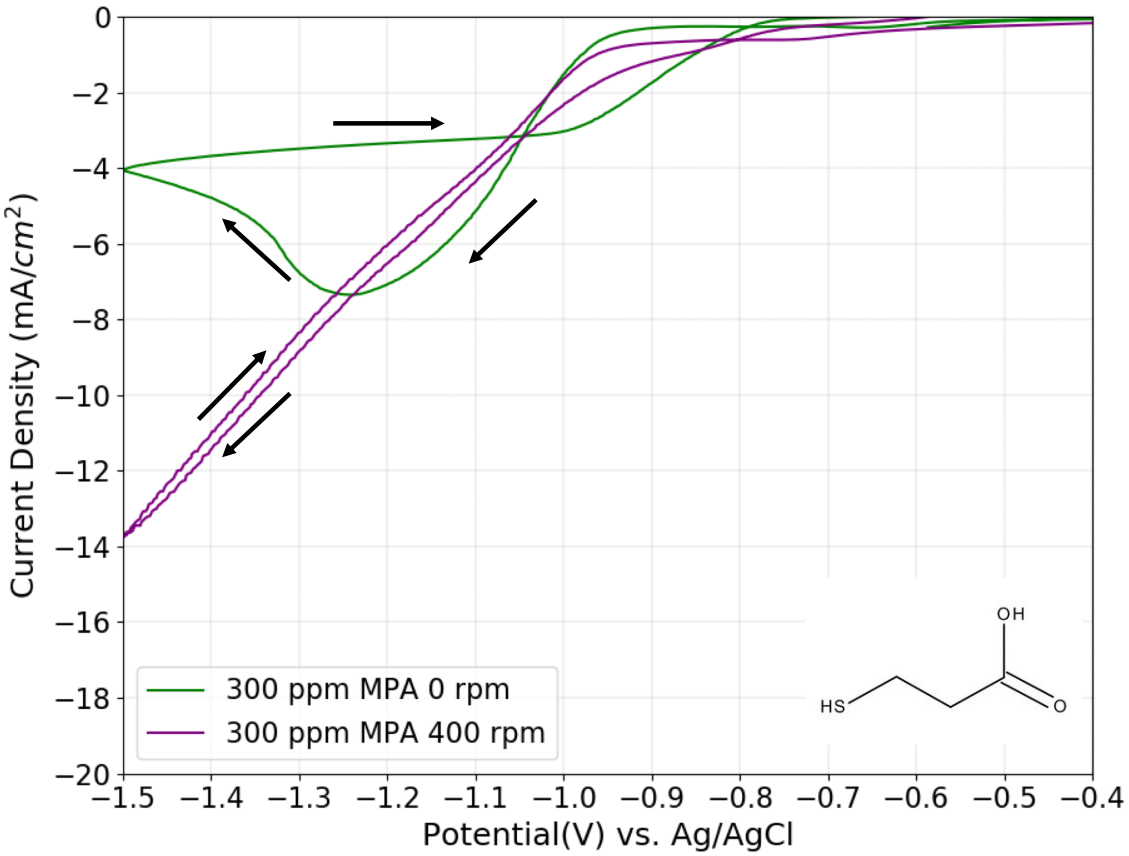

Figure S 4-4. Cyclic voltammetry of Co electrodeposition on Pt RDE at different rotation rates in 0.05 M Co solutions with 300 ppm MPA concentrations at adjusted pH = 5.67. Scan rate = 20 mV/s.

CHAPTER 5: EFFECTS OF ORGANIC ADDITIVES ON THE IMPURITY AND GRAIN STRUCTURE OF ELECTRODEPOSITED COBALT

Published Work Disclosure: This chapter is based on previously published paper (Hu, Y.; Deb, S.; Li, D.; Huang, Q., Effects of organic additives on the impurity and grain structure of electrodeposited cobalt. Electrochim. Acta 2021, 368, 137594.)

Summary

Co films were electrodeposited with different additives including dimethylglyoxime, sodium chloride, and mercapto-propanesulfonate (MPS). A systematic study was conducted using scanning electron microscope, four-point probe, secondary ion mass spectrum, and X-ray diffraction to understand the effects of such additives on the morphology, resistivity, impurity incorporation, and grain structure of film, as well as how thermal annealing influences these attributes. Transmission electron microscope with energy dispersive X-ray spectroscopy and local electrode atom probe tomography were used to determine the distribution of different impurity elements. A pronounced grain structure change from columnar grains to pseudo-spherical grains was observed upon the addition of MPS in electrolyte or the incorporation of S in film. In addition to the precipitation of sporadic S-rich clusters, S and C were also found to segregate at the grain boundaries in annealed Co films, both of which are believed to correlate to the grain growth and a significant resistance drop upon annealing.

Introduction

Copper (Cu) has been used as the conducting metal in back end of the line (BEOL) wiring for many CMOS technology generations.[1] Electrodeposited Cu was selected not only for the defect-free superconformal filling enabled by organic additives[2] but also because of

the self-annealing phenomenon,[3] where the as deposited fine-grained Cu undergoes abnormal grain growth at room temperature resulting in a much improved resistivity and reliability. However, as the BEOL critical dimensions decrease to the mean free path of Cu or below, the resistivity of Cu in fine features increases exponentially,[4] posing significant challenges on the further scaling of interconnects and demanding alternative materials.[5] Among them, cobalt (Co) has been proposed, explored and, recently, adopted as one of the front runners to replace copper in the finest metal levels.[6] The electron mean free path in Co is much shorter than Cu, allowing further scaling. On the other hand, a higher melting point of Co (than Cu) provides advantages as it decreases diffusion and electromigration.

Damascene Cu plating processes have been well established in the industry. Not only have the different roles of organic additives in such processes been extensively investigated,[7] but also much effort has been made to understand the recrystallization and the effect of impurity on such recrystallization of the electrodeposited Cu films.[8-10] As discussed above, the so-called "self-annealing", or room temperature grain growth, was typically observed for electrodeposited Cu films with a fine grain size and minimum amount of impurity elements.[11] The latter is dependent on the deposition conditions and the organic additives used.[12] Due to the local deviation of the additive concentration or distribution inside the narrow trenches to be filled, the impurity incorporation behavior in small structures can be significantly different from that of a film, and the annealing process in BEOL fabrication is therefore typically carried out at an elevated temperature to facilitate, expedite and stabilize the grain growth.

While the effects of additive, annealing, and impurity incorporation on electrodeposited Cu have been well established,[13-15] very few reports are available on Co. Kelly et al.[16] reported a comprehensive study about Co film properties with different deposition methods (physical vapor deposition, chemical vapor deposition, and electrodeposition) and annealing treatment. The resistivity of Co films with different

deposition methods was measured and compared. Moreover, they found that the impurity level of Co films was related to deposition methods, electrolyte composition, and annealing process. Doubina et al. recently conducted a systematic study on the thermal annealing effect on the grain structure of plated Co films and lines, where grain coarsening was observed at around 300 to 350 °C.[17] In our previous work,[18-20] additives with a pair of conjugated oxime groups such as dimethylglyoxime (DMG) display strong suppression effects on Co deposition and a suppression breakdown occurred upon the reduction of adsorbed Co^{2+}-dioxime chelates. Superconformal filling using such additives has also been demonstrated and results will be published separately. In this paper, the effects of DMG additive and annealing process on the impurity incorporation, film sheet resistance, and grain structure of electrodeposited Co are reported. The impacts of two co-additives, sodium chloride (NaCl) and sodium 3-mercapto-1-propanesulfonate (MPS), are also investigated here as the source of Cl and S impurities, respectively.

Experimental

A homemade electrochemical cell with an electrolyte bridge to separate the catholyte and anolyte was used in this study. The counter electrode was a Co rod with a purity at least 99.9% and a surface area much larger than that of the cathode. Si coupons (2 cm by 2 cm squares, or 4 cm^2) were cleaved from a 3-inch blanket wafer with Co (30 nm, PVD) seed layer on Ta (5 nm, PVD) adhesion layer, and were used as cathodes. The Si coupon was mounted on a holder rotating in the same way as a rotating disk electrode. The electrical connection was made through a front pin contact to the Co seed. All Co films were deposited at -15 mA/cm^2 and 400 rpm for 400 s, corresponding to a thickness between 640 and 910 nm depending on the Faraday efficiency. This current density was selected as it is used in BEOL metallization. The selection is also based on our previous studies, where the suppression by DMG has broken down and impurity incorporation is expected to occur.[20] After

electrodeposition, all films were thoroughly rinsed in deionized (DI) water and then blow-dried using compressed air before analysis.

The Co makeup solution for deposition was the same as our previous studies, containing 0.3 M $CoSO_4$, 0.4 M H_3BO_3, and 0.1 g/L sodium dodecyl sulfate (SDS). The pH of Co solution was adjusted to 4.0 with H2SO4. Concentrated DMG solution (23,000 ppm), concentrated MPS solution (17,800 ppm), and concentrated NaCl solution (3550 ppm of Cl) were prepared by dissolving the corresponding chemicals in water. Calculated amounts of the concentrated additive solutions were then added into the Co makeup solution to introduce 100 ppm of each additive. All salts and organic additives were at least ACS grade and used as received. DI water with a resistivity of 18.2 MOhm-cm was used in all studies.

An Autolab 302 N potentiostat was used for all electrochemical studies. A home-built vacuum annealing system was used to anneal all Co films at 300 C for overall 20 h. The annealed Co films were cooled down to room temperature before unloading and were kept in N2 atmosphere in between annealing to minimize oxidation. A four-point probe setup was used to measure the film sheet resistance, a ratio between resistivity to the film thickness. A Bruker D8 powder X-ray diffractometer (XRD) with Co Kα source (wavelength = 1.79 Å) was used to perform film crystallographic analysis. The D8 powder diffractometer is equipped with a 2-dimensional x-ray detector, which collects the x-ray signal within a θ range from θ-α to θ+α. The range α is determined by the size of the detector and its distance from the specimen. During the data acquisition, the x-ray tube and detector are both fixed at same positions, θ1, θ2, or θ3, resulting in the collection of multiple segments of diffraction pattern. The neighboring segments slightly overlap so that a complete diffraction pattern is obtained by merging them together. The 2θ resolution used in data acquisition is 0.005°. A JEOL 7000 scanning electron microscope (SEM) was used to characterize the morphology of electrodeposited Co films, operated at 30 kV. Time-of-flight secondary ion mass

spectroscopy (ToF-SIMS) equipped with a Bi cluster liquid metal ion source was used to obtain the depth profiles of various elements in the electrodeposited Co films. Since the electrodeposited Co are dense films without porosity or density change, the SIMS signal of a same element between different Co films can be used as a direct comparison of the concentration of impurity. However, a comparison between different elements would be inaccurate due to the yield difference for different elements. A FEI Quanta 3D Dual Beam (FIB) with a 30 kV gallium ion beam was used to prepare samples for transmission electron microscope (TEM) and local electrode atom probe (LEAP) tomography. Cross-sectional grain structure observation with elemental analysis was carried out using FEI TITAN TEM with a Bruker EDAX energy dispersive spectroscopy (EDS) detector. A Cameca LEAP 5000 XS was used to analyze the specimens prepared with FIB. The base temperature was maintained at 30 K during analysis, and the specimens were analyzed with a laser power of 0.05 nJ. Atoms were ionized using high-voltage pulses at a frequency of 200 kHz.

Results and discussion

The effects of additives on the morphology of electrodeposited Co were first characterized using SEM and Figure 5-1 shows the top-down images. The Co film prepared in additive-free solution shows large and flake-shaped Co grains with sharp ridges, which is consistent with the literature.[21] Moreover, no significant changes in the shape or size of grains are observed after vacuum annealing at 300 °C for up to 20 h. This also confirms that no significant oxide has formed during or between annealing studies. The film morphology, however, has dramatically changed after the addition of 100 ppm DMG. The flake-shaped Co grains become smaller and less frequent, and more irregular Co grains are observed. Based on our previous studies, DMG suppresses Co deposition and catalyzes hydrogen evolution reaction. The continuous formation and adsorption of Co^{2+}-DMG complex may have prevented the growth of large Co nuclei. Adding 100 ppm NaCl into the solution further

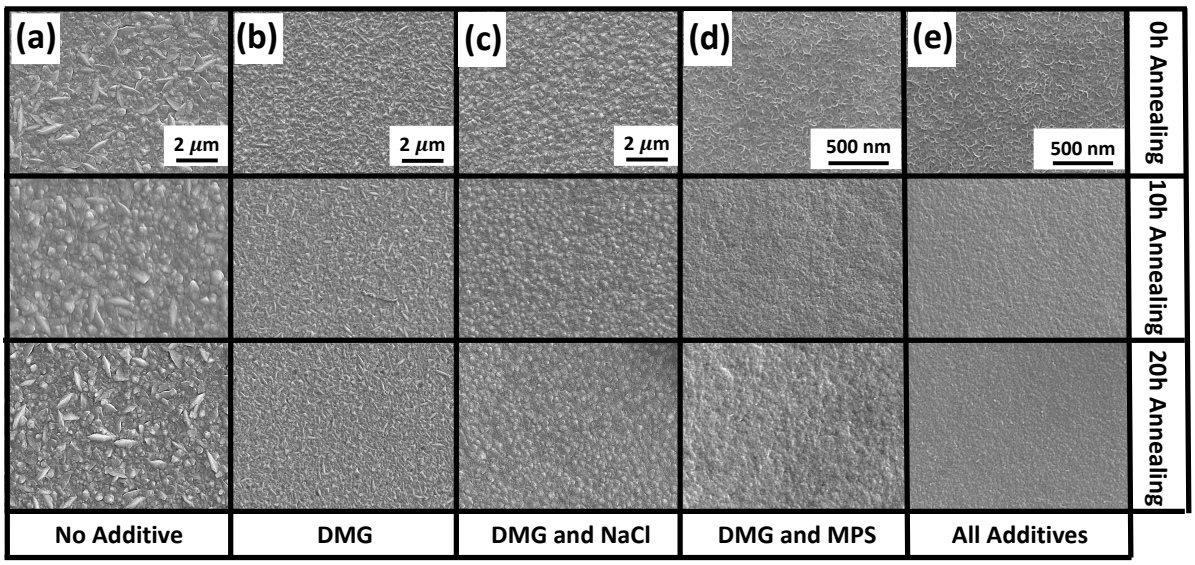

Figure 5-1. Top-down SEM images of electrodeposited Co films from solution containing (a) no additive; (b) 100 ppm DMG; (c) 100 ppm DMG and NaCl; (d) 100 ppm DMG and MPS; (e) 100 ppm DMG, NaCl, and MPS before and after annealing.

changes the shape of Co grains, that is, the flake shaped grains become even more sparse and the majority of grains are more spherical. This seems to suggest that the film deposition is dominated by the effect of DMG and this effect might be strengthened by the presence of chloride anion. A fourth case was studied with 100 ppm MPS added into the solution with DMG. Different from the chloride ion, the addition of MPS dramatically changed the film morphology. The size of Co particles further decreases and worm-shaped morphology features appear. It is noted here that the SEM images are at different magnifications for different films and that the worm-shaped features observed here are indeed much smaller than the ridged flake shaped particles in the additive free case. Thiol terminated molecules are known to bond with transition metal surfaces such as Co and form a mono layer.[22] Our recent work shows that the adsorption and desorption of MPS, or a Co-MPS complex, on deposited Co can sometimes be manifested as a spontaneous electrochemical oscillation at certain conditions.[23] The change of film morphology observed here seems to be consistent with the presence of a second adsorbate upon the addition of MPS. If a competitive adsorption between two adsorbates (Co-MPS complex and Co^{2+}-DMG complex) occurs,

depending on the interaction of the two, the change of the surface coverages would be expected to have an impact on the nucleation, growth, and therefore morphology of films. On the other hand, the annealing process completely changes the surface morphology, where the worm-shaped features disappear and a dense compact film with small spherical grains was obtained. When all three additives (DMG, Cl, MPS) are present in the solution, the surface morphology is similar to the case with only two additives, DMG and MPS, consistent with the above discussion on the stronger effects from DMG and MPS than chloride ion.

The effects of additive on impurity incorporation in Co films were studied using SIMS. The elemental depth profiles are shown in Figure 5-2. The profiling runs from the top surface of Co to the silicon (Si) substrate. The depth of the raster crater was determined with an AFM stylus. A sharp increase of Si signal upon the emerge of substrate is used as the end point of analysis and to estimate the thickness of Co film. In addition, the volatile CN species is used in SIMS to represent the concentration of N. Figure 5-2(a) and (b) show the depth profiles of Co films deposited without additives and with 100 ppm DMG, respectively. The SIMS signals of all impurity elements are much higher at the film surface, i.e. the beginning of analysis, because of the surface oxide as well as the matrix effect on the signal yield. The film thickness decreases from 780 nm to 640 nm upon the addition of DMG, where the Co deposition is suppressed. The presence of DMG also enhances the hydrogen evolution reaction,[24-25] further decreasing the current efficiency and film thickness in galvanostatic deposition. The comparison between the two films shows that the amount of N, measured as the count of CN species, dramatically increases for 20 times, from 50 to 1000 after DMG is added. At the same time, the counts of C and S both increase for about 7 times, from 15 to 100. Since DMG is the only N source in the electrolyte, the significant increase of CN species agrees with our previous work,[20] where the suppression effect of dioxime on Co deposition was concluded to result from a Co^{2+}-dioxime complex formed through a pair of

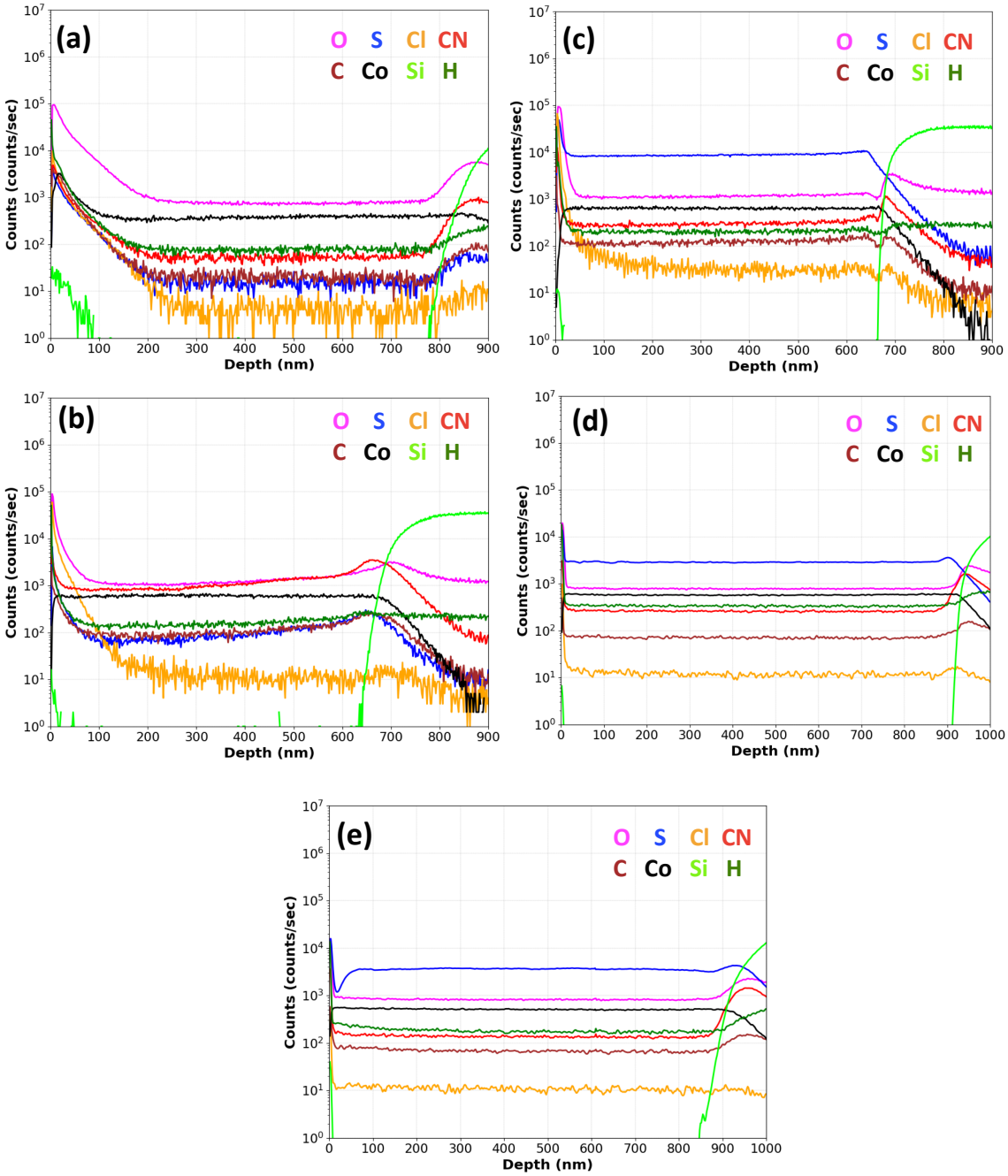

Figure 5-2. SIMS elemental depth profiles of electrodeposited Co films from solution containing (a) non-additive before annealing; (b) 100 ppm DMG before annealing; (c) 100 ppm DMG and MPS before annealing; (d) 100 ppm DMG, NaCl, and MPS before annealing; (e) 100 ppm DMG, NaCl, and MPS after 20 h annealing.

conjugated N-atoms in dioxime. The complex molecule adsorbs on electrode surface inhibiting Co deposition, but breaks down and gets incorporated into film at a sufficiently negative potential or a cathodic current. Interestingly, the increase of C signal is much less pronounced than N. Because the SIMS signal was not calibrated using a standard, it is

unclear if this difference results from the different yields of element or a lower incorporation of C. The latter, if true, may suggest that the C single bond and N bond in DMG breaks frequently upon the DMG incorporation.

The SIMS results here also show that the formation and incorporation of this Co^{2+}-DMG adsorbate facilitates the incorporation of sulfur, an element not present in DMG. This suggests a co-incorporation from the inorganic sulfate or the surfactant dodecyl sulfate. However, neither anion shows strong affinity with electrode surface, particularly at a negatively biased surface, resulting in very low S incorporation. Such co-incorporation is also observed for chloride, probably from the inevitable contamination from laboratory ambient or impurities in chemicals, but to a much lower degree and with a much lower concentration.

Figure 5-2(c) shows the depth profile of Co film deposited with 100 ppm DMG and 100 ppm MPS. A comparison with Figure 5-2(a) shows a significant increase of S concentration from 100 to 10,000, suggesting that MPS dominates the S incorporation in the Co film. This is not uncommon as the thiol group has a strong affinity with metal and such a significant S incorporation has been widely observed in Cu deposition in presence of MPS.[26] More interestingly, the concentration of CN decreases 3 folds, from 1000 to 300, while other elements such as C, O, and Cl all remained about the same, indicative of a lower incorporation rate of DMG in the presence of MPS. As discussed above in Figure 5-1, it is believed that both Co-MPS complex and Co^{2+}-DMG complex are adsorbed on electrode surface and suppress Co deposition. Therefore, this result not only demonstrates a competitive adsorption between the Co^{2+}-DMG and Co-MPS complexes, but also confirms a direct correlation between impurity incorporation with surface adsorbates. Moreover, the thickness of these two films are nearly the same, which means the addition of MPS on top of DMG does not further change the current efficiency of Co deposition. When all three additives are present in the solution, shown in Figure 5-2(d) and similar to Figure 5-2(c), only

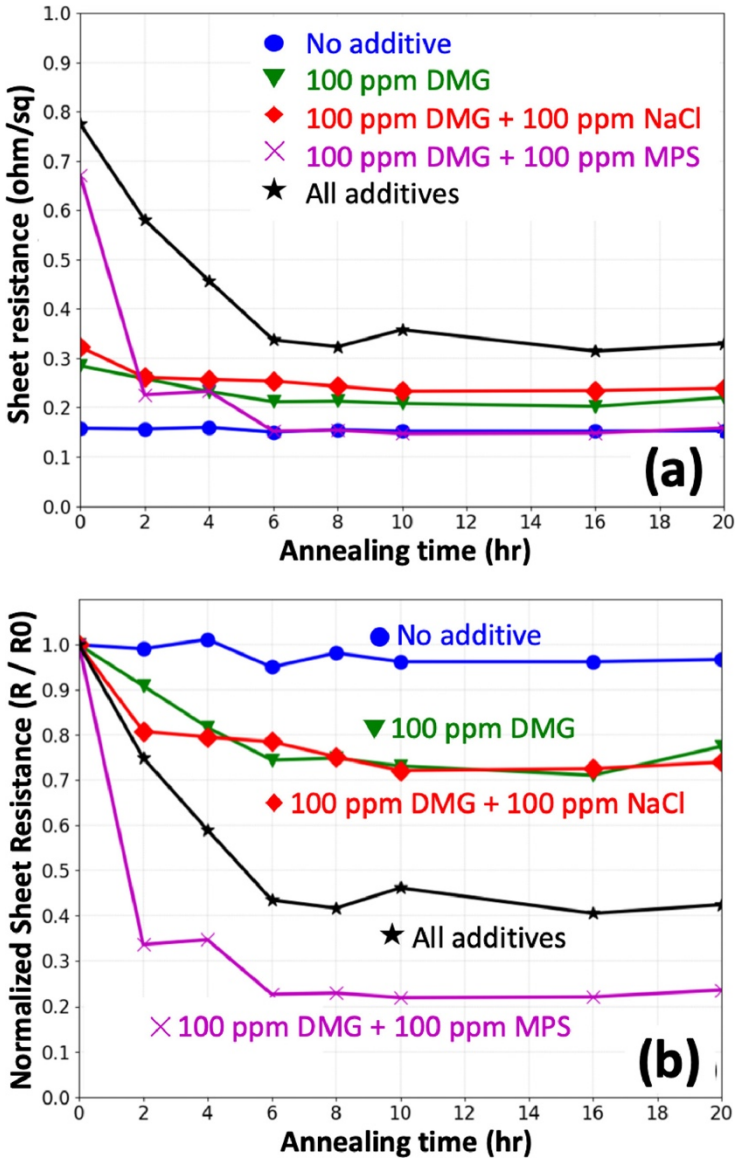

Figure 5-3. (a) Sheet resistance change with different additives and annealing conditions as indicated; (b) Normalized Sheet resistance change with different additives and annealing conditions as indicated.

S and CN incorporation increase compared with Figure 5-2(a). Surprisingly though, the concentration of Cl in film maintains at a similar level despite the addition of NaCl in electrolyte. The addition of Cl on top of DMG and MPS results in a decrease in S incorporation. It also results in an increase in current efficiency at the deposition condition used as the film thickness increases from about 640 nm to 910 nm. The mechanism is not clear and no significant impact was observed in film morphology. Figure 5-2(e) shows the impurity profile of the same sample in Figure 5-2(d), deposited with all additives but after

300 °C vacuum annealing for 20 h. All impurities remain nearly the same except for CN concentration, which decreases for about 50% upon the annealing. It is not shown here, but the amount of H in Co film decreases significantly upon annealing as well. Both H and N can form volatile species themselves and do not form strong ionic bonds with Co metal. Such attributes are different from other impurity elements such as C, O, Cl, S, and are believed to cause the decrease of their concentrations upon annealing.

It is well known that the impurities in copper films have a strong impact on grain coarsening upon annealing, typically characterized as a decrease of sheet resistance along annealing. A similar study was carried out and Figure 5-3(a) illustrates the sheet resistance change of five Co films deposited with different additives along a course of 20 h annealing at 300 °C. Before annealing, it is evident that the higher sheet resistance seems to correlate with higher impurity levels in the film. The Co film deposited without additive shows the lowest sheet resistance at around 0.158 /sq. This sheet resistance approximately doubles with the presence of DMG in electrolyte, and almost quintuples upon the addition of MPS on top of DMG. Moreover, the addition of Cl has shown very little increase in the sheet resistance, apparently consistent with the observation in morphology, where DMG and MPS also show the most predominant effects over Cl. It is worth noting here that the film thickness is not a constant as the current efficiency changes. But the change in film thickness estimated from SIMS profiles is much less pronounced than the sheet resistance. For example, the film thickness decreases for about 20% from additive free case in Figure 5-2(a) to the DMG with MPS case in Figure 5-2(c), but the sheet resistance increases for about 400%. In conjunction with the SIMS results, it can be seen that the addition of MPS or the incorporation of S seems to contribute to such a huge increase in sheet resistance. The sheet resistance is further normalized with the as-deposit resistance value (R_0) and is presented in Figure 5-3(b), where the resistance decreases along annealing and stabilizes after about 6 hours. The sheet

resistance of S-containing Co films, namely the films deposited with MPS, drastically drops up to 78% after 6 h annealing. The resistance evolution for Co films deposited with additives but without MPS, that is, films with much lower S-incorporation, stabilizes at about 30%, regardless of the presence of Cl. No significant resistance change is observed for film deposited additive free. Doubina et al.[17] reported that the low resistivity Co film with larger Co grains could be obtained when the film was annealed at 300 °C for 60 min. In our results, the S-containing Co films show the sharp drop of resistance upon 300 °C annealing and similar large grains are observed as shown in Figure 5-5(c).

While it is clear that the use of additives in electrolyte leads to the increase of sheet resistance, the effects of these additives differ. Again, the use of MPS and the high S incorporation in film show the strongest impact on sheet resistance, which cause not only the most significant increase of resistance for as deposited films but also the most pronounced decrease of sheet resistance along with annealing. On the other hand, incorporation of C and N from the addition of DMG in electrolyte shows a much less pronounced effect, where the sheet resistance also increases for as deposited films and decreases for annealed films, but both to a lower degree. Electrodeposited metal films with fine grains, when annealed, typically experience a change in microstructure, or grain growth, along with the outgassing or redistribution of impurity elements. Such changes often cause a sheet resistance decrease by mitigating the electron scattering at grain boundaries. However, the grain growth behavior or the easiness of grain boundary elimination is highly related to not only the impurity elements but also the grain structures of as deposited films.

The crystallographic structure of films was characterized with X-ray diffraction. Figure 5-4(a) shows the diffraction pattern of as-deposited Co films with different additives. The X-ray signal is plotted in the log scale. Both HCP and FCC Co phases are observed in all films. No peak is observed from the single crystal Si substrate with the powder diffractometer

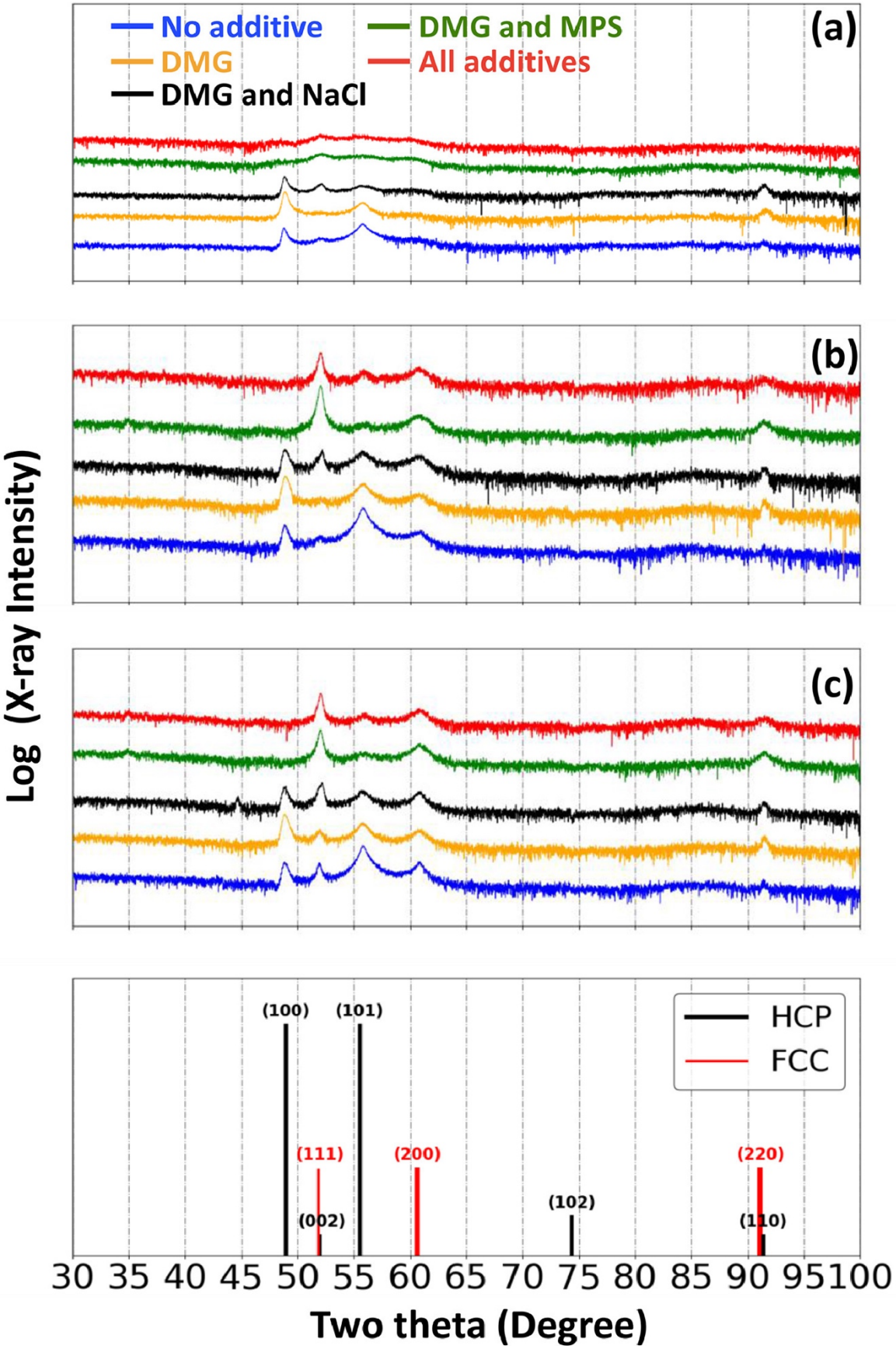

Figure 5-4. XRD results of electrodeposited Co films from solution containing different additives with (a) 0 h annealing; (b) 10 h annealing; (c) 20h annealing.

used in the study. The Co films deposited without MPS are polycrystalline with a predominant HCP structure, with the sharp peaks at 2 of 48.8°, 55.5°, 52.5° and 91.2° assigned to Co HCP (100), (101), (002) and (110) orientations, respectively. While two of the peaks at 48.8° and 91.2° are also close to the FCC (111) and FCC (220) reflections, respectively, the FCC (200) peak at 60.6° is broad and weak, suggesting that either the FCC grains are extremely refined or the fraction of FCC phase is extremely minor. This observation holds largely the same regardless of the addition or the absence of DMG and chloride, except for a small shift of the relatively preferred orientation within the HCP phase. The introduction of MPS into the electrolyte significantly changes the crystallinity of Co films. While all the above peaks are also observed, the peaks are much broader and weaker, indicative of much finer grains for both phases. As discussed earlier, these films show a much higher sheet resistance, as well as a much higher sulfur incorporation. Here, the much finer grains are believed to contribute to the higher sheet resistance through grain boundary scattering. Adsorbates such as halides are known to selectively adsorb on certain facets of metal crystals.[27] Such preferences are believed to relate to the change of the preferred crystallographic phases of Co observed here upon the addition of DMG and Cl. However, the addition of MPS seems to cause a ubiquitous peak broadening regardless of the orientation, suggesting that the thiol group in MPS has strong affinity with all Co facets and renders MPS a grain refiner.

Polycrystalline Co films with coarsened grains are obtained upon 300 °C vacuum annealing for 10 h. This grain coarsening effect are more pronounced for the films deposited with MPS, where the grains are refined. As shown in Figure 5-4(b), four strong reflections, HCP (002), (101), (110) and FCC (200), emerged after annealing for these films. No significant grain growth is observed in HCP (100) direction. Among the four peaks, HCP (002) seems to be the strongest, indicative of a preferred growth of HCP grains in (002)

direction. On the other hand, Co films deposited without MPS show much less pronounced change in the XRD reflections. No notable change other than the emergence of a weak FCC (200) peak at 60.6° is observed. Figure 5-4(c) shows the diffraction patterns of the same Co films after 20 h annealing. No further change is observed in crystallinity for Co films deposited with MPS. For the other Co films prepared without MPS, no further change was observed either, except for a sharper HCP (002) peak, suggesting that a crystallographic preference gradually evolves as the annealing continues. This evolution takes longer time and the preference is less prominent than the films prepared with MPS. This is consistent with the fact that the latter have much finer grains, that is, much higher grain boundary energy and easier boundary elimination or grain growth. However, it is known from SIMS results that the films also incorporate different impurity elements, particularly S and, to some extent, N. Impurities can increase film resistivity through electron scattering on these foreign elements. More importantly, depending on the mobility, they may segregate at grain boundaries as grains grow. Such segregated impurity can pin the grain boundary, slowing down the grain growth and resistance drop during annealing. Microscopic composition analysis techniques are needed to further understand the roles that the different impurities may play in the grain structure and resistivity.

Cross sectional TEM in conjunction with EDS was first attempted to characterize the grain structure and impurity distribution for two of annealed films, one deposited with DMG and the other with all three additives. Both films were deposited for 400 s at a same current density of 15 mA/cm^2 and a same rotation rate of 400 rpm. The conditions are similar to films presented in Figure 5-1, and the film thicknesses are also consistent, at about 600 nm. Figure 5-5(a) shows the dark field cross-sectional TEM micrographs of Co films with 100 ppm DMG after 20 h annealing. Columnar grains across the entire film thickness are observed with lateral grain size of about 100 nm. EDS elemental maps around a grain

boundary are acquired and presented in Figure 5-5(b). A slight contrast is observed between the two grains for Co, S, and Cl signals. This is because of the difference in the grain orientation, resulting in different signal intensities. But a uniform distribution of impurities is observed across the grains and grain boundaries. Line scans were also carried out perpendicularly across the grain boundary, but no aggregation of any element could be identified. An organic coating was applied on Co films prior to TEM sample preparation, resulting in the top region rich in carbon and oxygen.

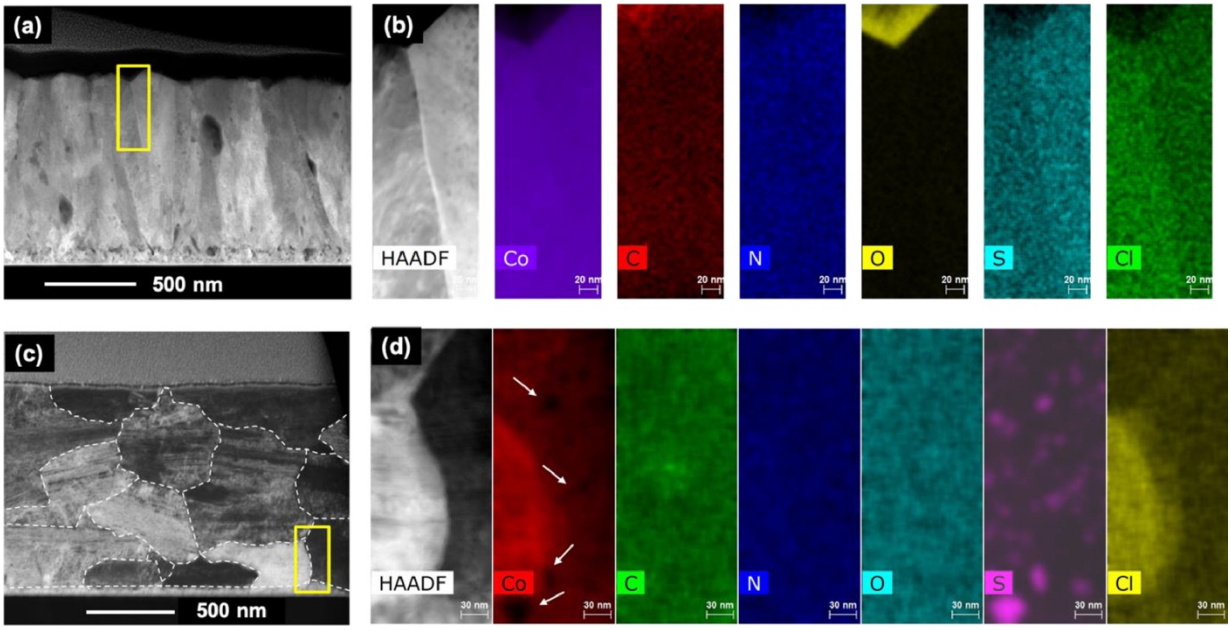

Figure 5-5. (a, c) Cross sectional FIB-TEM images and (b, d) EDS elemental maps around a grain boundary of Co films electrodeposited with (a, b) 100 ppm DMG and (c, d) 100 ppm DMG, NaCl, and MPS. Both films were annealed at 300 °C for 20 h annealing. White dashed lines in (c) are used to outline the grains. Yellow boxes in (a, c) are used to outline the location for EDS mapping.

Similar analysis was also carried out for a Co film deposited with all three additives (DMG, MPS, Cl) after 20 h annealing, and the results are shown in Figure 5-5(c). As outlined with the white dashed lines, the grain structure dramatically changes as compared with Figure 5-5(a). Instead of the columnar grains, randomly distributed, irregular but more spherical, grains with a more uniform size between 200 and 500 nm are obtained. It is known from XRD that the as deposited film has much finer grains. The more spherical grains observed

here post anneal suggest a random nucleation of initial grains and an anisotropic grain growth with a more uniform growth rate in all crystal orientations. Elemental maps are also acquired at a boundary between two grains, as indicated with a yellow box in the TEM image, and the results are shown in Figure 5-5(d). A clear contrast in signal density was observed between the two grains for Co and Cl, similar to Figure 5-5(b). It is worth noting that an intermediate Cl content region seems to be present at the grain boundary, resulting in two apparent boundaries with one on the left of the other. This indicates that the grain boundary in TEM micrograph may not be perfectly perpendicular to the TEM sample lamella and the projected view of the tilted grain results in such halo. Interestingly, whilst an aggregation of impurities at grain boundary could not be determined here, numerous sulfur-rich clusters are clearly observed across the entire field of view. Carbon accumulation occurs as well, albeit to a much less extend, forming one cluster. In addition, a lower cobalt signal is observed in the sulfur clusters (highlighted with white arrows), probably resulting from a combination of different crystal structure and orientation, and a lower cobalt concentration in a cobalt sulfide compound region. Since only one C cluster was observed, multiple regions in the lamella were examined and such observations have been confirmed.

EDS has a typical detection limit of 0.1 wt%.[28] and it can be even poorer for light elements such as the ones of interest in this study. While no impurity segregation at grain boundary is confirmed with TEM-EDS, such segregation cannot be completely ruled out because the impurity concentration at grain boundaries could still be well below the detection limit of EDS. Therefore, local electrode atom probe (LEAP) tomography was carried out to further characterize the distribution of different impurity elements in the annealed Co films. A same film as in Figure 5-5(c), deposited with all additives and annealed, was used to ensure high impurity incorporation. Multiple pillars with a footprint diameter of no more than 100 nm were prepared from a TEM lamella to ensure the inclusion of a grain boundary in at

least one of the pillars. No stress or charge accumulation was observed and the Co pillars well survived the entire analysis, that is, about 140 nm deep profiling. The entire mass spectrum is provided in Supplementary Material with all peaks assigned to a reasonable species to enable the reconstruction of the 3D pillar. The average concentration of all species other than hydrogen and hydrocarbon are well below 0.1 at% (even much lower in wt%), consistent with Figure 5-5, where no distribution other than S-rich clusters could be observed in TEM. Figure 5-6 shows the elemental distribution maps projected from an angle where a grain boundary can be clearly identified. As shown in the Co map, clusters rich in S were also observed randomly distributed across the film, consistent with the TEM results. Furthermore, CoO with a m/z ratio 75 have been observed as very small clusters randomly distributed across the entire film. However, such clusters were not evident in the oxygen map obtained from TEM EDS, probably due to the much smaller size.

The important result from LEAP analysis is that S and C are found to significantly accumulate at grain boundaries. At the specific view angle in Figure 5-6, a "χ" shaped segregation of S and C is observed, where the two impurity elements appear to be complementary to each other in terms of the segregation. In the C map, a "λ" shaped distribution was clearly observed. This "λ" shaped boundary is still observed, but much less pronounced, in S map. In addition, S accumulates along another short grain boundary located upper right to this "λ" shape. Overlapping the two maps not only confirms the same location of the grain boundaries, but also reveals the complete "χ" shape of the segregation.

Three LEAP videos are included in the Supplementary Materials with 360° view of the distribution of S and C in the entire pillar specimen. It can be seen from the videos, particularly the ones revolving around Y and Z axes, that the longer tail of the "λ" shape represents the projection of a curved grain boundary, which intersects the pillar from the top

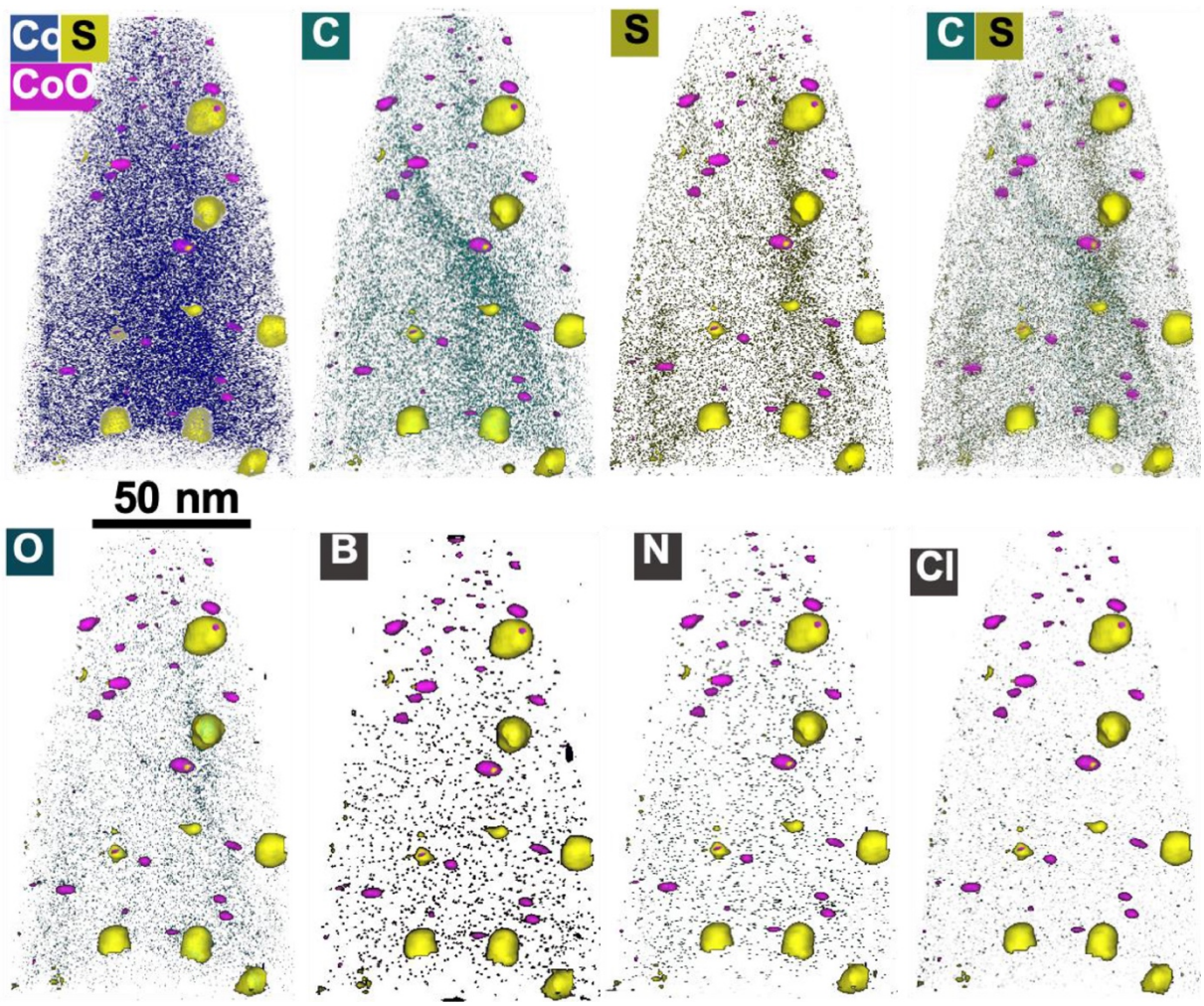

Figure 5-6. LEAP tomography elemental mapping and mass spectroscopy results of electrodeposited Co film with 100 ppm DMG, NaCl, and MPS after 20 h annealing.

cone surface to the cone base, resulting in a curved trapezoid surface. As discussed in Figure 5-4(c), the grains are spherical and grain boundaries are expected to be curved not only in X-Y view plane, but also in Y-Z and X-Z view planes as evidenced in the videos. On the other hand, while the other line of the "χ" shape may also result from a grain boundary, it is less obvious or conclusive. It is worth noting that no morphological patterns were observed on the pillar by SEM that can possibly relate to the observed impurity segregation. While TEM observation was not performed on the same pillar to avoid high energy beam damages, the C and S segregation observed in the 3D animation highly likely correlates to a curved grain boundary. In addition to S and C, some very minor accumulation was observed for O around the cross point of the "χ" shaped boundary. Again, numerous CoO clusters were observed

and are believed to be the predominant form of O in the film. This might relate to a stronger electron affinity of O and thus a stronger bond between Co and O, resulting in lower mobility of O. The concentration of other elements such as B, N and Cl, are much lower and no accumulation could be determined.

The effects of the incorporation and movement of impurities have been well studied in the electrodeposited Cu films. It has been reported that a higher annealing temperature not only facilitates the grain boundary annihilation but also promotes impurity mobility, both accelerating the grain growth.[29] Our results here confirm that impurities not only affect the Co grain structure but also redistribute and aggregate in Co films, which is believed to be responsible for the change of sheet resistance.

It is worth mentioning that this Co impurity and microstructure study is based on blanket films, which can be different from fine trenches. Because of the geometry of trench, the growth mode, grain structure, and the impurity incorporation of Co can be different. For example, an additive concentration gradient in the trenches is often needed to achieve the defect free filling. In addition, the current density in the feature is different from the applied current density due to the interaction between additives and the Co surface. Moreover, the filling rate in the trench is typically faster than the deposition on field region. Therefore, as mentioned above, it is very difficult to experimentally mimic the Co deposition in the trenches with a blanket film. Results shown in this study aims to provide a fundamental understanding on the effect of organic additives on the impurity incorporation and grain structure of electrodeposited Co, as well as how the impurities redistribute in relation with grain growth upon annealing.

Conclusion

A systematic study was carried out to understand the effects of additives in electrolyte on the properties of electrodeposited Co films, such as morphology, sheet resistance, grain

structure, the incorporation and distribution of impurity elements. The addition of additives, particularly MPS, not only smooths out the film surface, decreases the grain size, and increases the sheet resistance, but also dramatically amplifies the resistance drop upon annealing. SIMS analysis shows that the presence of DMG in electrolyte predominantly introduces N and C impurity into films. On the other hand, the further addition of MPS significantly increases S and decreases N incorporation probably due to a competitive adsorption between the DMG and MPS on electrode surface. XRD confirms that the addition of MPS results in smaller grains in the electrodeposited Co films. While such a refined grain structure contributes to a higher sheet resistance of as deposited Co films, it also eases the grain growth upon annealing resulting in the most significant resistance drop among all the different additive cases studied. Columnar grain structure and pseudo-spherical grains are observed in annealed Co films deposited without and with MPS, respectively. With atom probe tomography, randomly distributed S-rich and CoO clusters in nanometer scale are observed after the annealing of Co films deposited with all additives. More importantly, significant S and C segregation and marginal O segregation at grain boundaries are proved to occur during the annealing, probably correlating to the grain growth. The findings in this study are believed to provide understanding and guidelines for chemistry and process design to fabricate low resistance Co interconnects structures.

Acknowledgments

National Science Foundation is acknowledged for support through Grant CMMI-1662332. Preliminary TEM-EDS experiments were supported by the U.S. Department of Energy (DOE), Office of Science (SC), Office of Basic Energy Sciences (BES), Early Career Research program under Award # KC0203020:67037. YH thanks the Graduate Council at The University of Alabama for a fellowship support. Heng-Yong Nie at The University of Western Ontario was acknowledged for SIMS analysis. The Central Analytical Facility at the

University of Alabama and the Materials and Manufacturing Research Facility at US Air Force Research Laboratory are acknowledged for the access and training of equipment for characterization.

References

1. Andricacos, P. C.; Uzoh, C.; Dukovic, J. O.; Horkans, J.; Deligianni, H., Damascene copper electroplating for chip interconnections. *IBM Journal of Research and Development* **1998,** *42* (5), 567-574.

2. Moffat, T.; Wheeler, D.; Huber, W.; Josell, D., Superconformal electrodeposition of copper. *Electrochem. Solid-State Lett.* **2001,** *4* (4), C26-C29.

3. Harper, J.; Cabral Jr, C.; Andricacos, P.; Gignac, L.; Noyan, I.; Rodbell, K.; Hu, C., Mechanisms for microstructure evolution in electroplated copper thin films near room temperature. *J. Appl. Phys.* **1999,** *86* (5), 2516-2525.

4. Steinhögl, W.; Schindler, G.; Steinlesberger, G.; Engelhardt, M., Size-dependent resistivity of metallic wires in the mesoscopic range. *Physical Review B* **2002,** *66* (7), 075414.

5. Gall, D., Electron mean free path in elemental metals. *J. Appl. Phys.* **2016,** *119* (8), 085101.

6. Mont, F. W.; Zhang, X.; Wang, W.; Kelly, J. J.; Standaert, T. E.; Quon, R.; Ryan, E. T. In *Cobalt interconnect on same copper barrier process integration at the 7nm node*, 2017 IEEE International Interconnect Technology Conference (IITC), IEEE: 2017; pp 1-3.

7. Moffat, T. P.; Wheeler, D.; Kim, S.-K.; Josell, D., Curvature enhanced adsorbate coverage model for electrodeposition. *J. Electrochem. Soc.* **2006,** *153* (2), C127-C132.

8. Kelly, J.; Nogami, T.; Van der Straten, O.; Demarest, J.; Li, J.; Penny, C.; Vo, T.; Parks, C.; DeHaven, P.; Hu, C.-K., Electrolyte additive chemistry and feature size-dependent impurity incorporation for Cu interconnects. *J. Electrochem. Soc.* **2012,** *159* (10), D563-D569.

9. Huang, Q.; Avekians, A.; Ahmed, S.; Parks, C.; Baker-O'Neal, B.; Kitayaporn, S.; Sahin, A.; Sun, Y.; Cheng, T., Impurities in the electroplated sub-50 nm Cu lines: The effects of the plating additives. *J. Electrochem. Soc.* **2014,** *161* (9), D388-D394.

10. Stangl, M.; Lipták, M.; Acker, J.; Hoffmann, V.; Baunack, S.; Wetzig, K., Influence of incorporated non-metallic impurities on electromigration in copper damascene interconnect lines. *Thin Solid Films* **2009,** *517* (8), 2687-2690.

11. Lagrange, S.; Brongersma, S.; Judelewicz, M.; Saerens, A.; Vervoort, I.; Richard, E.; Palmans, R.; Maex, K., Self-annealing characterization of electroplated copper films. *Microelectron. Eng.* **2000,** *50* (1-4), 449-457.

12. Stangl, M.; Liptak, M.; Fletcher, A.; Acker, J.; Thomas, J.; Wendrock, H.; Oswald, S.; Wetzig, K., Influence of initial microstructure and impurities on Cu room-temperature recrystallization (self-annealing). *Microelectron. Eng.* **2008,** *85* (3), 534-541.

13. Barmak, K.; Gungor, A.; Cabral Jr, C.; Harper, J., Annealing behavior of Cu and dilute Cu-alloy films: Precipitation, grain growth, and resistivity. *J. Appl. Phys.* **2003,** *94* (3), 1605-1616.

14. Bonou, L.; Eyraud, M.; Denoyel, R.; Massiani, Y., Influence of additives on Cu electrodeposition mechanisms in acid solution: direct current study supported by non-electrochemical measurements. *Electrochim. Acta* **2002,** *47* (26), 4139-4148.

15. Hu, C.-K.; Gignac, L.; Baker, B.; Liniger, E.; Yu, R.; Flaitz, P. In *Impact of Cu microstructure on electromigration reliability*, International Interconnect Technology Conference, IEEE 2007, IEEE: 2007; pp 93-95.

16. Kelly, J.; Kamineni, V.; Lin, X.; Pacquette, A.; Hopstaken, M.; Liang, Y.; Amanapu, H.; Peethala, B.; Jiang, L.; Demarest, J., Annealing and Impurity Effects in Co Thin Films for MOL Contact and BEOL Metallization. *J. Electrochem. Soc.* **2019,** *166* (1), D3100-D3109.

17. Doubina, N. V.; Spurlin, T. A.; Opocensky, E. C.; Reid, J. D., The Effect of Thermal Annealing on Cobalt Film Properties and Grain Structure. *MRS Advances*, 1-9.

18. Huang, Q.; Lyons, T.; Sides, W., Electrodeposition of Cobalt for Interconnect Application: Effect of Dimethylglyoxime. *J. Electrochem. Soc.* **2016,** *163* (13), D715-D721.

19. Hu, Y.; Huang, Q., Effects of Dimethylglyoxime and Cyclohexane Dioxime on the Electrochemical Nucleation and Growth of Cobalt. *J. Electrochem. Soc.* **2019,** *166* (1), D3175-D3181.

20. Lyons, T.; Huang, Q., Effects of Cyclohexane-Monoxime and Dioxime on the Electrodeposition of Cobalt. *Electrochim. Acta* **2017,** *245*, 309-317.

21. Pradhan, N.; Singh, P.; Tripathy, B.; Das, S., Electrowinning of cobalt from acidic sulphate solutions—effect of chloride ion. *Miner. Eng.* **2001,** *14* (7), 775-783.

22. Caruso, A.; Wang, L.; Jaswal, S.; Tsymbal, E. Y.; Dowben, P. A., The interface electronic structure of thiol terminated molecules on cobalt and gold surfaces. *Journal of materials science* **2006,** *41* (19), 6198-6206.

23. Hu, Y.; Huang, Q., Oscillatory Behavior in Cobalt Electrodeposition with 3-Mercapto-1-Propanesulfonate. *The Journal of Physical Chemistry C* **2020**.

24. Jacques, P.-A.; Artero, V.; Pécaut, J.; Fontecave, M., Cobalt and nickel diimine-dioxime complexes as molecular electrocatalysts for hydrogen evolution with low overvoltages. *Proceedings of the National Academy of Sciences* **2009,** *106* (49), 20627-20632.

25. Valdez, C. N.; Dempsey, J. L.; Brunschwig, B. S.; Winkler, J. R.; Gray, H. B., Catalytic hydrogen evolution from a covalently linked dicobaloxime. *Proc Natl Acad Sci U S A* **2012,** *109* (39), 15589-93.

26. Demers, H.; Emekli, U.; Lifshin, E.; West, A., Characterization of Electrodeposited Copper Films with Time-of-Flight SIMS. *Microsc. Microanal.* **2009,** *15* (S2), 492-493.

27. Ghosh, S.; Manna, L., The many "facets" of halide ions in the chemistry of colloidal inorganic nanocrystals. *Chem. Rev.* **2018,** *118* (16), 7804-7864.

28. Goldstein, J. I.; Newbury, D. E.; Michael, J. R.; Ritchie, N. W.; Scott, J. H. J.; Joy, D. C., *Scanning electron microscopy and X-ray microanalysis*. Springer: 2017.

29. Brongersma, S.; Kerr, E.; Vervoort, I.; Saerens, A.; Maex, K., Grain growth, stress, and impurities in electroplated copper. *J. Mater. Res.* **2002,** *17* (3), 582-589.

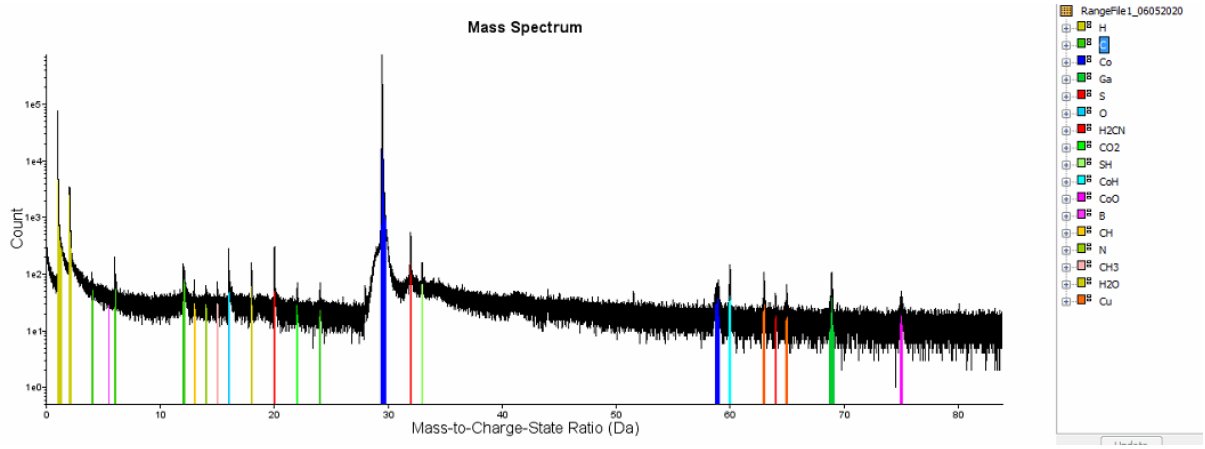

Figure S 5-1. The entire mass spectrum acquired from the LEAP analysis is shown below, with the species assigned to each of the peak.

Ion Type	Count	Ranged (%)
H	1387799.0	4.0215%
C	22124.639	0.0641%
Co	3.2934378E7	95.4351%
Ga	10068.859	0.0292%
S	27311.12	0.0791%
O	10817.547	0.0313%
H2CN	53839.277	0.1560%
CO2	6487.099	0.0188%
SH	10052.59	0.0291%
CoH	16171.368	0.0469%
CoO	3939.771	0.0114%
B	-183.93904	NA
CH	3214.7412	0.0093%
N	898.0574	0.0026%
CH3	3877.3352	0.0112%
H2O	10454.168	0.0303%
Cu	8206.482	0.0238%
Cl	83.65973	0.0002%

Figure S 5-2. The average concentration of all species in MS is listed below in a unit of atomic percent. The weight percent would be much lower for most of them with a lower mass than Co.

CHAPTER 6. CONCLUSIONS

Conclusions

The work presented in this dissertation provides a systematic study about the effects of a new class of suppressing organic additives, dioximes (dimethylglyoxime, cyclohexane dioxime, and furil dioxime), on the electrochemical deposition process of cobalt. The electrochemical nucleation of cobalt on diffusion barrier-liner materials are investigated and a double peak nucleation phenomenon due to a new two-step nucleation mechanism in presence of additives are discovered. In addition, the relationship between plating process and cobalt film properties such as impurity, grain structure, and electrical resistance are correlated.

In Chapter 2, the effects of DMG and CHD on cobalt nucleation process are studied. A typical 3D nucleation process controlled by hemispheric diffusion are observed. Two current peaks are observed with the addition of DMG or CHD in chronoamperometry studies, which is consistent with a proposed two-step nucleation mechanism. The first current peak is identified as the nucleation upon the reduction of Co-dioxime chelate, and the second peak as nucleation current from free Co^{2+} reduction. This mechanism is further confirmed with a controlled experiment, where only the first current peak was observed with all Co^{2+} being present as the chelate. Galvanostatic deposition studies show that the addition of DMG or CHD dramatically suppressed the formation of cobalt nuclei and CHD has a stronger suppression effect on Co nucleation than DMG.

In Chapter 3, the effects of FD on Co electrodeposition are studied. Suppression effect on Co deposition by FD is observed in CV as well as chronoamperometry nucleation studies. The total current transients during chronoamperometry nucleation are deconvoluted into

contributions from the capacitive charging, 3-D Co nucleation and growth, and the surfacearea dependent side reaction. Based on this model, the catalytic effect of Co-dioxime chelate on the side reaction rate is confirmed. The initial Co deposition is found to follow the progressive nucleation behavior for almost all cases. Galvanostatic deposition studies show that the nucleus shape, nucleation density as well as the morphology of thick films are highly dependent on the FD concentration and deposition current.

In Chapter 4, a potential oscillation is observed during galvanostatic deposition of Co in the presence of MPS, which mildly suppresses the deposition. The fast autocatalytic kinetics of the accumulation and dissolution of $Co(OH)_2$ and potential dependent adsorption and desorption of Co-MPS complex are used to explain this oscillation phenomenon. This proposed mechanism is confirmed with a systematic study on the effects of various parameters including bulk pH, Co^{2+} and MPS concentration, rotation rate, as well as pH buffer. Moreover, oscillation is also observed when mercaptopropionic acid, is used, confirming the formation of Co-MPS complex through the thiol group, rather than the sulfonate group.

In Chapter 5, the effects of additives in electrolyte on the properties of electrodeposited Co films, such as morphology, sheet resistance, grain structure, the incorporation and distribution of impurity elements are investigated. SIMS analysis shows that the presence of DMG in electrolyte predominantly introduces N and C impurity into films. However, the further addition of MPS significantly increases S and decreases N incorporation. This phenomenon is believed to suggest a competitive adsorption between the DMG and MPS on electrode surface. XRD confirms that the addition of MPS results in smaller grains in the electrodeposited Co films. While such a refined grain structure contributes to a higher sheet resistance of as deposited Co films, it also eases the grain growth upon annealing resulting in the most significant resistance drop among all the different

additive cases studied. With atom probe tomography, randomly distributed S-rich and CoO clusters in nanometer scale are observed after the annealing of Co films deposited with all additives. More importantly, significant S and C segregation and marginal O segregation at grain boundaries are proved to occur during the annealing, probably correlating to the grain growth.

This dissertation provides some benchmark studies on Co electrodeposition with a class of suppressing additive. The electrochemical effects of additive, which is expected to facilitate Co superfilling, has been included, as well as the material properties of deposited Co that relates to the interconnect performance. Some perspectives are however provided here on the future research along this topic.

Co trench filling test

DMG has been selected to conduct preliminary studies and to demonstrate defect- free Co filling in trenches with a width of 140 nm and an aspect ratio of about 1:3. More research can be performed to investigate the detailed filling mechanism.

Numerical simulation of Co trench filling process

Because the size of trench is at nanometer scale and the trench filling process can be completed within a short time, it is very difficult, if not impossible, to experimentally measure the local concentrations of additives, pH gradient, and the convection process across the trench during the filling process. Numerical simulation provides a nice complementary approach to study the trench filling process.

Alternative metals for further scaling

Co is promising to be used to enable the scaling of interconnect due to its shorter electron mean free path than Cu. However, it is not the only metal with such properties, nor the best, but it is a convenient choice because of its compatibility with manufacturing process. Further scaling to even smaller dimension is expected to require metals with even shorter

mean free path, such as ruthenium (Ru),[1] of which a higher melting point suggests even better resistance to electromigration. However, electrodeposition of Ru is challenging because of its tendency to form oxides and no study has been reported on additives for Ru superfilling.

Machine learning for screening additives

Additives play an important role in the metal electrodeposition and interconnect fabrication. The development of appropriate chemicals to suppress or accelerate the metal deposition is time consuming and challenging. Machine learning is an emerging technique that has been applied to significantly expedite many research fields such as medical,[2] geology,[3] and electrochemical sciences.[4] It has been successfully demonstrated for new drugs selection on the basis of chemical information.[5] Therefore, future research can be conducted to develop the machine learning algorithm for additive screening process.

References

1. Gall, D., Electron mean free path in elemental metals. *J. Appl. Phys.* **2016,** *119* (8), 085101.

2. Kononenko, I., Machine learning for medical diagnosis: history, state of the art and perspective. *Artificial Intelligence in medicine* **2001,** *23* (1), 89-109.

3. Merembayev, T.; Yunussov, R.; Yedilkhan, A. In *Machine learning algorithms for classification geology data from well logging*, 2018 14th International Conference on Electronics Computer and Computation (ICECCO), IEEE: 2018; pp 206-212.

4. Mistry, A.; Franco, A. A.; Cooper, S. J.; Roberts, S. A.; Viswanathan, V., How Machine Learning Will Revolutionize Electrochemical Sciences. *ACS energy letters* **2021,** *6* (4), 1422-1431.

5. Yang, Q.; Bassyouni, A.; Butler, C. R.; Hou, X.; Jenkinson, S.; Price, D. A., Ligand biological activity predicted by cleaning positive and negative chemical correlations. *Proceedings of the National Academy of Sciences* **2019,** *116* (9), 3373-3378